Progress in Materials Science 135 (2023) 101090

Contents lists available at ScienceDirect

Progress in Materials Science

journal homepage: www.elsevier.com/locate/pmatsci

A review on the dynamic-mechanical behaviors of high-entropy alloys

Yu Tang [a,1], Ruixin Wang [a,1], Bin Xiao [c], Zhouran Zhang [a], Shun Li [a], Junwei Qiao [b,*], Shuxin Bai [a,*], Yong Zhang [d,*], Peter K. Liaw [e,*]

[a] College of Aerospace Science and Engineering, National University of Defense Technology, Changsha 410073, China
[b] College of Materials Science and Engineering, Taiyuan University of Technology, Taiyuan 030024, China
[c] Shenzhen Institute of Advanced Electronic Materials, Shenzhen 518055, China
[d] State Key Laboratory for Advanced Metals and Materials, University of Science and Technology Beijing, Beijing 100083, China
[e] Department of Materials Science and Engineering, The University of Tennessee, Knoxville, TN 37996, USA

ARTICLE INFO

Keywords:
Dynamic-mechanical behaviors
High-entropy alloys
Dynamic models
Dynamic-mechanical properties

ABSTRACT

High-entropy alloys (HEAs) are a family of novel multi-principal alloys containing >4 principal elements in equimolar ratios or nearly-equimolar ratios. The unique multiple-principal components bring in the high configurational entropy or mixing entropy, and some unique microstructures of HEAs. Consequently, many impressive properties of HEAs, including outstanding dynamical mechanical performance, have been reported successively. Under the instantaneous loading with high strain rates ($\dot{\varepsilon} > 10^3\ s^{-1}$), dynamic-deformation mechanisms of materials are different from the static one, and the relevant influencing factors are complicated. To reveal the relationship between the unique microstructures of HEAs and their dynamic-mechanical properties, 76 articles published during the period of July 2015 to January 2023 have been reviewed in the present work. Firstly, the statistics and classification of all 61 reported HEAs are systematically done in terms of their processing, experimental method, theoretical model, phases and microstructures as well as the dynamic-mechanical properties. Secondly, theoretical models and deformation mechanism are summarized. The effects of dislocation motion, twinning, and phase transformation behavior on dynamic deformation of HEAs are discussed thoroughly. The adiabatic-shear behavior and its effect on dynamic deformation are also considered. The differences of dynamic-mechanical behavior as well as the relevant mechanisms between HEAs and traditional metallic materials are described. Finally, the potential application under dynamic loads of HEAs are demonstrated thoroughly. The present article additionally deals with the future research directions of dynamic-mechanical behaviors in order to develop novel high-performance HEAs.

1. Introduction

With the development of science and technology, structural materials, especially metallic materials, are becoming more popularly

* Corresponding authors.
E-mail addresses: qiaojunwei@gmail.com (J. Qiao), shuxinbai@hotmail.com (S. Bai), drzhangy@ustb.edu.cn (Y. Zhang), pliaw@utk.edu (P.K. Liaw).

[1] These authors contributed equally.

https://doi.org/10.1016/j.pmatsci.2023.101090
Received 11 April 2022; Received in revised form 1 February 2023; Accepted 7 February 2023
Available online 18 February 2023
0079-6425/

utilized in more complex and extreme environments, including high-temperature, irradiation, and high-speed dynamic loading. For example, ultra-high strength steels can be used as armor [1,2,3,4]. In contrast, tungsten heavy alloys [5,6,7,8] and depleted uranium alloys [9,10,11] can serve as kinetic energy penetrators with the capability of penetrating the shell of the target and destroying its structural protection. In order to retain intact configuration under extreme conditions, high strength and sufficient ductility under dynamic loadings are desired for structural materials. In general, metallic materials show significant strain-rate effects [12]. More specifically, the Peierls-Nabarro stress, and the yield strengths of the materials increase with increasing strain rates, accompanied by a drastic loss of ductility [13]. Hence, new metallic materials with outstanding dynamic-mechanical properties and distinctive strain-rate effect, such as the simultaneous increment of strength and ductility with increasing strain rates, need to be developed.

High-entropy alloys (HEAs) are a family of novel multi-principal alloys, the conception of which was first proposed by Cantor [14] and Yeh [15] in 2004. Unlike conventional alloys composed of one or two principal elements and multiple trace elements, HEAs contain $>$4 principal elements in equimolar ratios or nearly-equimolar ratios [16]. The high configurational entropy or mixing entropy, then the freedom in the atomic-level design and the enormous combination space of HEAs give rise to some intriguing microstructures, such as the intrinsic lattice distortion [17,18,19,20], short-range orderings [21,22,23,23,24], and heterostructures [25,26,27,28]. These intriguing microstructures then lead to some distinctive properties, including the combination of high strength and large ductility [25,21,28,29,30], great radiation resistance [31,32,33,34], high corrosion resistance [35,36,37,38], and high creep resistance [39,40,41]. More importantly, through the tailored and optimized alloy design, some of the aforementioned properties can be achieved in a single HEA entity. Under such circumstances, HEAs have been extensively studied as potential candidates for structural applications under dynamic loadings.

Mishra et al. [42] firstly reported the dynamic behavior of the $Al_{0.1}CrFeCoNi$ HEA in 2015, which resembled low stacking fault materials. The onset strain of twinning was dependent on the strain rate, and some secondary nano-twins emerged in the high-strain-rate deformed $Al_{0.1}CrFeCoNi$ HEA. Since then, there have emerged plenty of studies concerning the dynamic deformation mechanism of HEAs under high strain rates, with several interesting dynamic-mechanical properties being reported one after another. For example, the strength and ductility of the CrFeCoNi HEA are enhanced simultaneously upon the high strain-rate tension because of short-range orders/clusters, phonon drag of dislocations, and nano-twins [43]. Lu et al. [44] and Pataky et al. [45] reported that the deformation twins led to a simultaneous increment in the strength and ductility of the CrMnFeCoNi HEA (Cantor alloy) under dynamic loading.

Besides the combination of the high dynamic strength and ductility, HEAs also exhibit other interesting dynamic properties. Dai et al. [46] reported that the FeNiMoW HEA not only showed excellent strength (1.9 GPa) and ductility (28%) under dynamic compression, but also demonstrated outstanding self-sharpening capability due to its multiphasic structure as well as the balance between the dynamic recrystallization and the formation of shear bands, which might provide new opportunities to develop high-performance penetrator materials. Bai et al. [47] designed the $TiZrHfTa_{0.53}$ HEA with the desired strength and ductility, and excellent energy-release characteristics. Under dynamic loading, $TiZrHfTa_{0.53}$ HEA with structural reliability reacted with air to release a large quantity of energy, manifesting its potential as high-strength energetic structural materials.

There have already been many reviews covering the aspects of the mechanical behaviors of HEAs [48,49,50,51], including Li et al.'s review published in 2019 which focuses on the mechanical properties of the HEAs with face-centered-cubic structures [52] and George et al.'s comprehensive review on the mechanical properties and deformation behaviors of HEAs in 2019 [53] containing some aspects of dynamic-mechanical behaviors. However, given the growing amount of work, a review focusing mainly on the dynamic-mechanical behaviors and related aspects, such as the energetic characteristics and the self-sharpening effect, of HEAs is still lacking and imperatively required. Meyers' et al reported the review about strain-rate effects and dynamic behavior of HEAs in November 2022 [54]. They pay attention to the mechanical behavior and failure mechanism of HEAs. But the relationship between microstructures and mechanical response upon dynamic loading is not illustrated in detail. In this review, the studies on the microstructural issues associated with dynamic deformation phenomena (typically with strain rates of 10^3–10^6 s^{-1}) of HEAs up to January 2023 have been summarized and discussed.

This review begins with the classification and the statistics from the perspectives of dynamic-mechanical properties, number of reports, and already reported alloy systems, etc. Afterwards, it moves on to establish the relationship between the complicated structure of HEAs and their dynamic-mechanical behaviors. Importantly, the effects of different structural characteristics of HEAs, including dislocation, lattice-distortion, twins etc. on the dynamic-mechanical behaviors, are analyzed and summarized. Finally, typical potential applications for the HEAs with improved dynamic-mechanical properties and special dynamic behaviors are proposed.

2. Taxonomy and statistical analysis

2.1. Classification of reported alloys

The first two papers regarding the dynamic-mechanical behaviors of $Al_{0.1}CrFeCoNi$ [42] and $AlTi_xCrFeCoNi$ [55] HEAs were reported in 2015. The literature on the topic of the dynamic-mechanical behaviors of HEAs remained relatively limited until 2017. Since then, the number of publications has increased continuously as shown in Fig. 1(a). To January 2023, a total number of 61 HEAs have been described in 76 articles. The HEA systems, whose dynamic behaviors are most frequently studied, are the $Al_xCrFeCoNi$ (present in 25 papers) [42,43,45,55,56,57,58,59,60,61,62,63,64,65,66,67,68,69,70,71,72,73,74,75,76] and CrMnFeCoNi (15 papers) [44,45,69,77,78,79,80,81,82,83,84,85,86,87,88] HEAs. At the meantime, there are also 2 HEAs ($Cr_{10}Mn_{30}Fe_{50}Co_{10}$ [89,90,91] and $AlCrFeCoNi_{2.1}$ [92,93,94]) reported in 3 papers, and 2 others (TiZrNbHfTa [95,96] and FeNiMoW [46,97]) reported in 2 papers, as shown in Fig. 1(b).

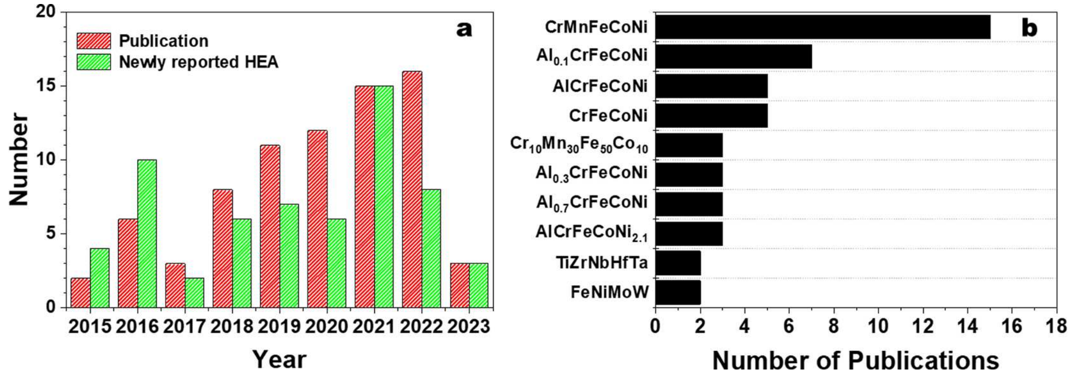

Fig. 1. (a) Cumulative number of publications and newly-reported HEAs as a function of publication year, up to January 2023. (b) Compositions of the most frequently studied HEAs and the number of publications where these compositions were studied.

2.2. Experimental methods for the dynamic-mechanical properties of reported HEAs

The common equipment for dynamic deformation at different velocities or strain rates are the split Hopkinson pressure bar (SHPB) ($\sim10^1$ m/s or 10^2–10^4 s^{-1}), light gas gun ($\sim10^2$ m/s or 10^5–10^6 s^{-1}), and ballistic gun ($\sim10^2$–10^3 m/s or $>10^6$ s^{-1}). Among them, SHPB (chosen in 59 papers [42,43,44,45,46,47,55,56,57,58,59,60,61,62,63,64,65,66,71,72,73,74,77,78,79,80,81,82,83,84,85,88,92,93,95,96,98,99,100,101,102,103,104,105,106,107,108,109,110,111,112,113,114,115,116,117,118,119,120]) is the most popular one, as shown in Fig. 2(a). By contrast, light gas gun was chosen in 7 papers [69,75,76,89,90,94,121] and the ballistic gun was chosen in 9 papers [46,47,67,74,92,97,111,115,122]. A Charpy pendulum impact tester can apply dynamic loading, which was selected in 2 papers [70,103]. Dynamic compression properties [42,44,46,47,55,56,57,58,59,60,61,62,63,64,65,66,72,73,74,77,78,80,81,82,83,85,88,92,93,95,96,98,99,100,101,102,103,105,106,107,108,109,110,111,112,113,115,116,117,118,119,120] have been reported in 52 papers while dynamic tensile [43,44,45,71,79,84,104,114] and shear [56,66,68,85,86,91,88,73] properties have been both reported in just 8 papers, (Fig. 2(b)). The numbers of papers concerning spallation induced by a light gas gun [69,75,76,89,90,94,121] and impact toughness [70,103] are 5 and 2, respectively. For ballistic gun tests, the energy release during penetration (3 papers [47,111,115]), penetration properties as projectile (3 papers [46,74,97]) and ballistic deformation as armor (3 papers [67,92,122]) were reported in 9 papers totally.

2.3. Theoretical models for the dynamic-mechanical behaviors of HEAs

2.3.1. Johnson-Cook (J-C) model

The J-C model is a phenomenological constitutive model most commonly employed to depict plastic flows under dynamic condition quantitatively.

(a) Classical J-C model

The mathematical expression of the J-C model under uniaxial-stress conditions at room temperature is written below [123]:

$$\sigma = \left(A + B\varepsilon_p^n\right)\left(1 + Cln\frac{\dot{\varepsilon}}{\dot{\varepsilon}_0}\right)\left[1 - \left(\frac{T - T_r}{T_m - T_r}\right)^m\right] \quad (1)$$

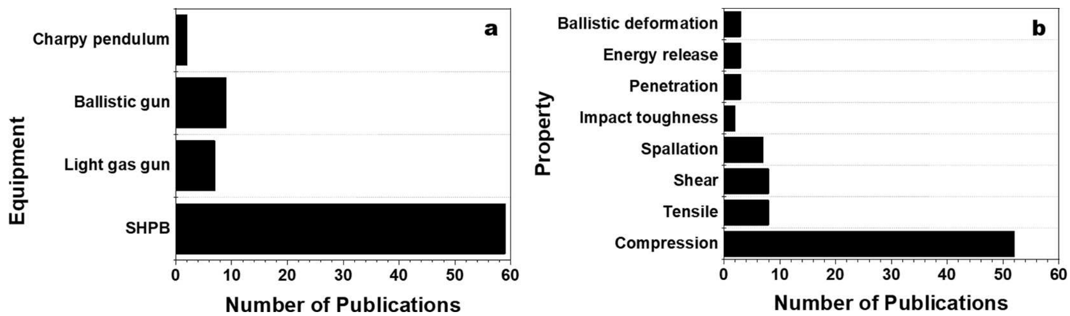

Fig. 2. (a) Number of publications for a given equipment to apply dynamic loads. SHPB represents the split Hopkinson pressure bar. (b) Number of publications for given properties under dynamic loads.

where σ is the uniaxial dynamic flow stress, ε_p is the uniaxial plastic strain, $\dot{\varepsilon}$ is the strain rate, $\dot{\varepsilon}_0$ is the reference strain rate and equals 10^3 s^{-1}, *A*, *B*, and *C* are parameters, *n* is the strain hardening exponent, *m* is the model constant, T_m is the melting temperature, and T_r is a reference temperature and equals 298 K. As shown in Eq. (1), the rheological stress of materials under a dynamic loading is jointly contributed by the effects of strain hardening, strain-rate hardening, and thermal softening.

The function of *C* can be expressed as a binary quadratic polynomial of variable strains and strain rates [124], usually simplified as the form of

$$C = C\left(\varepsilon_p, ln\frac{\dot{\varepsilon}}{\dot{\varepsilon}_0}\right) = C_0 + C_1\varepsilon_p + C_2 ln\frac{\dot{\varepsilon}}{\dot{\varepsilon}_0} + C_3\varepsilon_p ln\frac{\dot{\varepsilon}}{\dot{\varepsilon}_0} \tag{2}$$

where the strain- and strain-rate-dependent regression coefficients C_0-C_3 are required to be determined.

The work of plastic deformation can be used to calculate an adiabatic temperature rise as follows [12]:

$$\Delta T = T - T_0 = \int_{T_0}^{T} dT = \frac{\beta}{\rho C_p}\int_0^{\varepsilon_p}\sigma d\varepsilon \tag{3}$$

where ρ is the density, and C_p is the specific heat capacity, β is the efficiency of the strain energy converted into heat and is usually taken as 0.9 [125].

Combining Eqs. (1) and (3), and assuming $m = 1$, the J-C constitutive model equation can be modified as:

$$\sigma = (A + B\varepsilon^n)\left(1 + Cln\frac{\dot{\varepsilon}}{\dot{\varepsilon}_0}\right)exp\left(\frac{-0.9\left(1 + Cln\frac{\dot{\varepsilon}}{\dot{\varepsilon}_0}\right)}{\rho C_p(T_m - T_0)}\left(A\varepsilon + \frac{B\varepsilon^{n+1}}{n+1}\right)\right) \tag{4}$$

The curves based on the above modified J-C model agree well with the experimental observations in the systems of $Al_{0.3}CrFeCoNi$ [56], $Al_{0.6}CrFeCoNi$ [60], CrMnFeCoNi [78], $AlTi_{0.5}Cr_{1.5}Fe_{1.5}CoNi$ [100], $TiZrNbMo_xHfTa$ [107] HEAs.

However, some reports believed that the overlook of the effect of thermal softening also coincide well with the experimental results in the cases of $AlTi_xCrFeCoNi$ (x = 0, 0.2, and 0.4) [55], $(Al_{0.5}CrFeCoNi)_{0.95}Mo_{0.025}C_{0.025}$ [66], $Al_xCrMnFeCoNi$ (x = 0.4 and 0.6) [79] and $AlCrFeNi_2Cu$ [99] HEAs. It suggests that the strong work hardening but thermal effect dominates plastic flows in some HEAs, especially those without refractory elements.

(b) improved J-C model-1

For high strain-rate experiment at room temperature, the dynamic yield strength has a linear relationship with the logarithm of the strain rate, i.e., $\left(\frac{\sigma}{A} - 1\right)\propto \ln\frac{\dot{\varepsilon}}{\dot{\varepsilon}_0}$. Thus, the first two terms of the modified J-C constitutive equation (Eq. (1)) can be re-written as

$$\frac{\sigma}{A + B\varepsilon^n} - 1 = Cln\frac{\dot{\varepsilon}}{\dot{\varepsilon}_0} \tag{5}$$

For each true plastic strain rate, $\frac{\dot{\varepsilon}}{\dot{\varepsilon}_0}$ is a constant. Substituting the values of the flow stress and corresponding true plastic strain at different stain rates into Eq. (5), a series of *C* values can be obtained. There is an approximate linear relationship between ε_p and *C*. To get accurate constitutive parameter, *C* can be improved to a linear function of true plastic strain expressed as

$$C = C_1 + C_2\varepsilon_p \tag{6}$$

where C_1 and C_2 can be identified from the intercept and the slope of the fitted line.

Hence, the modified J-C model can be rewritten as:

$$1 - \frac{\sigma}{(A + B\varepsilon^n)\left(1 + Cln\frac{\dot{\varepsilon}}{\dot{\varepsilon}_0}\right)} = \left(\frac{T - T_r}{T_m - T_r}\right)^m \tag{7}$$

The values of *m* can be obtained by taking a logarithm transformation of Eq. (7) as well as the dynamic data at different temperatures T_r. Thus, the parameter *m* can be expressed as the following polynomial equation:

$$m = a + b_1\dot{\varepsilon} + b_2\dot{\varepsilon}^2 \tag{8}$$

Finally, the improved J-C model can be obtained as follows:

$$\sigma = (A + B\varepsilon^n)\left(1 + (C_1 + C_2\varepsilon)ln\frac{\dot{\varepsilon}}{\dot{\varepsilon}_0}\right)\left(1 - \left(\frac{T - T_r}{T_m - T_r}\right)^{a + b_1\dot{\varepsilon} + b_2\dot{\varepsilon}^2}\right) \tag{9}$$

This improved J-C model was found to be applicable in describing the flow behavior of TiZrNbHfTa HEAs [96].

(c) Improved J-C model-2

The aforementioned improved J-C constitutive equation cannot describe the characteristics that the flow stress of the materials increases sharply with the increase of strain rates near the strain rate of (10^3–10^4) s^{-1}. In the $Al_{0.3}Ti_{0.3}CrFeCoNi$ HEA [112], the relationship between the dynamic yield strength and strain rate tends to be a power function rather than a linear one. Therefore, the power function form in the Cowper-Symonds model [126] can be used to replace the strain-rate strengthening term in the original J-C model as follows:

$$\sigma = (A + B\varepsilon^n)\left[1 + \left(\frac{\dot{\varepsilon}}{C}\right)^{\frac{1}{P}}\right])exp\left(\frac{-0.9\left(1 + \left(\frac{\dot{\varepsilon}}{C}\right)^{\frac{1}{P}}\right)}{\rho C_p(T_m - T_0)}\left(A\varepsilon + \frac{B\varepsilon^{n+1}}{n+1}\right)\right) \tag{10}$$

The improved J-C constitutive model can better describe the dynamic flow behaviors of the $Al_{0.3}Ti_{0.3}CrFeCoNi$ HEA at different strain rates [112].

2.3.2. Zerilli-Armstrong (Z-A) model

The Z-A model is a physical constitutive model [127] derived from dislocation mechanisms that play an essential role in the plastic deformation of metallic materials under various deformation conditions. There are two reasonably explicit expressions to describe the plastic flow stresses of face centered cubic (FCC) or body centered cubic (BCC) structured metallic materials for their constitutive behaviors.

(a) The Z-A model for FCC-HEAs

For FCC-alloys, the Z-A model used for the prediction of strain-rate flow behavior can be represented as follows:

$$\sigma = \left(C_1 + C_2\varepsilon_p^P\right)exp(T \times [C_3 ln\dot{\varepsilon} - C_4]) \tag{11}$$

where C_1, C_2, C_3, C_4, and P are material constants, respectively. Note that the value of T is 298.15 K.

A modified Z-A model for FCC alloys was also proposed to account for the coupling effect of the strain rate and temperature on the flow stress with the form of:

$$\sigma = \left(A_1 + A_2\varepsilon_p^n\right)exp\left\{ - (A_3 + A_4\varepsilon_p)\overline{T} + (A_5 + A_6\overline{T})ln\frac{\dot{\varepsilon}}{\dot{\varepsilon}_0}\right\} \tag{12}$$

where $\overline{T} = (T - T_r)$, A_1, A_2, A_3, A_4, A_5, and A_2 are material parameters.

The theoretical predictions based on the above Z-A model for stress–strain response are in good agreement with experimental measurements for FCC-HEAs, such as CoCrFeMnNi HEAs[77].

(b) The Z-A model for BCC-HEAs

For BCC-alloys, the Z-A model can be represented as follows:

$$\sigma = \Delta\sigma'_G + c_1 exp(- c_3T + c_4Tln\dot{\varepsilon}) + c_5\varepsilon_p^n + kd^{-\frac{1}{2}} \tag{13}$$

An alternative approach for determining the thermal stress as a function of both strain rate and temperature can be obtained by assuming that the activation volume is independent of strain rate and temperature. Thus, the modified Z-A model is written as [128]:

$$\sigma = \widehat{Y}exp(- \beta_3T + \beta_2Tln\dot{\varepsilon}) + B\varepsilon^n + Y_a \tag{14}$$

where $\widehat{Y}$ is the threshold yield stress and equals approximately to yield strength under quasi-static condition when $\varepsilon = 0$ [128], β_3, β_2, B and n are the constants and Y_a represents the temperature-independent stress, $B\varepsilon^n + Y_a$ is the athermal stress and taken as the grain boundary strengthening for various alloys [43].

The Z-A model discussed above is usually applied to analyze the experimental behavior of the $TiZrNbMo_xHfTa$ HEAs [107], matching quite well with the experimental results.

2.3.3. Khan and Liang (KHL) and Khan and Liu (KL) models

(a) KHL model

The Huang and Khan model [129], a modified version of the Bodner-Partom model, is widely accepted as an empirical model. Afterwards, Khan and Liang modified it into the KHL model [13], whose applicability in BCC metals has been already verified. The KHL model has the form as denoted in Eq. (15):

$$\sigma = \left(A + B\varepsilon_p^{n0}\left(1 - \frac{ln\dot{\varepsilon}}{lnD_0^P}\right)^{n1}\right)(exp(Cln\dot{\varepsilon}))\left(1 - \left(\frac{T - T_r}{T_m - T_r}\right)^m\right) \tag{15}$$

The KHL model considers the coupled effect of the strain and strain rate on the flow stress through the strain-rate exponent $n1$. The second bracketed term is incorporated to include the effect of viscous drag on the yield stress at high strain rates. The exponent m is related to the thermal softening of the materials at higher temperatures, and n_0 is the strain hardening exponent.

The KHL model was further modified so as to depict the behaviors of nanocrystalline iron, copper mixture and titanium etc. The modified KHL model is given in Eq. (16):

$$\sigma = \left(A + B\varepsilon_p^{n0}\left(1 - \frac{ln\dot{\varepsilon}}{lnD_0^P}\right)^{n1}\right)\left(\frac{\dot{\varepsilon}}{\dot{\varepsilon}_0}\right)^C\left(1 - \left(\frac{T - T_r}{T_m - T_r}\right)^m\right) \tag{16}$$

(b) Khan and Liu (KL) model

Khan and Liu proposed an empirical constitutive model based on the KHL model to account for strain-rate sensitivity and thermal softening in AA 2024-T35 [130,131]. The model is expressed in Eq. (17)

$$\sigma = \left[A + B\varepsilon_p^{n0}exp(-C_3\frac{\dot{\varepsilon}}{\dot{\varepsilon}_0})\left(\frac{T_m - T}{T_m - T_r}\right)^{m1}\right]\left[exp\left(C_1\frac{\dot{\varepsilon}}{\dot{\varepsilon}_0}\right) - C_2(T)exp(-K_1\dot{\varepsilon})\right]\left[\frac{T_m - T}{T_m - T_r}\right]^{m2} \tag{17}$$

where

$$C_2(T) = \left[\frac{1}{2}\frac{(T - T_c) + |T - T_c|}{(T_m - T_r)}\right]^{m3} \tag{18}$$

In this model, the constant $C3$ and the exponent $m1$ describe the decrement in work hardening with increasing strain rate and temperature, respectively.

Mishra et al. utilized the modified J-C, the modified Z-A, the modified KHL, and the KL models to predict the flow behavior of $Fe_{38.5}Mn_{20}Co_{20}Cr_{15}Si_5Cu_{1.5}$ HEA [108]. According to their results, the J-C model could predict the flow behavior well at low strain rates ($10^{-3} - 100\ s^{-1}$), but failed to delineate the flow behavior accurately at higher strain rates (10^3 –$2.5 \times 10^3\ s^{-1}$) (see Fig. 3a) due to

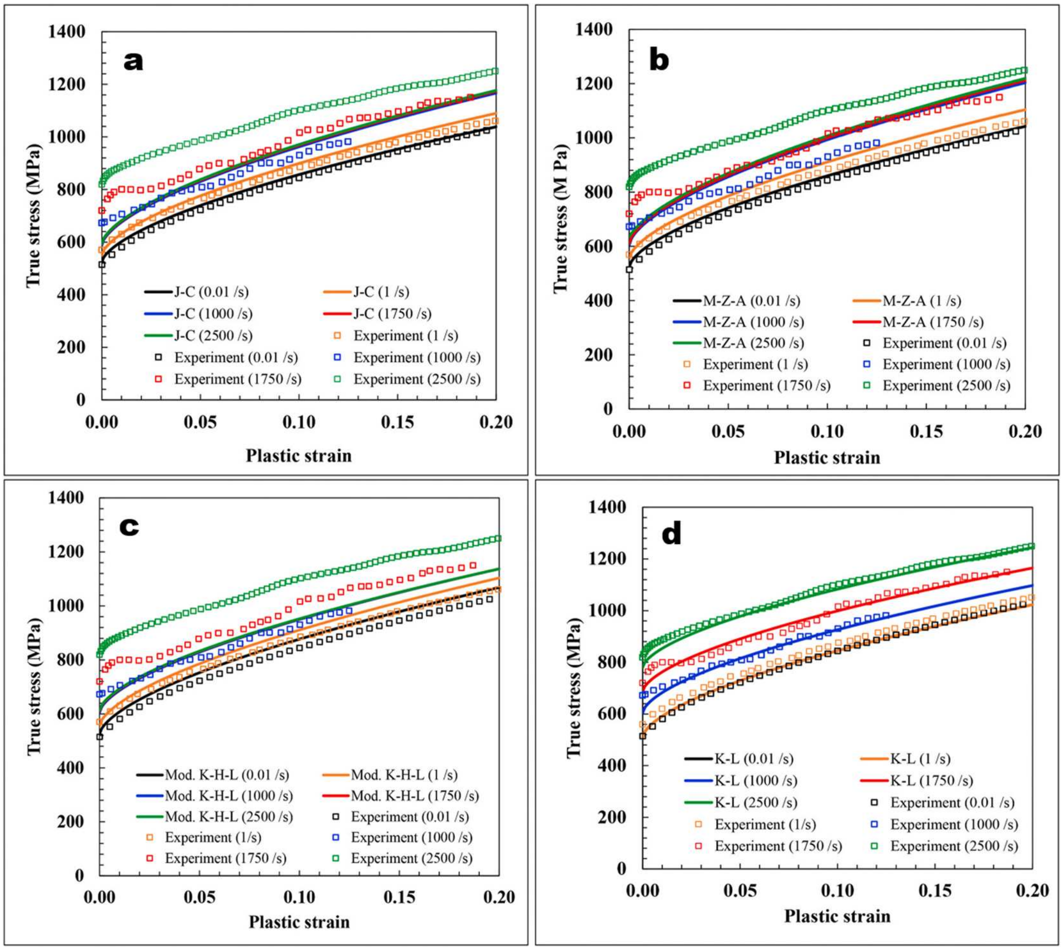

Fig. 3. Comparisons of different empirical models with the experimental results of $Fe_{38.5}Mn_{20}Co_{20}Cr_{15}Si_5Cu_{1.5}$ at multiple strain rates [108]. (a) the modified J-C model, (b) the modified ZA model, (c) the modified KHL model, and (d) the KL model.

the fact that the term $(1 + C\ln\frac{\dot{\varepsilon}}{\dot{\varepsilon}_0})$ in Eq. (1) is not sufficient to elucidate the viscous drag effect at strain rates higher than 10^3 s^{-1}. Similarly, the prediction of the modified Z-A model agreed with the experimental results in the strain-rate region of 10^{-3}–100 s^{-1} (Fig. 3b). However, it over-predicted strain hardening at high strain rates. By contrast, the modified KHL model over-predicted the flow behavior at low strain rate, whereas it under-predicted the flow response at high strain rate (Fig. 3c). Compared with the modified Z-A model, the modified KHL model exhibited a better trend in the stress–strain curve owing to the inclusion of the term $\left(1 - \frac{\ln\dot{\varepsilon}}{\ln D_0^p}\right)^{n1}$, which accounts for the reduction in hardening rate at high strain rate. The KL model could better correlate experimental results at high strain rates than the aforesaid three models (Fig. 3d). It successfully described the viscous drag effect as well as the reduction in strain hardening due to lower transformation levels at high strain rate. Moreover, its prediction reasonably agreed with experimental results at lower strain rates as well.

2.3.4. *Strengthening mechanism models*

(a) Microstructure-based constitutive model

In CrFeCoNi HEA, the flow stress (σ) can be decomposed into a simple summation of solid solution strengthening (σ_{ss}), grain boundary (Hall-Petch) strengthening (σ_g), and forest hardening (σ_f) shown as follows:

$$\sigma(\varepsilon,\dot{\varepsilon},T) = \sigma_{ss}(\dot{\varepsilon},T) + \sigma_g + \sigma_f(\varepsilon,\dot{\varepsilon},T) = \sigma_y(\dot{\varepsilon},T) + \sigma_f(\varepsilon,\dot{\varepsilon},T) \tag{19}$$

where σ_{ss} includes the lattice friction stress and the strengthening effect from short-range orders/clusters [132], σ_g takes the grain refinement from the annealing twins into account, and σ_f shows the dislocation–dislocation interactions that enhances with increasing dislocation density.

In this model, thermal activation strain-rate analysis related to short-range obstacles is employed. A form of Z-A model [127] was used to describe the effects of the temperature and strain rate on the yield strength σ_y of CrFeCoNi HEA, as shown in Fig. 4 [43]. However, an obvious deviation between the experimental results and the prediction of the thermal activation equation (blue thread) was found at strain rates higher than 10^3 s^{-1}. It is well established that the dislocation motion will be impeded by the interaction between the dislocation and lattice vibration (phonon viscosity) at high strain rates, thus enhancing the strength. In such a case, a thermal activation rate equation considering phonon drag effect (introduced via a simplified form) is utilized as follows [133].

$$\sigma_y = \sigma_0^* exp(-\beta_0 T + \beta_1 T ln\dot{\varepsilon}) \Big/ (1 - c\dot{\varepsilon})^{\beta_1 T} + \sigma_g \tag{20}$$

where β_0 and β_1 are material constants, σ_0^* is the thermal stress at $T = 0$ K, σ_g is the athermal stress and taken as the grain boundary strengthening. c is a material parameter. The thermal activation rate equation considering dislocation drag better depicted the strain-rate sensitivity of σ_y for CrFeCoNi HEA under dynamic loading.(b) Taylor-hardening model

The Taylor hardening model [134] was proposed to describe the work hardening behavior of the CrFeCoNi HEA.

$$\sigma_f = M\alpha Gb\sqrt{\rho} \tag{21}$$

where M is the Taylor factor, G is the shear modulus, α is the constant related to dislocation interaction strength, ρ is the total dislocation density, and b is the Burgers vector for perfect dislocation. The evolution of the total dislocation density considering the competition between the dislocation storage and recovery can be given by the following expression [135].

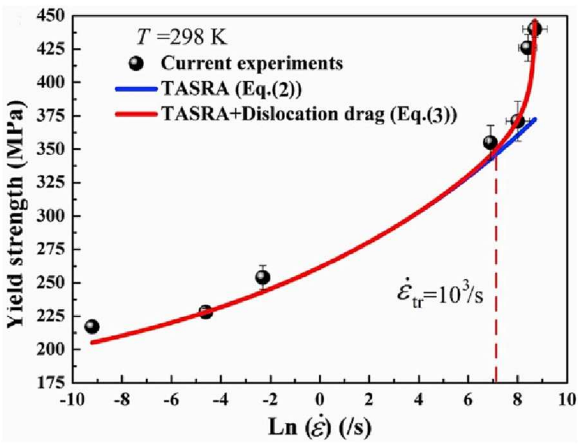

Fig. 4. Comparison of the experimental data and the modelling results of the dependence of yield stress on strain rate in CrFeCoNi HEA [43]. TASRA represents thermal activation strain-rate analysis.

$$\frac{d\rho}{d\varepsilon} = M\left(\frac{1}{b\Lambda} - k_{\tau}\rho\right) \tag{22}$$

where k_τ is the dislocation recovery factor, and Λ is the mean free path associated with the immobilization of mobile dislocations at obstacles after traveling a distance. For some HEAs, nanotwin boundaries are considered during the evolution of dislocations, i.e., $\frac{1}{\Lambda} = k_\rho\sqrt{\rho} + \frac{i\Delta}{\Delta}$. The value of k_ρ shows the effectiveness of the dislocation structure to dislocation storage, usually taken as $k_{\rho 1}$ and $k_{\rho 2}$ under quasi-static and dynamic conditions, respectively, owing to different dislocation structures. The value of Δ is the average twin spacing and $i\Delta$ is a constant for scaling the contribution of the average twin spacing to effective boundary distance [136]. The evolution of Δ is in connection with the average twin thickness (t) and twin volume fraction (F) based on the analysis of Fullman [137].

$$\Delta = 2t\frac{1-F}{F} \tag{23}$$

where t is assumed to be a constant. The twinning kinetics can be obtained from Olson and Cohen's analysis [138].

$$F = 1 - exp(-\phi(\varepsilon - \varepsilon_{int})) \tag{24}$$

where ϕ is a material constant, and ε_{int} is twinning initial strain determined by the critical twinning stress (σ_{int}).

The strain-hardening behavior is connected with the annihilation of stored dislocations, i.e., dislocation recovery, especially at large deformation. The dislocation recovery is a thermally activated process since it is in fact based on dislocation motion.

$$k_r = k_{r0}\left(\frac{\dot{\varepsilon}}{\dot{\varepsilon}_0}\right)^{-\frac{KT}{A}} \tag{25}$$

where k_{r0} is the recovery factor at 0 K, and K is Boltzmann constant. $\dot{\varepsilon}_0$ is the reference strain rate (taken as 10^7 s^{-1}) [139], and A is a material parameter dependent on the stacking fault energy (SFE).

Adiabatic heating generally occurs at high strain rate and considerably affects dislocation evolution via temperature-dependent dislocation recovery. For simplification, the evolution of the heat with plastic strain is described in a curvilinear form expressed as below:

$$\Delta T = a_T\varepsilon_p + b_T\varepsilon_p^n \tag{26}$$

where a_T, b_T, and n are fitting parameters, respectively.

The present constitutive model dovetails nicely with the evolution of flow stresses against strains in the NiCoCrFe HEA over a wide range of strain rates.

(c) Thermo-viscoplastic constitutive model

A thermo-viscoplastic constitutive model that independently considers twin enhancement effect is summarized as follows for the CrMnFeCoNi HEA:

$$\sigma(\varepsilon, \dot{\varepsilon}, T) = \sigma_{matrix} + \sigma_{twin} \tag{27}$$

where σ_{matrix} is the matrix-related stress, and σ_{twin} is the twin-related stress. The stresses of the matrix and the twins weighted by their respective contents are given as

$$\sigma(\varepsilon, \dot{\varepsilon}, T) = (1-F)\sigma^m(\varepsilon, \dot{\varepsilon}, T) + F\sigma^t(\varepsilon, \dot{\varepsilon}, T) \tag{28}$$

where F is the twin volume fraction, σ_m and σ_t are the flow stresses of the matrix and the twin, respectively. The flow stress of the matrix is decomposed into a solution strengthening stress, $\sigma^m_{ss}(\dot{\varepsilon}, T)$, a grain boundary strengthening stress σ^m_{HP}, and a dislocation forest strengthening stress $\sigma^m_{for}(\varepsilon, \dot{\varepsilon}, T)$. Similarly, the flow stress of the twin is decomposed into a twin critical stress σ^t_{crit}, a twin boundary strengthening stress σ^t_{HP}, and the effect of the twin on the surrounding dislocation slip $\sigma^t_{slip}(\varepsilon, \dot{\varepsilon}, T)$ [43,140,141]. The formula can be further written as

$$\sigma(\varepsilon, \dot{\varepsilon}, T) = (1-F)\left(\sigma^m_{ss}(\dot{\varepsilon}, T) + \sigma^m_{HP} + \sigma^m_{for}(\varepsilon, \dot{\varepsilon}, T)\right) + F\left(\sigma^t_{crit} + \sigma^t_{HP} + \sigma^t_{slip}(\varepsilon, \dot{\varepsilon}, T)\right) \tag{29}$$

The solution strengthening stress of the matrix, $\sigma^m_{ss}(\dot{\varepsilon}, T)$, is determined by the yield strength obtained from experiments. The effect of the Hall-Petch term is introduced to describe the grain boundary strengthening stress of the matrix and the twins, given respectively as

$$\sigma^m_{HP} = \frac{HP}{\sqrt{d_g}} \tag{30}$$

$$\sigma^t_{HP} = \frac{HP_t}{\sqrt{d_{twin}}} \tag{31}$$

where HP is the Hall-Petch coefficient, d_g is the grain size, and HP_t is the Hall-Petch coefficient of the twins. The parameter d_{twin} is the equivalent grain size of a grain containing twins, given as

$$d_{twin} = \frac{1-F}{sin(\alpha)n}d_g \tag{32}$$

where α is the angle between the slip plane and the twin plane, and n is determined by the average number of lamellae inside the matrix grains [141]. The Taylor hardening model describes the dislocation forest strengthening of the matrix as shown below:

$$\sigma^m_{for}(\varepsilon,\dot{\varepsilon},T) = M\chi Gb\sqrt{\rho(\varepsilon,\dot{\varepsilon},T)} \tag{33}$$

where M is the Taylor constant, χ is the dislocation hardening coefficient, G is the shear modulus, and $\rho(\varepsilon,\dot{\varepsilon},T)$ is the dislocation density. The evolution of the dislocation density is described by the Kocks-Mecking-Estrin evolution law model [142], given as

$$\frac{d\rho}{d\varepsilon} = M\left(\frac{1}{bL} - f(\dot{\varepsilon},T)\rho\right) \tag{34}$$

where $f(\dot{\varepsilon},T)$ is the strain-rate and temperature-dependent dynamic recovery coefficient of dislocation, and L is the mean free path determined by

$$\frac{1}{L} = \frac{1}{d_g} + k\sqrt{\rho} \tag{35}$$

where k is the work hardening coefficient. Additionally, $\sigma^t_{slip}(\varepsilon,\ \dot{\varepsilon},T)$ increases in proportion to the slip dislocation density such that

$$\sigma^t_{slip}(\varepsilon,\dot{\varepsilon},T) = MGCbb_t(\varepsilon,\dot{\varepsilon},T) \tag{36}$$

where C is the twin hardening coefficient, and b_t is the Burgers vector of the twinning dislocation. The evolution of the twin volume fraction F is described as

$$\begin{cases} F = 0\sigma < \sigma^t_{crit} \\ \frac{dF}{d\varepsilon} = (1-F)NV_{tw}\sigma \geq \sigma^t_{crit} \end{cases} \tag{37}$$

where N is the number of nuclei per unit volume, and the V_{tw} is the volume of a newly-formed twin [136]. In this model, the probability of twin nucleation is related to the instantaneous flow stress, given as

$$N = N_0 exp\left[-\left(\frac{\sigma^t_{crit}}{\sigma}\right)^{s(\dot{\varepsilon},T)}\right] \tag{38}$$

where N_0 is a material constant, and $s(\dot{\varepsilon},T)$ is the twin growth efficiency dependent on strain rate and temperature. Among them, the twin critical stress, σ^t_{crit}, can be calculated according to the following formula [143].

$$\sigma^t_{crit} = \frac{2\gamma_{SF}}{mb_p} \tag{39}$$

where γ_{SF} is the SFE, m is the Schmid factor, and b_p is the Burgers vector of the partial dislocation. Following twin nucleation, it is assumed that the twin nuclei immediately grow into disc-shaped twins, whose diameter and thickness are approximately equal to that of the grain size and the average twin width, respectively:

$$V_{tw} = \frac{1}{4}\pi e d_g^2 \tag{40}$$

where e is the average twin width.

This constitutive model is in excellent agreement with the tensile test data of the CrMnFeCoNi HEA [84].

2.3.5. *Adiabatic shear during dynamic deformation*

(a) Adiabatic-temperature rise for whole sample

As already discussed in Section 2.3.1, the adiabatic temperature rise can be calculated through the work of deformation (see Eq. (3)). For the CrMnFeCoNi HEA, the maximum possible temperature rise was estimated to be 96 K when the sample was tested at 2,300 s^{-1} [44], which is comparable to that reported in some TWIP steels [144]. The temperature rise ΔT achieved 120 K at the strain rate of 4,600 s^{-1} for dual-BCC structured $AlTi_{0.5}Cr_{1.5}Fe_{1.5}CoNi$ HEA [100], while it reaches 149 K at the strain rate of 4,000 s^{-1} for the $Al_{0.6}CrFeCoNi$ HEA with FCC plus BCC structure [60]. The final temperature rise of the $Al_{0.3}Ti_{0.3}CrFeCoNi$ HEA at a strain rate of 4,700 s^{-1} is 178 K [112]. Mishra et al. [108] studied the relationship between the strain and ΔT at different strain rates in the $Fe_{38.5}Mn_{20}Co_{20}Cr_{15}Si_5Cu_{1.5}$ HEA via Eq. (3), where the value of β was taken as 0.6. As displayed in Fig. 5, the temperature rise under

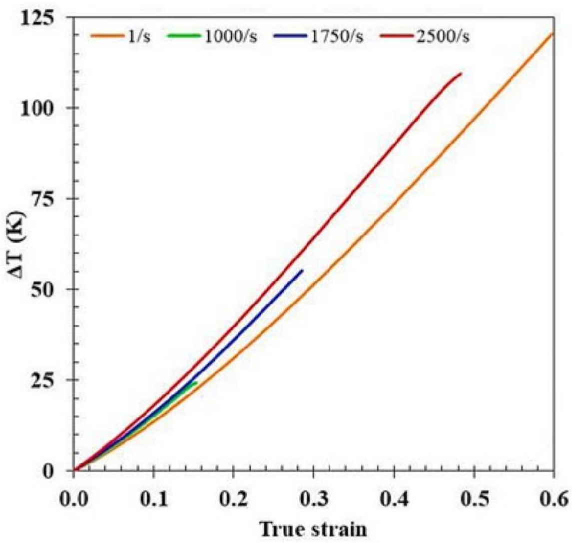

Fig. 5. Temperature rise as a function of strain in the $Fe_{38.5}Mn_{20}Co_{20}Cr_{15}Si_5Cu_{1.5}$ HEA due to adiabatic heating [108].

dynamic condition is appreciable, reaching 110 K at 50% true strain during high strain-rate deformation (2,500 s^{-1}).

Meyers et al. utilized a modified J-C constitutive equation to calculate the relationship between the temperature and plastic strain at a fixed strain rate [145].

$$\sigma = \left(\sigma_y + B\varepsilon_p^n\right)\left(1 + Clog\frac{\dot{\varepsilon}}{\dot{\varepsilon}_0}\right)\left(\frac{T}{T_r}\right)^{\lambda} \tag{41}$$

where λ is an experimentally determined parameter. By substituting Eq. (3) into Eq. (41), the mathematical expression of the temperature is obtained as:

$$T = \left[T_r^{-\lambda+1} + \frac{1 + Clog\frac{\dot{\varepsilon}}{\dot{\varepsilon}_0}}{\rho C_p T_r^{\lambda}} \times 0.9(1-\lambda)\varepsilon\left(\sigma_0 + \frac{B\varepsilon^n}{n+1}\right)\right]^{\frac{1}{1-\lambda}} \tag{42}$$

The temperature at an extremely high strain rate of 10^4 s^{-1} and a true strain of 0.5 was only 402 K, indicating a temperature rise of 109 K in $Al_{0.3}$CrFeCoNi HEA [56].

(b) Adiabatic-temperature rise in an adiabatic-shear band (ASB)

The temperature rise in ASB can be evaluated based on the principle that plastic work converts into heat at quasi-adiabatic conditions. The temperature rising is given by [125].

$$\Delta T = \frac{\beta W_p}{\rho C_p} \tag{43}$$

where W_p is the specific plastic work. Accordingly, we have:

$$\Delta T = \frac{\beta}{\rho C_p}\int_0^{\gamma_f} \tau d\gamma \tag{44}$$

where γ_f is the final shear strain that can be estimated from SEM images.

For the W-$Al_{0.5}V_{0.2}Cr_{0.9}FeNi_{2.5}$ HEA, the shear strain in ASBs was estimated to be at least 400% based on the microstructure. The temperature in ASBs was calculated to be above 1,870 K [113].

(c) Formation of ASBs

An adiabatic shear band can form when the material starts to "soften". The condition for instability is $\frac{d\tau}{d\gamma} \le 0$, and can be obtained from the general function, $\tau = f(\gamma, \dot{\gamma}, T)$,

$$\frac{d\tau}{d\gamma} = \left(\frac{\partial\tau}{\partial\gamma}\right)_{\dot{\gamma},T} + \left(\frac{\partial\tau}{\partial\gamma}\right)_{\gamma,T}\frac{\partial\dot{\gamma}}{\partial\gamma} + \left(\frac{\partial\tau}{\partial T}\right)_{\gamma,\dot{\gamma}}\frac{dT}{d\gamma} \le 0 \tag{45}$$

The normal stress and strain at a constant strain rate can be converted to corresponding shear stress and shear strain [146] via $\tau = \frac{\sigma}{2}$ and $\gamma = \sqrt{2e^{2\varepsilon} - 1} - 1$.

In the $Al_{0.3}CrFeCoNi$ HEA [56], at the constant $\dot{\gamma}$ and T, $\frac{\partial\dot{\gamma}}{\partial\gamma} = 0$, the strain hardening parameter and the thermal softening parameter were ~ 440 MPa and ~ − 0.2 MPa/K, respectively. Consequently, $\frac{dT}{d\gamma} = 175\ K^{-1}$. Neglecting the second term in Eq. (45), Eq. (46) can be obtained:

$$\frac{d\tau}{d\gamma} = \left(\frac{\partial\tau}{\partial\gamma}\right) + \left(\frac{\partial\tau}{\partial T}\right)\frac{dT}{d\gamma} \approx 440 - 0.2 \times 175 = 405MPa \geq 0 \quad (46)$$

Grady et al. proposed adiabatic shear dissipation energy (ASDE) Γ as a criterion to measure the adiabatic-shear sensitivity [147].

$$\Gamma = \frac{\rho C_p}{a}\left(\frac{9\rho^3 c^2 \chi^3}{\sigma_y^3 \alpha^2 \dot{\varepsilon}}\right)^{\frac{1}{4}} \quad (47)$$

$$\chi = \frac{\lambda}{\rho C_p} \quad (48)$$

where χ is the thermal diffusivity coefficient, α is the thermal softening coefficient and λ is the thermal conductivity. The parameters ρ, C_p, λ, and α are associated with the intrinsic properties of the materials.

In summary, many theoretical models have been proposed in order to describe the dynamic-mechanical behaviors of HEAs. A classic J-C model is generally used to fit the dynamic stress–strain curves of FCC HEAs. By contrast, the modified and improved J-C models are suitable for BCC HEAs, especial refractory high-entropy alloys (RHEAs), due to unignorable thermal effect. The Z-A model can successfully describe dislocation motion in HEAs including both FCC and BCC HEAs. As empirical models, the KHL and KL models agree better with the experimental observations of the mechanical properties of BCC-HEAs at high strain rates (>2,000 s^{-1}). Meanwhile, some classic strengthening models, such as solid solution strengthening, grain boundary (Hall-Petch) strengthening and Taylor strengthening models can be used to explain the dynamic strengthening mechanisms of HEAs. In addition, some models relevant to plastic deformation energy and temperature are also applicable to interpreting adiabatic behavior in BCC- RHEAs.

2.4. Dynamic-mechanical properties of reported HEAs

The dynamic-mechanical properties of reported HEAs are listed in Table 1.

Table 1
Mechanical properties of HEAs under dynamic loads. The following acronyms are used: AC (as-cast); CW (cold-worked); HW (hot-worked); HIP (hot-isostatic pressed); PM (powder metallurgy); A (annealed); LGG (light gas gun); Charpy pendulum impact tester (CP); BG (ballistic gun); C (compression); T (tensile); S (shear); PT (phase transformation); TW (twinning); AS (adiabatic shear); F (fracture); $\dot{\varepsilon}$ (strain rate); σ_y (yield strength); σ_u (ultimate strength); ε_u(ultimate strain); – (unavailable).

Alloy	Year	Processing	Phase	Equipment, load mode	$\dot{\varepsilon}$(s^{-1})	σ_y (MPa)	σ_u (MPa)	ε_u (%)	Additional mechanism
$Al_{0.3}Ti_{0.3}CrFeCoNi$	2021 [112]	AC	$FCC/L1_2$ + BCC/B2	SHPB, C	1,500	1,002	1,300	12	–
					2,900	1,066	1,660	25	–
					3,600	1,130	1,750	32	–
					4,700	1,181	1,800	44.6 (F)	AS
$AlTi_{0.2}CrFeCoNi$	2015 [55]	AC	BCC	SHPB, C	1,790	1,772	2,748	12	–
					2,060	1,793	2,820	13.4	–
					2,310	1,836	2,825	15.5	–
					2,770	1,893	2,895	13.3 (F)	–
$AlTi_{0.4}CrFeCoNi$	2015 [55]	AC	BCC	SHPB, C	1,550	2,032	2,350	9.1	–
					2,000	2,050	2,800	8.8	–
					2,350	2,065	2,625	11.7 (F)	–
					2,900	2,090	2,900	12.7 (F)	–
$AlTi_{0.5}Cr_{1.5}Fe_{1.5}CoNi$	2017 [100]	AC	BCC + BCC	SHPB, C	2,800	2,010	2,265	13 (F)	–
					3,500	2,200	2,270	15.5 (F)	–
					4,600	2,250	2,480	17(F)	–
$Al_{0.2}CrFeCoNiCu_{0.8}Si_{0.2}$	2016 [98]	AC	FCC + $L1_2$	SHPB, C	3,500	640	1,500	26.5	–

(continued on next page)

Table 1 (*continued*)

Alloy	Year	Processing	Phase	Equipment, load mode	$\dot{\varepsilon}$(s^{-1})	σ_y (MPa)	σ_u (MPa)	ε_u (%)	Additional mechanism
$Al_{0.5}CrFeCoNiCu_{0.5}Si_{0.2}$	2016 [98]	AC	FCC + BCC + B2	SHPB, C	3,500	870	1,740	29	–
$Al_{0.9}CrFeCoNiCu_{0.1}Si_{0.2}$	2016 [98]	AC	BCC + B2	SHPB, C	3,500	2,010	2,850	19	–
$Al_{0.1}CrFeCoNi$	2015 [42]	–	FCC	SHPB, C	1,000	220	820	40	–
					2,600	243	830	42	TW
	2016 [70]	HW	FCC	CP	Charpy impact energy: 420 J				–
	2018 [59]	AC	FCC	SHPB, C	10^3	300	405	12	–
		CW	FCC	SHPB, C	10^3	775	900	12.5	TW
		CW + A	FCC	SHPB, C	10^3	795	805	8	TW
	2020 [63]	HIP	FCC	SHPB, C	2,500	380	880	30	–
					2,500	417	1,030	40	–
					4,000	467	1,090	51	TW
					3,000 (77 K)	524	1,290	38	–
					4,000 (77 K)	574	1,395	44.5	–
					4,700 (77 K)	619	1,510	51	TW
	2020 [67]	AC	FCC	BG	594 m/s	Partial penetration			TW
					739 m/s	Plug			TW, AS
					994 m/s	Full penetration			TW, AS
	2022 [71]	A	FCC	SHPB, T	4,500	240	710	56 (F)	–
					7,000	252	885	56 (F)	–
					4,500 (77 K)	400	1,100	58(F)	TW
	2022 [75]	AC	FCC	LGG	307 m/s	Spall strength: 3.635 GPa			–
					511 m/s	Spall strength: 3.735 GPa			–
					762 m/s	Spall strength: 4.040 GPa			TW
$Al_{0.3}CrFeCoNi$	2016 [70]	HW	FCC	CP	Charpy impact energy: 413 J				–
	2017 [56]	HIP + A	FCC	SHPB,C	1,800	5,03	795	25	AS
				SHPB, S	–	–	–	110	AS
	2018 [58]	CW + A	FCC + $L1_2$	SHPB, C	2,000	480	860	17.5	TW
$Al_{0.5}CrFeCoNi$	2021 [64]	HW + A	FCC + BCC + B2	SHPB, C	2,000	1,352	1,503	15.5 (F)	–
$(Al_{0.5}CrFeCoNi)_{0.95}Mo_{0.025}C_{0.025}$	2019 [66]	PM	FCC + BCC + $M_{23}C_6$	SHPB, C	550	754	1,375	7	–
					1,300	878	2,200	16	–
					2,200	958	1,995	12.5	–
					3,000	1,057	2,400	18	–
				SHPB, S	–	–	–	2.53 (F)	–
					–	–	–	5.3 (F)	AS
					–	–	–	9.83 (F)	AS
$Al_{0.6}CrFeCoNi$	2018 [60]	AC	FCC + BCC	SHPB, C	2,800	880	1,400	32.5	–
					3,600	942	1,480	36	–
					4,000	997	1,530	40 (F)	TW
$Al_{0.7}CrFeCoNi$	2018 [57]	CW	FCC + B2	SHPB, C	2,000	1,820	1,815	19	–
		CW + A	FCC + B2 + $L1_2$	SHPB, C	2,000	2,200	2,180	20	–
	2019 [61]	CW + A	FCC + BCC + $L1_2$ & B2	SHPB, C	2,000	1,440	1,800	20	TW
	2020 [68]	HW + A	FCC + $L1_2$/BCC + B2	SHPB, S	7 m/s	1,200	1,490	24	–
					11.26 m/s	1,320	1,385	70 (F)	AS
					17.1 m/s	1,500	580	130	AS

(*continued on next page*)

Table 1 (*continued*)

Alloy	Year	Processing	Phase	Equipment, load mode	$\dot{\varepsilon}(s^{-1})$	σ_y (MPa)	σ_u (MPa)	ε_u (%)	Additional mechanism
AlCrFeCoNi	2015 [55]	AC	BCC	SHPB, C	960	1,546	2,005	5.8	–
					2,000	1,571	2,510	12.7	–
	2016 [69]	AC	BCC	LGG	5×10^6	Hugoniot elastic limit: 2.05 GPa			–
	2019 [62]	BS	BCC	SHPB, C	2,500	2,100	2,350	21.5	–
	2021 [65]	AC	BCC + B2	SHPB, C	1,350	1,520	1,990	7.8 (F)	–
					1,800	1,570	2,000	7 (F)	–
					2,500	1,630	2,090	7 (F)	–
					3,300	1,680	2,250	11 (F)	–
					4,000	1,715	2,350	12 (F)	–
	2022 [72]	AC	BCC	SHPB, C	500	1,310	1,400	4	–
					1,500	1,620	2,005	13(F)	–
					2,500	1,750	2,250	14(F)	–
					500 (773 K)	1,070	1,250	9	–
					1,500 (773 K)	1,200	1,750	18(F)	–
					2,500 (773 K)	1,385	2,130	18(F)	–
$AlCrFeCoNi_{2.1}$	2019 [92]	AC	FCC + B2	SHPB, C	10^3	790	1,450	20	–
				BG	803 m/s	Partial penetration			–
					1,159 m/s	Plug			AS
					1388 m/s	Full penetration			AS
	2021 [93]	Drop-casting	FCC + B2	SHPB, C	1,500	790	1,600	15	–
					2,500	980	1,720	19	–
					3,200	1,000	1,875	30 (F)	–
					2,300 (473 K)	805	1,480	18	–
					2,300 (673 K)	795	1,400	18.5	–
		Suction-assisted casting	FCC + B2	SHPB, C	1,800	910	1,670	14.5	–
					2,300	1,100	1,890	26	–
					3,200	1,100	2.029	37 (F)	AS
					2300 (473 K)	900	1,600	29	–
					2300 (673 K)	810	1,400	28	–
	2023 [94]	AC	$L1_2 + B_2$	LGG	310 m/s	Spall strength: 3.21 GPa			TW
					620 m/s	Spall strength: 3.43 GPa			TW
$Al_{0.4}CrMnFeCoNi$	2019 [79]	CW + A	FCC	SHPB, T	250	400	690	7	–
					550	430	900	16	–
					1,300	434	1000	22 (F)	–
$Al_{0.6}CrMnFeCoNi$	2019 [79]	CW + A	FCC + BCC	SHPB, T	250	455	880	7	–
					550	472	1,185	16	–
					1,300	469	1,105	18 (F)	–
$AlCrFeNi_2Cu$	2016 [99]	AC	FCC + BCC	SHPB, C	955	862	1,100	6.2	–
					2,119	928	1,395	16.1	–
					3,044	1,030	1,640	23 (F)	–
TiVZrNb	2021 [111]	AC	BCC	SHPB, C	3,340	1,845	1,950	10	–
					4,800	1,828	2,050	20	AS
					8,040	1,980	2,250	25(F)	AS
					10,200	2,052	2,350	30(F)	AS
				BG	Release chemical energy at 932 to 1779 m/s				AS
$TiV_{0.5}ZrNb_{0.5}Hf$	2018 [101]	AC	BCC	SHPB, C	4,269	2,750	2,000	45 (F)	–
					5,591	2,600	1,750	62.5 (F)	–
					6,329	2,600	1,700	67 (F)	–

(continued on next page)

Table 1 (*continued*)

Alloy	Year	Processing	Phase	Equipment, load mode	$\dot{\varepsilon}(s^{-1})$	σ_y (MPa)	σ_u (MPa)	ε_u (%)	Additional mechanism
$TiV_{0.5}ZrMo_{0.5}Hf$	2018 [101]	AC	BCC	SHPB, C	5,740	3,010	1,995	71 (F)	–
					6,212	3,250	1,900	76 (F)	–
					6,816	3,250	1,600	86 (F)	–
$TiV_{0.5}ZrHfTa_{0.5}$	2018 [101]	AC	BCC	SHPB, C	2,827	1,220	1,250	26 (F)	–
					3,187	1,210	1,245	30 (F)	–
					3,113	1,250	1,125	30 (F)	–
$TiVZr_{2.0}Nb_{2.0}Hf$	2018 [101]	AC	BCC	SHPB, C	3,597	1,500	1,510	34 (F)	–
					3,756	1,505	1,500	37 (F)	–
$TiZrNbMo_{0.25}HfTa$	2020 [107]	AC	BCC	SHPB, C	2,100	1,510	1,580	28	–
					4,200	1,550	1,630	25	–
					5,300	1,602	1,748	33	–
$TiZrNbMo_{0.5}HfTa$	2020 [107]	AC	BCC	SHPB, C	3,000	1,753	1,890	23	–
					4,200	1,805	1,920	23	–
					5,400	1,854	2,000	16.5	–
$TiZrNbMo_{0.75}HfTa$	2020 [107]	AC	BCC	SHPB, C	2,100	1,750	1,970	12.3	–
					4,500	1,815	1,900	16	–
					6,000	1,870	1,900	19.5	–
TiZrNbHfTa	2016 [95]	AC	BCC	SHPB, C	2,100	1,390	1,415	10	–
					3,450	1,450	1,460	49 (F)	AS
	2020 [96]	AC	BCC	SHPB, C	1,600	1,300	1,370	13	–
					2,600	1,300	1,380	34	AS
					1,600 (673 K)	1,000	1,090	19.5	–
					2,600 (673 K)	1,180	1,200	33.5 (F)	AS
$TiZrHfAl_{0.5}$	2023 [120]	AC	BCC + HCP	SHPB, C	~2,000	1,260	1,480	12	–
					~2,000 (253 K)	1,300	1,620	14.5 (F)	TW
$TiZrHfNi_{0.5}$	2023 [120]	AC	BCC + HCP	SHPB, C	~2000	1,200	1,500	9(F)	–
					~2,000 (253 K)	1,050	1,510	9(F)	TW
$TiZrHfCu_{0.5}$	2023 [120]	AC	BCC + HCP	SHPB, C	~2,000	1,250	1,520	11	–
					~2,000 (253 K)	1,625	1,810	10(F)	TW
$TiZrHfTa_{0.53}$	2017 [47]	AC	BCC + HCP	SHPB, C	950	1,360	1,590	10.4 (F)	–
					1,270	1,469	1,600	8.9 (F)	–
					1,500	1,390	1,580	13.2 (F)	AS
					2,200	1,388	1,570	12.1 (F)	AS
				BG	Penetrate A3 steel plate at 600 and 875 m/s				–
$TiZrHfTa_{0.7}W_{0.3}$	2022 [115]	AC	BCC + HCP	SHPB, C	2,500	1,890	2,430	4 (F)	–
					4,200	1,940	2,450	4.5 (F)	AS
				BG	~2.1 km/s	Penetration depth: 43.5 ± 1.0 mm Penetration channel diameter:23.0 ± 0.1 mm			—
$V_{10}Cr_{10}Fe_{45}Co_{35}$	2019 [104]	CW + A	FCC	SHPB, C	3,000	640	1,925	25.9	PT, TW
					3,000 (77 K)	1,083	2,245	21.6	PT, TW
$V_{10}Cr_{10}Fe_{45}Co_{30}Ni_5$	2019 [103]	CW + A	FCC	SHPB, T	3,200	520	1,028	55.4 (F)	TW
					1,550 (77 K)	650	1,369	56.5	PT, TW
				CP	Charpy impact energy: 112.6 J				PT, TW
					Charpy impact energy (77 K): 110 J				PT, TW

(continued on next page)

Table 1 (*continued*)

Alloy	Year	Processing	Phase	Equipment, load mode	$\dot{\varepsilon}(s^{-1})$	σ_y (MPa)	σ_u (MPa)	ε_u (%)	Additional mechanism
$Cr_{10}Mn_{30}Fe_{50}Co_{10}$	2020 [91]	CW + A	FCC + HCP	SHPB, S	1.37×10^5	601	1,200	210	–
					1.55×10^5	1,650	1,210	225	AS
					1.61×10^5	1,650	1,160	225	AS
		HW + A	FCC + HCP	SHPB, S	1.37×10^5	550	1,060	210	–
					1.55×10^5	1,480	1,150	225	AS
					1.61×10^5	1,490	1,100	260	AS
	2021 [89]	HW + A	FCC + HCP	LGG	187 m/s	Spall strength: 2.21 GPa			TW
					433 m/s	Spall strength: 2.32 GPa			TW
		CW + A	FCC + HCP		187 m/s	Spall strength: 1.89 GPa			TW
					433 m/s	Spall strength: 1.98 GPa			TW
	2021 [90]	HW + A	FCC + HCP	LGG	187 m/s	Spall strength: 2.78 GPa			–
$Cr_{20}Mn_{20}Fe_{40}Ni_{20}$	2022 [114]	HW + CW + A	FCC + σ phase	SHPB, T	1,300	566	1,070	33.3	TW
					3,000	743	1,412	37.5	TW
CrMnFeNi	2022 [121]	HIP	FCC	LGG	304 m/s	Hugoniot elastic limit: 0.67 GPa Spall strength: 1.58 GPa			–-
CrMnFeCoNi	2016 [77]	PM	FCC	SHPB, C	1,200	555	1,100	1.6	–
					1,600	601	1,275	2	–
					2,500	645	1,850	3.4	–
					2,800	698	2,010	4.2 (F)	AS
	2016 [69]	AC	FCC	LGG	5×10^6	Hugoniot elastic limit: 1.65 GPa			TW
	2018 [78]	CW + A	FCC	SHPB, C	3,000	590	1,750	39	–
					3,500	650	1,990	41	–
					4,700	676	2,750	52 (F)	AS
	2018 [85]	PM	FCC	SHPB, C	1,600	590	815	22.5	–
				SHPB, S	–	150	320	~7	TW, AS
	2018 [44]	CW + A	FCC	SHPB, C	2,100	316	600	15	TW
				SHPB, T	1,600	525	734	50 (F)	TW
					2,200	500	740	64 (F)	TW
	2019 [80]	HW	FCC	SHPB, C	750	610	800	18	–
					2,800	605	1,200	50	–
	2019 [81]	A	FCC	SHPB, C	3,000	192	620	40	–
					6,000	200	716	40	TW
					9,000	347	1,123	40	TW
	2019 [45]	CW + A	FCC	SHPB, T	403	390	610	11.5	–
					635	400	780	17.5	–
					1,000	455	610	14 (F)	TW
	2020 [82]	CW + A	FCC	SHPB, C	5,000	320	1,010	23	TW
					8,000	354	1,080	24	TW
	2020 [86]	CW + A	FCC	SHPB, S	50,000	415	1,020	6.2	TW, AS
	2021 [83]	CW + A	FCC	SHPB, C	15,000	–	–	62	AS
	2021 [84]	CW + A	FCC	SHPB, T	7,000	472	1,586	57	TW
	2022 [88]	PM	FCC	SHPB, C	1,200	500	1,120	15	–
					2,800	700	2,060	38	–
				SHPB, S	~410,000	450	635	8.71	AS
$Cr_{26}Mn_{20}Fe_{20}Co_{20}Ni_{14}$	2021 [109]	HT + A	FCC	SHPB, C	1,000	282	533	11.4	TW
					2,000	300	553	22.6	TW
					3,000	360	581	35.8	TW
$Cr_{22}Mn_{14}Fe_{22}Co_{22}Ni_{20}$	2020 [105]	CW + A	FCC	SHPB, C	9,000 (−100℃)	800	2,800	30	TW
					9,000 (−150℃)	850	3,250	30	TW
$Cr_{15}Mn_{20}Fe_{38.5}Co_{20}Cu_{1.5}Si_5$	2021 [108]	AC	FCC + HCP	SHPB, C	1,000	680	1,195	12.2 (F)	–
					1,750	740	1,700	24.1 (F)	–
					2,500	870	2,180	34.7 (F)	PT, TW

(*continued on next page*)

Table 1 (*continued*)

Alloy	Year	Processing	Phase	Equipment, load mode	$\dot{\varepsilon}(s^{-1})$	σ_y (MPa)	σ_u (MPa)	ε_u (%)	Additional mechanism
$Cr_{15}Mn_{30}Fe_{38}Co_{15}Ni_2$	2022 [118]	AC + HW + CW + A	FCC	SHPB, C	1,200	490	710	20	–
					2,900	570	1,275	35	TW
					4,800	620	1,150	20	TW
$Cr_{15}Mn_{30}Fe_{37.9}Co_{15}Ni_2Gd_{0.1}$	2022 [118]	AC + HW + CW + A	FCC	SHPB, C	1,200	450	900	15	–
					2,500	500	1,340	40	TW
					4,800	650	1,345	30	TW
$Cr_{15}Mn_{30}Fe_{37.8}Co_{15}Ni_2Gd_{0.2}$	2022 [118]	AC + HW + CW + A	FCC	SHPB, C	1,300	300	880	20	–
					2,700	410	1,375	42	TW, AS
					5,100	415	1,370	45	TW, AS
$Cr_{26}Fe_{27}Co_{24}Ni_{23}$	2021 [122]	CW + A	FCC	BG	Being fully penetrated by semi-armorpiercing projectiles with a velocity of ~ 840 m/s				TW
	2022 [117]	CW + A	FCC	SHPB, C	2,500	450	992	40	TW
					7,000	600	1,470	40	TW
CrFeCoNi	2019 [45]	CW + A	FCC	SHPB, T	183	370	485	5	–
					495	390	710	14	–
					980	450	620	13 (F)	TW
	2020 [43]	CW + A	FCC	SHPB, T	1,000	354	410	70	–
					3,000	371	555	75 (F)	–
					4,500	426	650	80 (F)	–
					6,000	440	715	77 (F)	TW
	2022 [73]	AC	FCC	SHPB, C	700	350	625	15	–
					2,500	577	1,050	44	–
				SHPB, S	17,300	800	1,220	173 (F)	AS
	2022 [74]	AC	FCC	SHPB, C	2,964	215	870	36	–
					3,614	287	1,005	45	–
				BG	895 m/s	Penetration depth: 4.98 mm Penetration channel diameter: 16.79 mm			–-
					1,136 m/s	Penetration depth: 12.66 mm Penetration channel diameter: 21.19 mm			TW
		A (873 K)	FCC	SHPB, C	2,027	351	785	24	–
					3,998	640	1,000	54	–
				BG	814 m/s	Penetration depth: 4.77 mm Penetration channel diameter: 18.79 mm			–
					1,152 m/s	Penetration depth: 18.73 mm Penetration channel diameter: 22.17 mm			–-
		A (1273 K)	FCC	SHPB, C	2,187	221	710	25	–
					3,863	264	1,000	55	–
				BG	877 m/s	Penetration depth: 4.38 mm Penetration channel diameter: 18.27 mm			–
					1,212 m/s	Penetration depth: 17.90 mm Penetration channel diameter: 22.29 mm			TW
	2023 [76]	HW + A	FCC	LGG	507 m/s	Hugoniot elastic limit: 0.70 GPa Spall strength: 3.15 GPa			TW
					901 m/s	Hugoniot elastic limit: 0.70 GPa Spall strength: 3.28 GPa			TW
$Cr_{10}Fe_{21}Co_{30}Ni_{30}W_9$	2022 [116]	CW + A	FCC + μ	SHPB, C	3,000	400	1,010	25	–
					4,500	438	1,260	45	TW
$Cr_{10}Fe_{23}Co_{30}Ni_{30}Mo_4W_9$	2022 [116]	CW + A	FCC	SHPB, C	3,000	648	1,490	25	–
					4,100	710	1,630	40	TW
$CrFeCoNiMo_{0.2}$	2022 [119]	Selective laser melting	FCC +σ phase	SHPB, C	1,440	790	1,338	13	–
					1,740	820	1,530	16	–

(*continued on next page*)

Table 1 (*continued*)

Alloy	Year	Processing	Phase	Equipment, load mode	$\dot{\varepsilon}(s^{-1})$	σ_y (MPa)	σ_u (MPa)	ε_u (%)	Additional mechanism
$CrCoNiMo_{0.1}$	2021 [110]	CW + A	FCC	SHPB, C	1,003	610	1,065	8	–
$CrCoNiMo_{0.2}$	2021 [110]	CW + A	FCC + σ phase	SHPB, C	967	800	1,590	10	TW
MnFeCoNiCu	2020 [106]	A	FCC	SHPB, C	3,000	400	970	38 (F)	TW
FeNiMoW	2020 [46]	AC	FCC + BCC + μ phase	SHPB, C	2,000	1,200	1,900	28 (F)	TW
				BG	10–20% better penetration performance than conventional tungsten heavy alloys from 876 m/s to 1,330 m/s				Shear band
	2022 [97]	AC	FCC + BCC + μ phase	BG	862	Penetration depth: 14 mm Volume of penetration channel: 1812 mm^3			Shear band
					1,298	Penetration depth: 42 mm Volume of penetration channel: 6886 mm^3			Shear band
					2,130	Penetration depth: 63 mm Volume of penetration channel: 15247 mm^3			Shear band
$W\text{-}Al_{0.5}V_{0.2}Cr_{0.9}FeNi_{2.5}$	2021 [113]	HW + A	FCC + BCC + $L1_2$	SHPB, C	4,000	2,300	2,000	35 (F)	AS

The strain-rate effect is a typical phenomenon in the dynamic deformation of conventional alloys, featured by enhanced yield strength and reversely decreased ductility as the strain rate increases. Fig. 6a and 6b depict the variation of the yield stress and the ultimate strain with increasing the strain rate for the representative HEAs mentioned in Table 1. The compression properties are marked by solid symbols, and the tensile properties are labeled by hollow ones. As shown in Fig. 6a, enhanced yield strength and ultimate strengths with increasing the strain rate can be clearly found in all these representative HEAs [42,43,44,60,65,79,92,96 99,100,109,111,112]. Surprisingly, the ultimate strains of these HEAs also increase as the strain rate increases, as shown in Fig. 6b. Fig. 6c illustrates the changing rate in yield strength versus the changing rate in ultimate strain for plenty of known metals and alloys [148,149,150,151,152,153,154,155,156,157,158,159,160,161,162,163,164,165, 166,167,168,169,170,171,172,173,174,175,176,177,178,179,180]. Herein the changing rate in strength/ductility is defined as the ratio of the strength/ductility variation between the strain rates of $\sim 10^{-3}$ and $\sim 10^{3}\ s^{-1}$. As shown in Fig. 6c, for most conventional alloys and pure metals located in the second quadrant, the increment in yield strength is positive while that in ultimate strain is negative with increasing strain rate. For HEAs, it is common that the higher the strain rate is, the higher the yield strength and the lager the ultimate strain would be, indicating that the strain-rate effect in HEAs is different from that in conventional alloys. To reveal the essence and relevant mechanisms of this difference, the dynamic deformation mechanisms of HEAs are summarized and discussed as follow.

3. Dynamic deformation mechanisms of HEAs

3.1. Dislocation motion under dynamic loads

According to pioneering researches, dislocation motion dominates plastic deformation under the quasi-static loading of HEAs, including 3d HEAs, such as CrMnFeCoNi [22,181] and RHEAs, such as TiZrNbHf [21,182]. Unlike the situation in conventional alloys, various unique microstructures, including pronounced lattice distortion, composition fluctuations and short-range orderings etc., form in HEAs. The consequent pinning at nanoscale and atomic scale leads to the transformation of the slip mode among the planar slip, cross slip and multiple slip for the durable movement in the deformed HEAs. The flexible and complex dislocation motion contributes to a significant enhancement in strain hardening, then a breakthrough of the balance between the strength and ductility, namely the simultaneous promotion of the strength and ductility [21,22,183,184]. Also, SFE would influence the deformation mode of HEAs. The high SFE ($>$45 mJ/m^2) generally leads to the prominent dislocation glide. Whereas additional deformation modes occur in the alloys with decreasing SEF. The intermediate SFE (15–45 mJ/m^2) would stimulate twinning, and low SFE ($<$15 mJ/m^2) would propels phase transformation [185,186,187,188]. Like the situation under quasi-static loading, the dislocation motion is the predominant mode during the plastic deformation of HEAs under dynamic loadings.

3.1.1. Thermal-activation and phonon-drag effects

In the earliest reports on the dynamic-mechanical behavior of HEAs, Wang and Qiao et al. pointed out that the thermally activated dislocation motion and the phonon drag effect jointly resulted in striking strain-rate sensitivity and positive strain-rate effect of HEAs, including $AlCrFeCoNiTi_x$ [55], $AlCrCuFeNi_2$ [99] and $AlCoCr_{1.5}Fe_{1.5}NiTi_{0.5}$ [100].

Specifically, the movement of dislocations needs to overcome two kinds of energy barriers, i.e., short-range and long-range

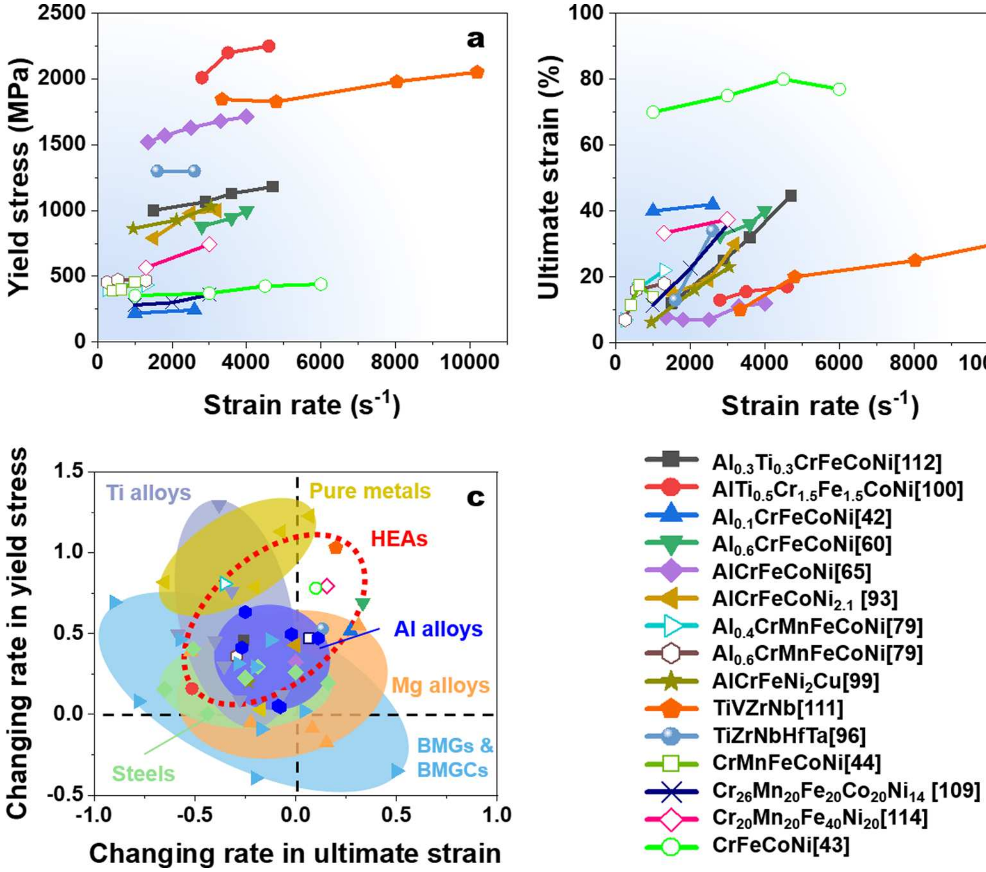

Fig. 6. Strain-rate dependence of (a) yield strength and (b) ultimate strain for representative HEAs. The hollow and solid markers represent compression properties and tensile properties, respectively. (c) The changing rate of yield strength versus the changing rate of ultimate strain with strain rates from of $\sim10^{-3}$ to $\sim10^{3}\,s^{-1}$ for representative HEAs [42,43,44,60,65,79,92,93,96 99,100,109,111,112,114] in comparison with a wide range of material systems including Al alloys [148,149,150,151], Mg alloys [152,153,154,155], Ti alloys [156,157,158,159,160,161], steels [162,163,164,165,166,167,168], bulk metallic glasses (BMGs) & bulk metallic glass matrix composites (BMGCs) [169,170,171,172,173,174,175,176,177], pure metals [155,157,178,179,180].

obstacles. As the temperature increases, the thermal vibration of lattice atoms increases, and the short-range barrier for dislocation movement decreases, which is called thermal activation. However, thermal activation, namely the cumulative frequency at which atomic thermal vibration overcomes the energy barrier, requires a certain reaction time to take effect. Under dynamic loads, the time for dislocation to overcome the short-range obstacles decreases with increasing strain rates, then the thermal-activation effect is undermined. Thus, larger external load is required to overcome the short-range obstacles for dislocation motion, whose macroscopic manifestation is enhanced yield strength. When the strain rate increases to a level close to lattice vibration, the latter will generate an anisotropic resistance to dislocation movement. This anisotropic resistance changes the energy of dislocation, and exhibits as a drag from phonons, the energy quantum of lattice vibration. The phonon drag effect increases with increasing strain rates and local temperatures [189,190] due to higher energy and larger number of phonons. Fig. 7 describes the variation of yield strength as a function of strain rate in the $Al_{0.1}CrFeCoNi$ HEA [42]. As can be seen, the yield strength of $Al_{0.1}CrFeCoNi$ gets enhanced with increasing strain rates owing to the thermally activated dislocation motion and the phonon drag effect. Moreover, significantly higher yield strength and slope are found in the high strain-rate region, indicative of the pronounced impact of phonon drag on dislocation motion.

It is interesting to note that the phonon drag effect and the consequent strain-rate effect cannot be obviously observed in some RHEAs, such as TiZrNbHfTa [96], in the strain-rate range of $10^{2}\sim10^{3}\,s^{-1}$. The reason is that the refractory components possess a large atomic mass and may lead to less lattice vibration and phonons in such systems. At room temperature, the strain rate increasing from 400 s^{-1} to 2,600 s^{-1} cannot enhance the phonon-drag effect. Only when the temperature increases to 673 K can the lattice vibration and effect of viscous resistance become remarkably enhanced, leading to a substantial increment in the yield strength when the strain rate increases, as presented in Fig. 8.

In fact, BCC transition metals generally show a particularly complex response to dislocation motion with a strong temperature- and stain-rate dependence of the flow stress (the critical resolved shear stress) [191]. Direct measurements of dislocation mobility revealed that edge dislocations in BCC metals had a low lattice resistance and, correspondingly, high mobility [192]. This trend indicated that edge dislocations were not essential to the complex response of BCC metals. Instead, screw dislocations along the [111] direction were

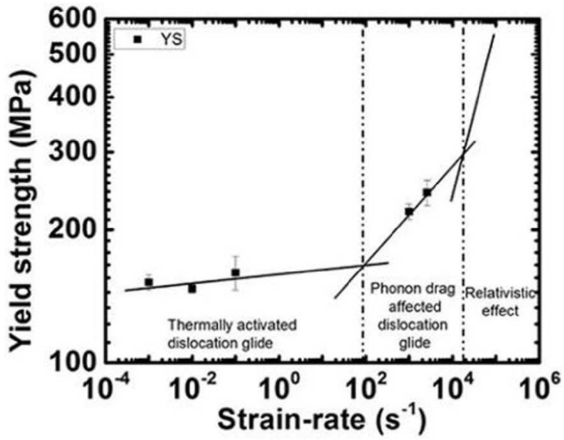

Fig. 7. Yield strength versus strain-rate plot and deformation mechanisms in different regions of the $Al_{0.1}CrFeCoNi$ HEA [42].

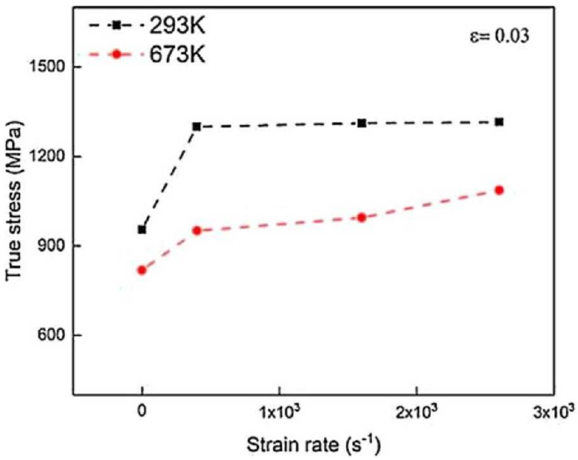

Fig. 8. The flow stress of the TiZrNbHfTa HEA at 0.03 true plastic strain as a function of strain rate (0.001 s^{-1}~2,600 s^{-1}) at a temperature of 293 K and 673 K, respectively [96].

known to exhibit a strong and anisotropic lattice resistance (the so-called Peierls barrier) at low temperatures and high strain rates [193]. So, Song et al. found that the dynamic deformation of the TiZrNbHfTa BCC RHEA was mainly controlled by screw dislocation motion [96].

The strain-rate sensitivity parameter (m) is utilized to describe the dependence of the strength/stress, σ, on the strain-rate, $\dot{\varepsilon}$. It is defined by the slope of the logarithmic strength at a constant strain versus the logarithmic strain rate:

$$m = \frac{\partial ln\sigma}{\partial ln\dot{\varepsilon}} \tag{49}$$

Table 2 summarizes the strain-rate sensitivity parameter, m, in the quasi-static region (m_s), dynamic region (m_d), and the averaged overall value (m_a) of HEAs and some classic metals and alloys. As listed in Table 2, the value of m_d is much larger than that of m_s owing to the thermally-activated dislocation motion with increasing the strain rate and the phonon-drag effect under a dynamic condition. Furthermore, HEAs exhibit a larger m than typical metals and alloys. m is a microstructure-sensitive parameter influenced by microstructural characteristics, such as lattice distortion, grain size, etc. [56,65,62,112]. The discussion on m will be detailed in the later part.

3.1.2. Dislocation multiplication and entanglement

Besides the thermal-activation and phonon-drag effects, rapid dislocation multiplication and consequent dislocation entanglement at high strain rates also affect the dynamic-mechanical behavior of HEAs.

On one hand, the dislocation density will surge during the dynamic deformation of HEAs. In consequence, the dislocation interaction in dynamically-deformed HEAs will be stronger than that in quasi-static deformed alloys. Thus, the work hardening and flow stress will be enhanced during dynamic deformation. For example, Wang et al. found that there emerged stronger dislocation interaction during dynamic deformation than the case of quasi-static deformation in both $AlTi_xCrFeCoNi$ [55] and $AlCrFeNi_2Cu$ [99] HEAs.

Table 2
Strain-rate sensitivity parameter in a quasi-static region (m_s), dynamic region (m_d), and an averaged overall value (m_a) for representative metallic materials.

Material	m_s	m_d	Material	m_a
$Al_{0.1}CrFeCoNi$ [42]	0.0158	0.104	$Al_{0.1}CoCrFeNi$ [59]	0–0.017
$(Al_{0.5}CrFeCoNi)_{0.95}Mo_{0.025}C_{0.025}$ [66]	0.0043	0.192	$Al_{0.3}CoCrFeNi$ [58]	0.006–0.063
$Al_{0.4}CrMnFeCoNi$ [79]	0.039	0.048	$Al_{0.7}CoCrFeNi$ [57]	0.017–0.018
$Al_{0.6}CrMnFeCoNi$ [79]	0.018	0.024	AlCoCrFeNi [62]	0.008–0.016
CrMnFeCoNi [78]	0.0269	0.257	CrMnFeCoNi [44,45,78]	0.022–0.048
$Cr_{15}Mn_{20}Fe_{38.5}Co_{20}Cu_{1.5}Si_5$ [108]	0.007	0.180	CrFeCoNi [45]	0.044
$Cr_{20}Mn_{20}Fe_{40}Ni_{20}$ [114]	0.0172	0.3978	Al [242]	0.028
CrFeCoNi [43]	0.021	0.223	Ni [243]	0.0028
$Cr_{10}Fe_{21}Co_{30}Ni_{30}W_9$[116]	0.0166	0.224	Cu [243]	0.006
$Cr_{10}Fe_{23}Co_{30}Ni_{30}Mo_4W_9$[116]	0.0077	0.293	Fe-14Cr-16Ni [244]	0.006–0.007
FeCoNi [245]	0.0169	–	93 W alloy [246]	0.042
CrCoNi [245]	0.0286	–		
HCP-Mg [247]	~0.01	–		
Al [248]	~0.001	–		
α-Fe [248]	~0.009	–		
FCC-Ni [248]	~0.0028	–		
Cu [249]	~0.0025	0.0215		
$Cu_{0.2}Al$ [249]	–	0.0221		
Cu_2Al [249]	–	0.0422		
Cu_6Al [249]	–	0.0827		
$Fe_{22}Mn_{1.3}Al_{0.6}C$ [250]	0.00741	–		
$Fe_{21}Mn_6Al_{0.6}C$ [250]	0.0246	–		
$Fe_{25}Mn_{1.6}Al_{0.24}Si_{0.08}C_{0.05}Nb$ [144]	0.00890	0.350		
$Fe_{28}Mn_{1.6}Al_{0.28}Si_{0.08}C$ [144]	0.00933	0.120		
304L steel [251]	0.0185	0.0634		
316L steel [251]	0.0267	0.397		

Hence, a higher work-hardening rate was available during dynamic deformation, as shown in Fig. 9. Zhang et al. [112] pointed out that the deformation mode of the dual-phase $Al_{0.3}CrFeCoNiTi_{0.3}$ HEA was dominated by planar glides under dynamic loads. Under a strain rate of 4,700 s^{-1}, the dislocation substructure displayed Taylor lattice (6.5% strain), high-density dislocation walls (16% strain) and intersected microbands (a strain of 29%). The large number of immobile Lomer–Cottrell locks and profuse geometrically necessary dislocations accumulated at the phase boundaries phenomenally-enhanced the strength and work-hardening capacity. The coupling of microband-induced plasticity effect and FCC phase contributed to large dynamic ductility. The yield strength, the ultimate strength, and the ultimate strain of $Al_{0.3}CrFeCoNiTi_{0.3}$ HEAs were 1,181 MPa, 1,880 MPa, and 40%, respectively.

Particularly, Zhao et al. [109] utilized electron-backscatter diffraction (EBSD) to characterize the improved dislocation multiplication with the strain rate in the $Cr_{26}Mn_{20}Fe_{20}Co_{20}Ni_{14}$ HEA. As shown in Fig. 10a − 10c, the misorientation increases with rising strain rate in EBSD, revealing that the higher density of dislocations tend to accumulate at higher strain rates. The dislocation density can be calculated according to the following equation [194]:

$$\rho = \frac{2\theta_{KAM}}{xb} \tag{50}$$

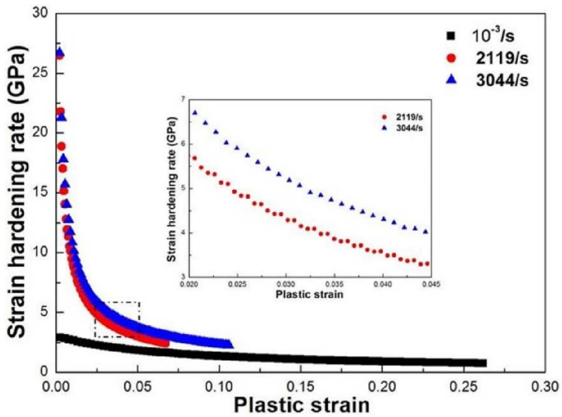

Fig. 9. Strain hardening rate as a function of plastic strain at different strain rates in the $AlCrFeNi_2Cu$ HEA [99].

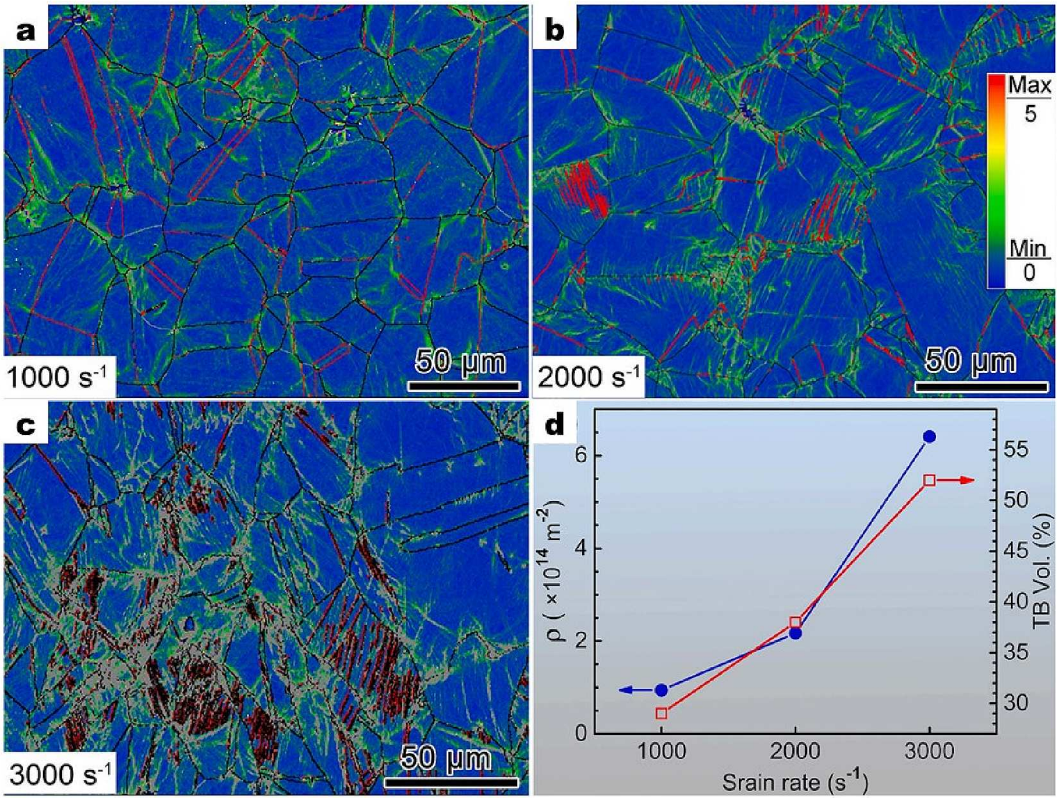

Fig. 10. Kernel average misorientation maps of the $Cr_{26}Mn_{20}Fe_{20}Co_{20}Ni_{14}$ HEA deformed at (a) 1,000, (b) 2,000 and (c) 3,000 s^{-1}, respectively. (d) Variations of dislocation densities (ρ) and volume fraction of twin boundary (TB Vol.) of the samples deformed at different strain rates [109].

where ρ is the dislocation density, θ_{KAM} is the kernel average misorientation, x is the unit length, twice that of the step size used in EBSD acquisition, and b is the magnitude of Burgers vector. The calculated results showed that the dislocation density of the $Cr_{26}Mn_{20}Fe_{20}Co_{20}Ni_{14}$ HEA increased substantially from 9×10^{13} m^{-2} at 1,000 s^{-1} to 2.17×10^{14} m^{-2} at 2,000 s^{-1}, and further to 6.41×10^{14} m^{-2} at 3,000 s^{-1} (see Fig. 10d). Song et al. [93] revealed that the fraction of $2^\circ - 15^\circ$ low-angle grain boundaries, which mainly resulted from the dislocation accumulation during plastic deformation, increased from 67.6% for the $AlCrFeCoNi_{2.1}$ HEA deformed at 0.001 s^{-1} with a strain of 30% to 74.2% for the sample deformed at 3,000 s^{-1} with a strain of 27%. The dislocation cells originating from high-density dislocation tangles at high strain rates contributed to apparent work hardening and strain-rate sensitivity of the $AlCrFeCoNi_{2.1}$ alloy. Dai et al. [84] estimated the dislocation density of the CrMnFeCoNi HEA at different states. Per their report, the dislocation densities of undeformed, quasi-static, and dynamic tensile CrMnFeCoNi alloy specimens were 2.60×10^{13}, 7.62×10^{14}, and 1.19×10^{15} m^{-2}, respectively. Moreover, they also observed a higher density of dislocation clusters and dislocation cells with a smaller size in dynamic-tensile specimens. Since the average diameter of dislocation cells is considered inversely proportional to the square root of the dislocation density, a high dislocation density was further verified by this observation. The high dislocation density mainly determined the high flow stress of the CrMnFeCoNi alloy under dynamic loading. Its yield strength and true ultimate strength were 472 MPa and 1,586 MPa at a strain rate of 7,000 s^{-1}, which were 18% and 52% higher than quasi-static ones, respectively.

Similarly, Gu et al. [110] derived the dislocation density from the full-width half-maximum of the major peaks in the XRD patterns of the $CoCrNiMo_x$ HEAs using the Williamson-Hall method [195,196].

$$\delta\frac{cos\theta}{\lambda} = \alpha + 2\varepsilon\frac{sin\theta}{\lambda} \tag{51}$$

$$\alpha = \frac{0.9}{D} \tag{52}$$

$$\rho = 14.4\frac{\varepsilon^2}{b^2} \tag{53}$$

where δ, θ, λ, ε, D, ρ, and b are the peak width, diffraction angle, X-ray wavelength, strain, average grain size, dislocation density, and the magnitude of the Burgers vector, respectively. The calculated average dislocation densities of the $CrCoNiMo_x$ HEAs deformed at ~1,000 s^{-1} were $(2.69 \pm 0.97) \times 10^{15}$ m^{-2}, $(3.2 \pm 1.65) \times 10^{15}$ m^{-2} and $(7.63 \pm 2) \times 10^{15}$ m^{-2} with increasing x from 0 to 0.2. More

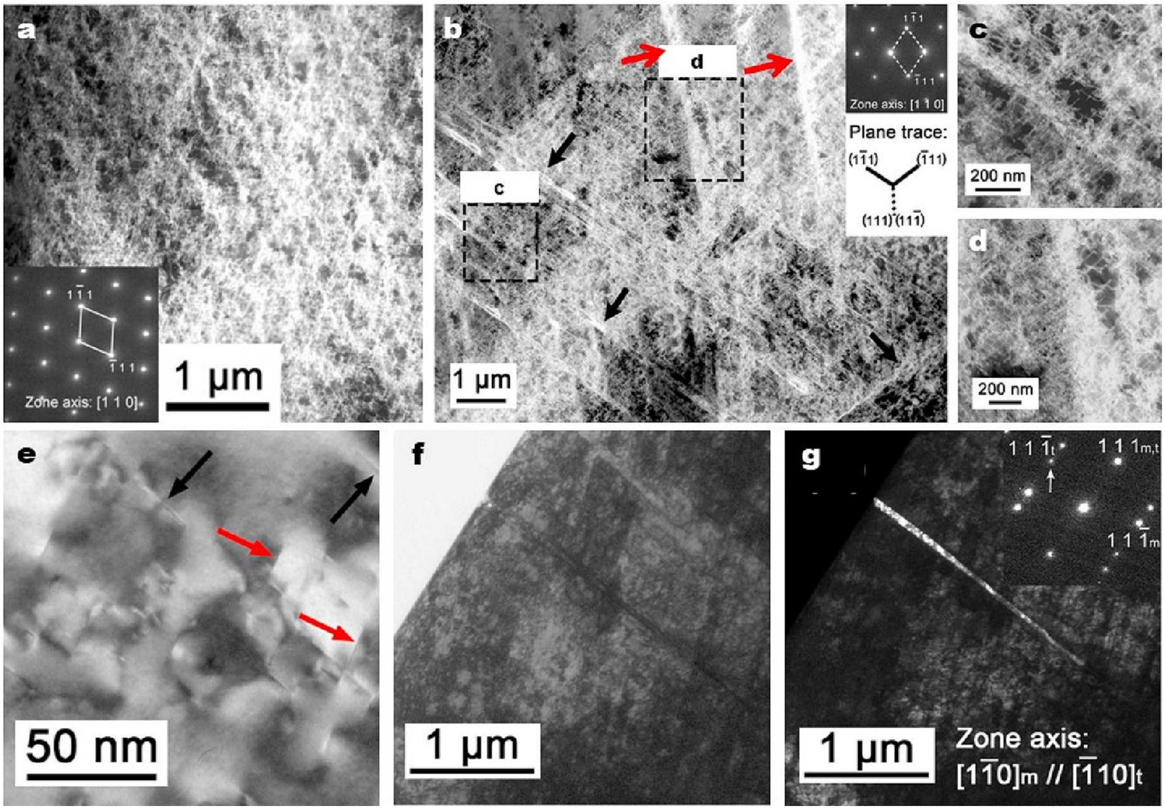

Fig. 11. Deformed structures with a 40% strain in CrMnFeCoNi deformed at (a) 3,000 s^{-1} and (b) - (g) 6,000 s^{-1} [81].

pronounced dislocation accumulation contributes to a higher work-hardening rate and enhanced flow stress in the $CoCrNiMo_{0.2}$ HEA.

Dirras et al. [95] further reported that the flow stress caused by dislocations can be expressed by the Taylor equation [134]. Based on XRD result, the average dislocation density of the TiZrNbHfTa HEA deformed at a high strain rate (4,700 s^{-1}) was 47 ± 7 × 10^{14} m^{-2}, about triple that of a quasi-statically- compressed specimen (15 ± 2 × 10^{14} m^{-2} [197]). The calculated flow stress (1,236 MPa) was very close to the experimental flow stress (1,228 MPa), demonstrating that a large dislocation density is indeed the major cause of high flow stresses at high strain rates.

On the other hand, the dislocation multiplication and dislocation entanglement can influence the dislocation-motion mechanism and the fracture mode of HEAs. For example, Yang et al. [81] studied the deformation mechanism of the CrMnFeCoNi HEA at different strain rates. It was found that dislocation slip dominated the deformation at different strain rates. Meanwhile, dislocation cells formed due to serious dislocation entanglement at the strain rate of 3,000 s^{-1} (see Fig. 11a). As the strain rate increased to 6,000 s^{-1}, a large number of high-density dislocation walls formed, characterized by the gliding of numerous dislocations on {1 1 1} planes (see Fig. 11d − 11d). Such dislocation walls could offer an extra strain-hardening effect and consequently, a high flow stress during deformation. Hence, some stacking faults (SFs) (see Fig. 11e) and nano-twin (see Fig. 11f and 11 g) could be observed in the sample strained at 6 × 10^3 s^{-1} due to the trigger from the high flow stress.

Additionally, dislocations, which proliferated rapidly, would accumulate at the grain boundaries of the CrMnFeCoNi HEA according to the discovery of Wang et al. [77]. These local hotspots weakened the bonding force between grains, then the grain boundaries collapsed and micropores formed gradually. When the continuously increasing local stress was larger than the bonding strength of the grains, cracks initiated along the grain boundaries. As a result, there emerged an intergranular fracture in the dynamic deformation of the CrMnFeCoNi HEA which generally displays the good ductility under a quasi-static loading. Dai et al. [84] reported the multiple fracture characteristics in the CrMnFeCoNi HEA after dynamic tensile deformation. Although dimple fracture remained as the dominant fracture characteristic, which was similar to that of quasi-static tensile specimens, quasi-cleavage fracture emerged, characterized by tearing dimples, river patterns, and tearing ridges on the fracture surface of dynamic deformed specimen. Moreover, the dimples and quasi-cleavage fractures were staggered with clear boundaries between these two fracture types, suggesting a transition from ductile to brittle with increasing strain rates. As reported by Yang et al. [90], the voids also preferentially nucleated at the grain boundaries of the $Cr_{10}Mn_{30}Fe_{50}Co_{10}$ HEA with good ductility under quasi-static loading due to the rapidly proliferating dislocations. As a result, voids connected to form microcracks at a high rate of 190 m/s.

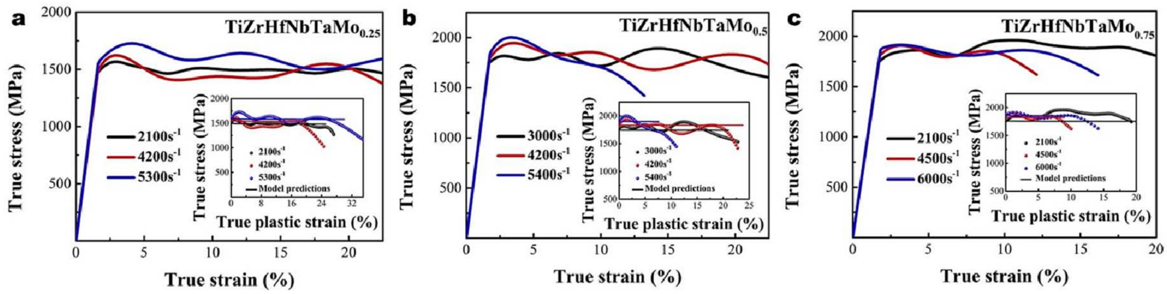

Fig. 12. The true stress–strain curves of (a) $TiZrHfNbTaMo_{0.25}$, (b) $TiZrHfNbTaMo_{0.5}$, and (c) $TiZrHfNbTaMo_{0.75}$ under dynamic loads at room temperature [107].

3.2. *The effect of intrinsic microstructures on dynamic deformation in HEAs*

Apart from the strain rate, several intrinsic microstructure characteristics generally present in undeformed alloys at different scales also have notable influence on dislocation motion and resultant mechanical behavior in HEAs under dynamic loading.

3.2.1. *Lattice-distortion effect*

In general, lattice distortion is considered as the intrinsic characteristics of HEAs [20,18,198]. In HEAs, a simple solid solution composed of multiple elements will form under the effect of the high mixing entropy. The disordered squeeze of the constituent atoms with various atomic radii, valence electron concentrations, etc. inevitably distort the solid-solution lattice of HEAs. The distorted lattice will lead to a local elastic strain field, which can hinder dislocation motion, generating solid-solution-strengthening effect [199,200]. As a result, HEAs generally manifest a higher strength and hardness than conventional alloys under quasi-static loads [17,201,202,203,204].

Under dynamic loads, lattice distortion plays a similar role in hindering dislocation motion to those under quasi-static load. For example, Qiao et al. [107] reported that the degree of the lattice distortion of the $TiZrHfNbTaMo_x$ alloy increased significantly with the increase of Mo content. Thus, the yield strengths of $TiZrHfNbTaMo_x$ increased from 1,555 MPa to 1,820 MPa at ~4,500 s^{-1} when x increased from 0.25 to 0.75, as indicated by the red curves in Fig. 12. Under an impact load in which the strain rate is higher than 10^5 s ^{1}, the average Hugoniot elastic limit, normally known as the transition point from elastic state to elastic–plastic state, of the FCC-HEA CrMnFeCoNi and BCC-HEA AlCrFeCoNi, reached 1.64 GPa and 2.05 GPa at $\sim 5.0 \times 10^6\ s^{-1}$, respectively [69]. According to the opinion of Dai et al., these values are both remarkably higher than those of conventional alloys with similar compositions in spite of slighter lattice distortion degree. On this basis, He et al. [65] and Gangireddy et al. [58,59] proposed that the effect of the lattice friction stress resulting from lattice distortion would rapidly increase with the fast proliferation of dislocations at high strain rates, and further resulted in a higher strain-rate sensitivity, compared with conventional alloys, as listed in Table 2.

Surprisingly, the dislocation motion under a dynamic load could overcome the resistance from the distorted lattice, which generally yields a pile-up of dislocations under a quasi-static load. As a consequence, the dynamic strength is enhanced by the lattice distortion and solid-solution strengthening effect, whereas the plasticity is not traded off. For instance, the yield strength of the $TiZrHfNbTaMo_{0.5}$ HEA reached 1.8 GPa while the fracture strain was >23 % at 4,200 s^{-1}, as exhibited in Fig. 12b [107].

3.2.2. *Short-range orderings*

Short-range orderings refer to the microstructures that chemically or topologically deviate from randomness at the interatomic scale, including A-A/B-B atomic pairings [205,206], nanodomains/superlattice [207,208,209,210], ordered interstitial complexes [21,211], and topological ordering [212,213]. Although HEAs are generally considered as solid solutions with disordered atomic occupancy, the complex interactions between the constituent elements often lead to some orders at atomic scale. short-range orderings can induce a pinning effect on dislocation motion at the atomic scale, promoting the transformation of dislocation slip mode under quasi-static load. One typical example is the replacement of Mn by Pd in the CrMnFeCoNi HEA reported by Yu et al. [22], in which Pd possesses greater difference from the rest of the principal elements, thus reducing the uniformity of the element distribution. The pinning effect of alternating tension and compression strain field from atomic-scale composition fluctuation on dislocation promotes a transition from plane slip to cross slip. Lu et al. [21] introduced ordered oxygen complexes in the TiZrHfNb HEA by doping 2 atomic percent oxygen. It showed that ordered oxygen complexes not only changed the dislocation slip mode from a planar slip to wavy slip but also induced double cross-slip.

Under a dynamic load, the short-range orderings in HEAs also play an essential role in dislocation movement. According to Qiao et al., the short-range orderings in the NiCoCrFe [43] and $Fe_{40}Mn_{20}Cr_{20}Ni_{20}$ [114] HEAs can produce strong short-range obstacles for dislocation movement, endowing the alloy with higher strain-rate sensitivity and positive strain-rate effect compared with common coarse-grained FCC HEAs as listed in Table 2. For NiCoCrFe HEA, the yield strength (440 MPa) at 6,000 s^{-1} is twice the quasi-static yield strength, as shown in Fig. 13. In $Fe_{40}Mn_{20}Cr_{20}Ni_{20}$ HEA deformed at high strain rates when the thermal activation of dislocations gradually fails, short-range orderings could limit the dislocation slip to a smaller scale and lead to deformed sub-grains. As a result, it exhibits the highest dynamic strain-rate sensitivity ($m = 0.3978$) among all reported HEAs.

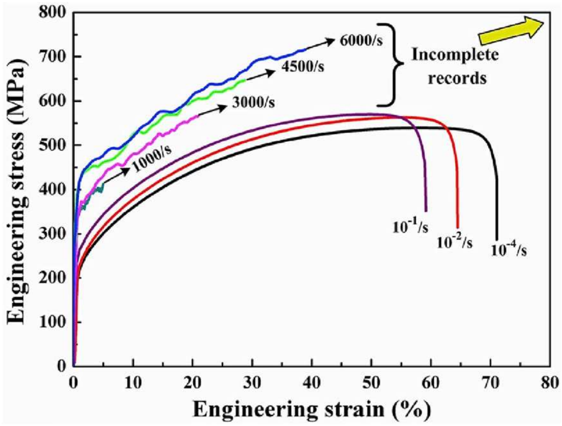

Fig. 13. The engineering stress–strain curves of CrFeCoNi HEA at various strain rate [43].

3.2.3. *Gran boundary*

Up to now, nearly all reported bulk HEAs are polycrystalline materials with coarse grains or fine grains. Hence, the properties of HEAs are inevitably affected by grain boundaries, which generally hinder the dislocation motion due to the irregular arrangement of atoms and larger lattice distortion [214]. The smaller the grain size is, the larger the grain boundary area, and the higher the yield strength will be, following the classic Hall-Petch relationship (Eq. (54)), regardless of quasi-static or dynamic loads [215,216,217].

$$\sigma = k_y d^{-\frac{1}{2}} \tag{54}$$

where d is the mean grain size, and k_y is the Hall-Petch constant.

Under quasi-static load, the yield strength of HEAs, such as CrMnFeCoNi [218], $Al_{0.1}$CrNbVMo [219] and HfNbTaZrTi [220], follows the Hall-Petch relationship. Although fine-grain alloys exhibit higher yield strength than coarse-grain alloys, a large number of dislocations normally pile up at grain boundaries, causing stress concentration and microcrack. Therefore, the ductility is usually deteriorated with grain refinement.

Under dynamic loads, the effects of grain boundaries and grain size on the dynamic-mechanical properties of HEAs are similar to those under quasi-static load. As depicted in Fig. 14, for the CrMnFeCoNi HEA reported by Lu et al. [44], when the average grain size decreased to 12 μm, the yield strength at 2,100 s^{-1} reached 361 MPa, 30% higher than that of the coarse-grain alloy A with an average grain size of 450 μm. In addition, the plasticity of FeCoNiCrMn HEAs under quasi-static and dynamic loads is similar, because the energy provided by dynamic loads enables the dislocations to overcome the resistance at grain boundaries. Gu et al. [110] found that the $CrCoNiMo_{0.2}$ HEA with grain sizes of 12.5 μm and 6.4 μm in precipitate-free regions and precipitate-dense regions was obtained by cold-working and recrystallization annealing, respectively. This fine-grain HEA maintained a high work-hardening rate of 6,350 MPa and a decent plasticity of ~10% during dynamic deformation at the strain rate of 967 s^{-1}.

It is worth noting that a large number of grain boundaries in fine-grain HEAs will determine their strain sensitivity. Gangireddy et al. [59] discovered that the recovered grains in the $Al_{0.1}$CrFeCoNi HEA would lower the strain sensitivity to 0.008. Xue et al. [62] demonstrated that the AlCrFeCoNi HEA with equiaxed grains (H2400) and columnar crystals (H200) both exhibited a positive strain-rate effect. The strain-rate sensitivity parameter of the H200 alloy with a grain size of ~200 μm reached 0.016, nearly 50% higher than that of H2400 alloy with a grain size of ~80 μm, as shown in Fig. 15d. In addition, given the fact that the oriented texture caused by the heat conduction direction during solidification is beneficial to dislocation slip during plastic deformation, H200 with columnar crystals exhibited better ductility (~43%) at the strain rate of 2,500 s^{-1} (see Fig. 15a).

3.2.4. *Additional phases (heterostructure)*

Although HEAs were initially regarded as single-phased solid solutions in early researches, more and more researchers have begun to pay attention to the effect of multi-phases in HEAs since the report of eutectic HEAs [26] and transformation-induced plasticity (TRIP) dual-phased HEAs [25] in 2014 and 2016, respectively. Previous reports successfully revealed that the structure, size, quantity and distribution of additional phases, or heterostructure at different scales, play a crucial role in the mechanical properties of HEAs. For instance, the synergy between the soft FCC phase and the hard B2 phase promotes deformation homogeneity and delays necking, thus endowing the cast $AlCrFeCoNi_{2.1}$ eutectic HEA with a quasi-static tensile strength of 944 MPa and an elongation of 25.6%, respectively [26]. By introducing uniformly-distributed $L1_2$ coherent nano-precipitates, the quasi-static yield strength of $Al_{0.5}Cr_{0.9}FeNi_{2.5}V_{0.2}$ HEAs is higher than 1 GPa while the fracture elongation is 17% [221].

Under dynamic loading with high strain rates, additional phases, including solid solutions with different structures and precipitated ordered complexes, have a vital impact on the dislocation motion and the mechanical properties of HEAs as well.

Firstly, the presence of additional phases generally reduces the strain-rate sensitivity of HEAs. In the cases of Al_xCrMnFeCoNi HEAs constituted by different phases reported by Peng et al. [79], the strain-rate sensitivity of $Al_{0.4}$CrMnFeCoNi HEAs with a single FCC structure (m = 0.039–0.048) was significantly higher than that of $Al_{0.6}$CrMnFeCoNi HEAs (m = 0.018–0.024) with an FCC + BCC dual-

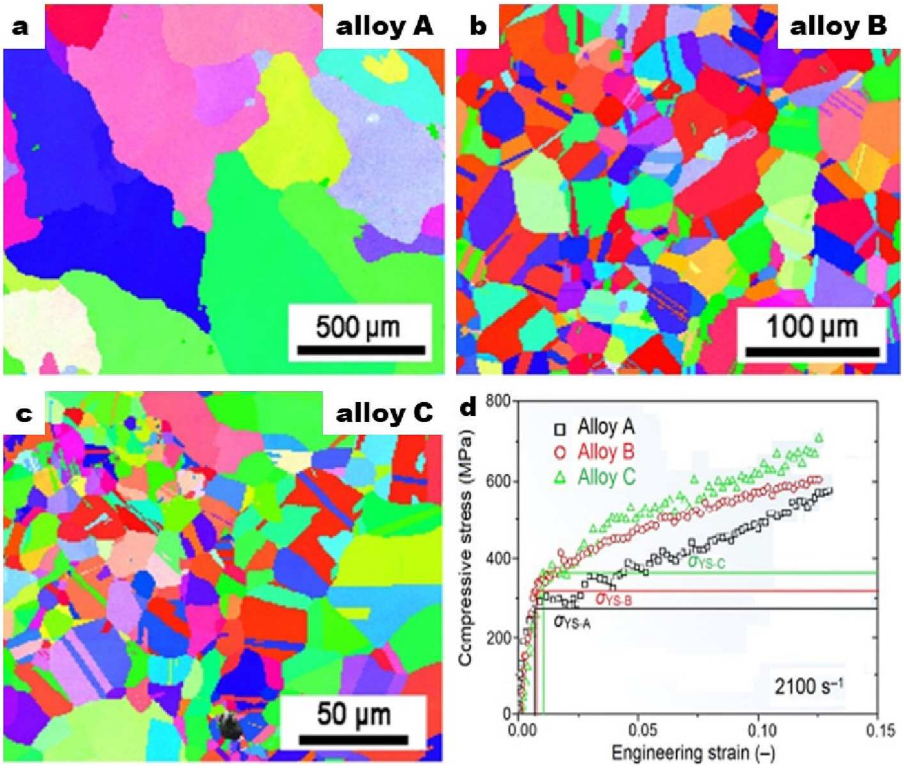

Fig. 14. Inverse pole figure (IPF) results exhibiting randomly-orientated grains with different grain sizes of alloys (a) A, (b) B, and (c) C, and (d) engineering strain–stress curves of alloy A, B, and C under dynamic loads [44].

phase structure, as displayed in Fig. 16. Similarly, compared with the single-phased FCC $Al_{0.3}CrFeCoNi$ HEA with high m_a (0.053) [56], the $Al_{0.7}CrFeCoNi$ HEA with lamellar dual-phase microstructure possesses a considerably smaller value of $m_a = 0.017–0.018$ [61].

Secondly, dual-phase HEAs generally manifest a higher yield strength and a greater strain-hardening rate. One typical example is that the presence of nanoscale $L1_2$ precipitates coherent with the FCC matrix deriving from low-temperature annealing could increase the resistance of dislocation motion without generating dislocation pile-up [61]. Hence, while the strain-rate sensitivity of the $Al_{0.7}CrFeCoNi$ HEA with an FCC + B2 dual-phase lamellar structure will not be affected, the dynamic flow stress can reach 2,150 MPa along with a work hardening of >500 MPa. According to Gwalani et al. [64], the annealing-derived dispersive B2 phases could cause a lattice mismatch between B2 phase and FCC solid-solution matrix. Consequently, the yield strength and the ultimate strength of $Al_{0.5}CrFeCoNi$ HEAs at 2,000 s^{-1} increased from 682 MPa and 1,168 MPa to 1,352 MPa and 1,503 MPa, respectively. Wang et al. [66] reported that the yield strength of the $(Al_{0.5}CrFeCoNi)_{0.95}Mo_{0.025}C_{0.025}$ HEA prepared by powder metallurgy could reach 1,055 MPa at 3,000 s^{-1} due to dispersed $M_{23}C_6$ carbides. Gu et al. [110] showed that the enhanced dynamic yield strength of the $CoCrNiMo_x$ ($x = 0$, 0.1, and 0.2) HEAs ranging from ~ 450 MPa to ~ 800 MPa (Fig. 17c) was mainly attributed to the precipitation (σ phase) hardening resulting from supersaturated Mo. The presence of the σ precipitations induced the vast occurrence of stacking faulting/nano-twinning (Fig. 17a) and microbanding (Fig. 17b) in the $CoCrNiMo_{0.2}$ alloy, which could act as both full and partial dislocation sources. The strain-hardening ability and plastic deformation ability under dynamic condition were thereby improved via microband-induced plasticity effect and twinning-induced plasticity effect as shown in Fig. 17c and 17d. The W-$Al_{0.5}Cr_{0.9}FeNi_{2.5}V_{0.2}$ HEA containing $L1_2$ precipitations exhibited a rather high yield strength above 2,300 MPa at $\sim 4 \times 10^3$ s^{-1}, which is much higher than the value of ~1,800 MPa ($\sim 5 \times 10^3$ s^{-1}) in conventional W-NiFe obtained by liquid phase sintering [113].

Thirdly, the complex multiphase will hinder the propagation of microcracks in HEAs. An example is illustrated by the hot-rolled and subsequently quenched $Fe_{50}Mn_{30}Co_{10}Cr_{10}$ HEA with more martensites (46 wt%) [89]. It exhibits lower crack propagation rates, lower damage rates, and higher spall strength (2.21 GPa and 2.32 GPa with the velocity of 190 and 420 m/s) under impact loading, as shown in Fig. 18a.

3.3. The effect of associated microstructure on dynamic deformation in HEAs

Besides strain rate and intrinsic microstructures, several associated microstructures formed during the process of dynamic deformation, such as twinning, phase transformation, and adiabatic shear, also play a non-ignorable role in the dynamic deformation of HEAs. Fig. 19 summarizes the number of reports regarding phase transformation, twinning, and adiabatic shear effects in HEAs with different structures. As can be seen, the phase transformation effect has only been reported in 3 metastable HEAs, i.e. $V_{10}Cr_{10}Fe_{45}Co_{30}Ni_5$ [103],

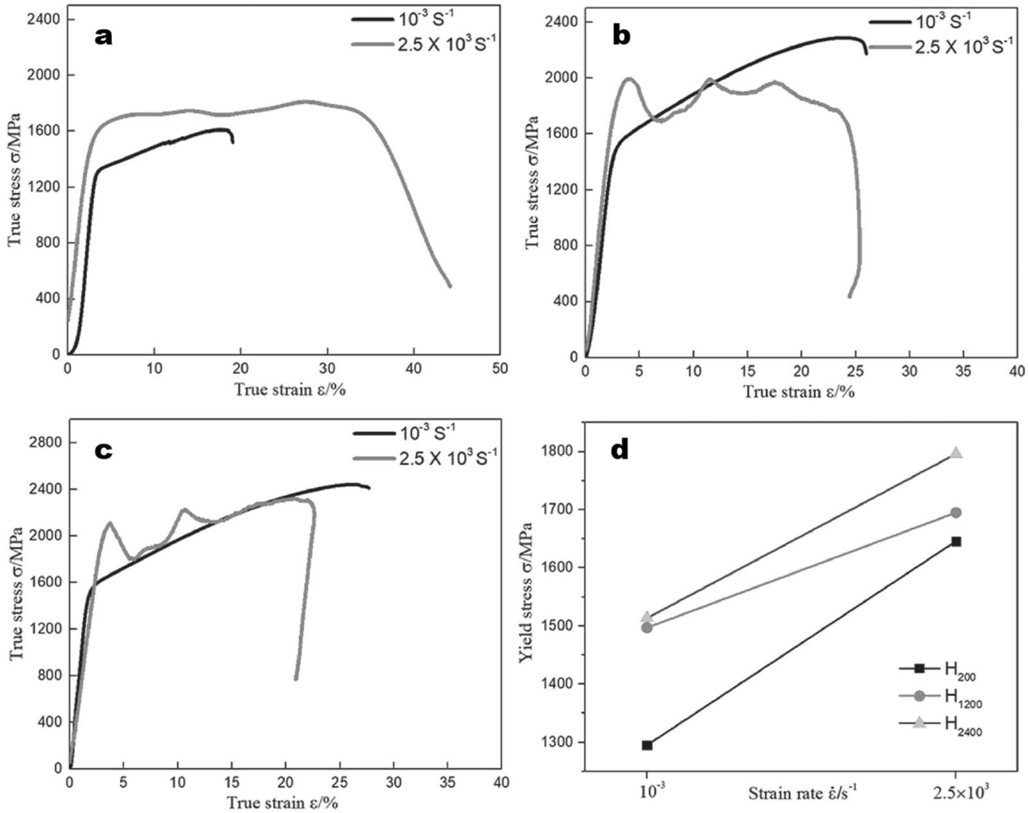

Fig. 15. True strain–stress curves of the AlCrFeCoNi HEAs with (a) 200, (b) 1200, and (c) 2400 μm/s Bridgman solidification withdrawal velocities. (d) The variation of yield strength with strain rate [62].

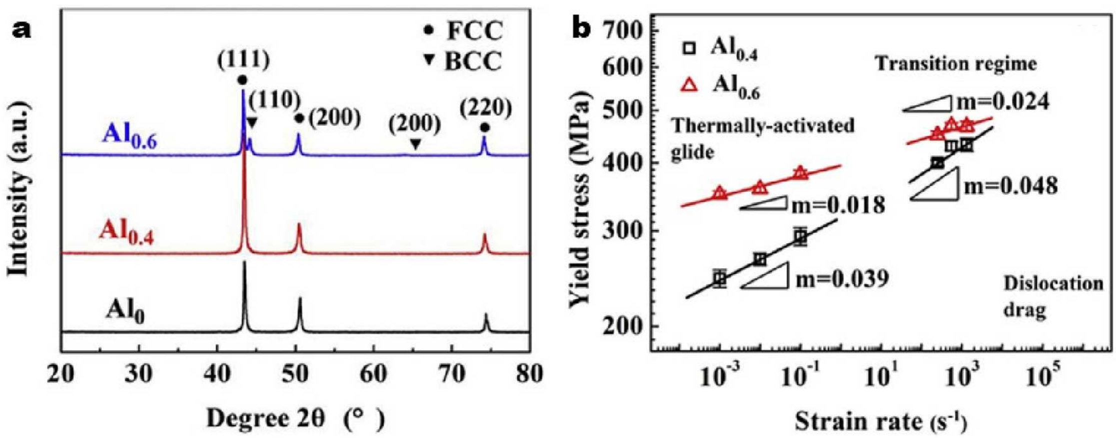

Fig. 16. (a) XRD patterns and (b) yield stress versus strain rate curves of the $Al_xCrMnFeCoNi$ alloys [79].

$V_{10}Cr_{10}Fe_{45}Co_{35}$ [104] and $Cr_{15}Mn_{20}Fe_{38.5}Co_{20}Si_5Cu_{1.5}$ [108] (see Table 1). Twinning occurs within a wide range of strain rates in almost all 19 HEAs containing FCC phase [42,43,44,45,46,58,59,60,61,63,69,76,81,82,84,85,86,89,94,103,104,105,106,108,109,110,118,122] and 3 HEAs with BCC + HCP phase [120]. The adiabatic shear effect can be observed in 18 HEAs with all kinds of phase compositions [46,47,56,63,66,68,77,78,83,85,86,91,92,93,95,96,111,112,113,118].

3.3.1. Twinning of HEAs under dynamic loads

As one kind of deformation mechanism, twinning is produced by the movement of partial dislocations, and more likely to occur in the alloys with low SFE, such as Mg alloy [222] and FCC-HEAs (SFE = 20–40 $mJ \cdot m^{-2}$) [223]. As reported by Gludovatz et al. [29], the twinning effect of CrMnFeCoNi HEAs was activated during quasi-static deformation at low temperatures (77 K). The formation of

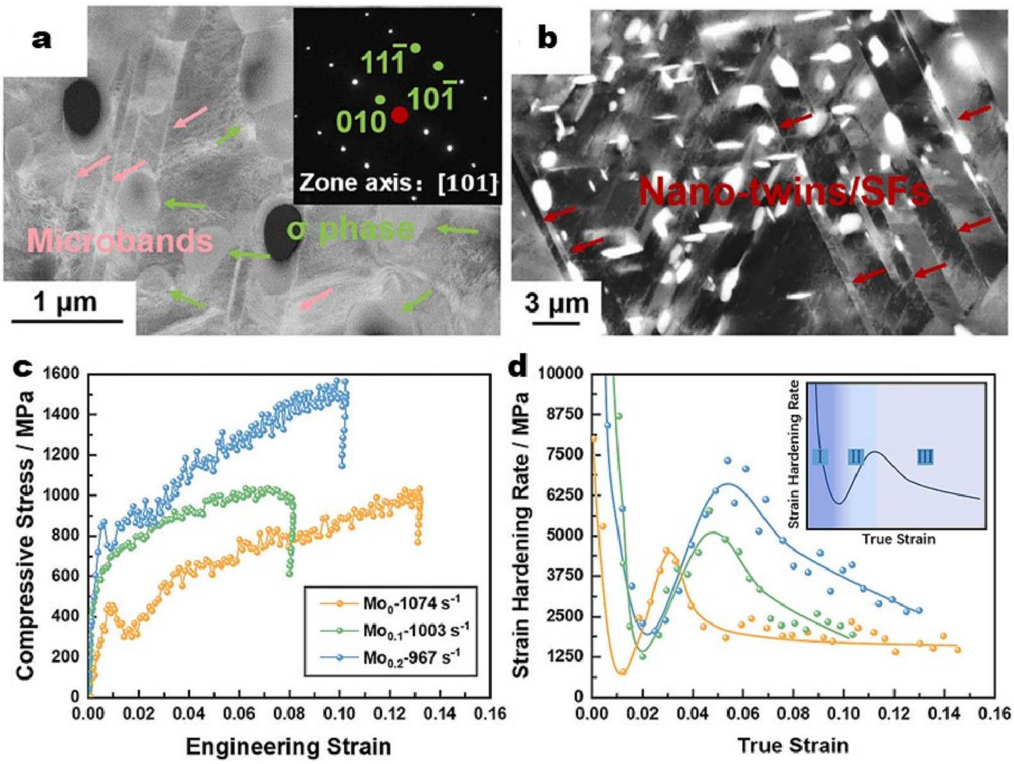

Fig. 17. TEM observations of as-deformed $CoCrNiMo_{0.2}$ HEA: (a) microbands and precipitates with corresponding SAED pattern and (d) STEM-TEM image of microbands, precipitates and nano-twins/SFs. (c) Compressive stress–engineering strain curves and (d) strain hardening response for the dynamic deformed $CoCrNiMo_x$ HEAs [110].

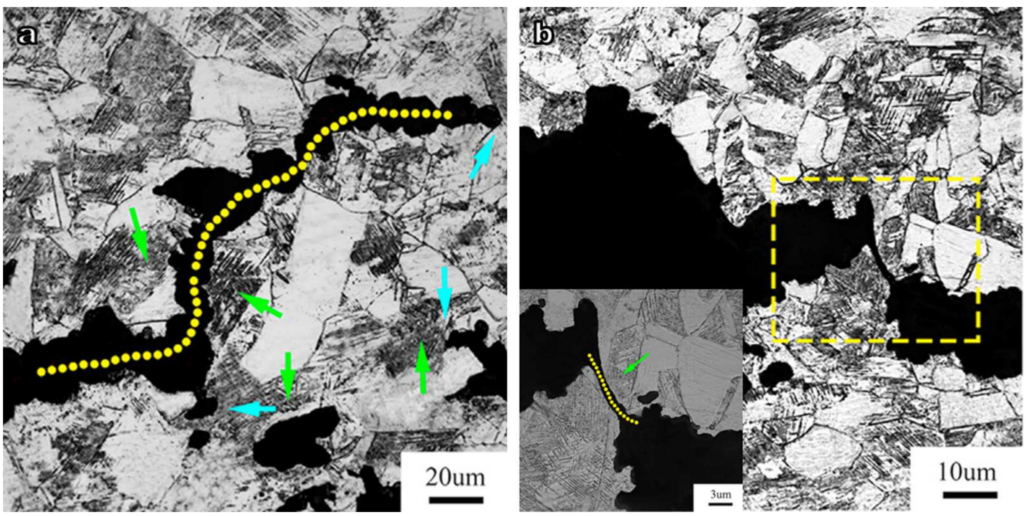

Fig. 18. Propagation characteristics of micro-cracks under 420 m/s impact loading: (a) hot-rolled + quenched sample and (b) cold-rolled + quenched sample [89].

deformation twins in the CrMnFeCoNi HEA led to a decrement in the mean free path of dislocation motion and an increment in strain hardening. Therefore, the yield strength and the ductility of the CrMnFeCoNi HEA increased simultaneously by ~ 85% and ~25% to 759 MPa and >70%, respectively, as the temperature decreased from 293 K to 77 K. According to the research conducted by Bi et al. [224], twinning in the $Cr_{20}Fe_6Co_{34}Ni_{34}Mo_6$ HEAs contributed to a high yield strength of ~1.1 GPa and a high strain hardening of ~2 GPa, respectively. For the CoCrNi alloy with a SFE value of 22 ± 4 mJ·m^{-2}, the severe plastic deformation and large fracture toughness

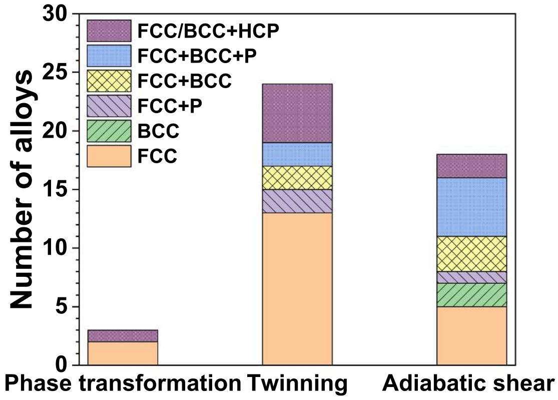

Fig. 19. Distribution of deformation mechanisms under dynamic loads in HEAs with various microstructures [42,43,44,45,46,47,56,58,59,60,61,63,66,68,69,76,77,78,81,82,83,84,85,86,89,91,92,93,94,95,96,103,104,105,106,108,109,110,111,112,113,118,120,122]. P represents precipitation.

resulted from the formation and bridging of twins at nanoscale at room temperature, which could inhibit the expansion of cracks, as reported by Laplanche et al. [225] and Yu et al. [226].

It is evident that the effect of twinning is favorable of improving the mechanical properties of HEAs under a quasi-static load. Briefly summarized, twinning in HEAs under dynamic loads has following characteristics:

(a) Improved mechanical properties

The $Al_{0.1}CrFeCoNi$ HEA with single FCC structure reported by Mishra et al. [42] exhibited a high strain-rate sensitivity and a high strain-hardening rate due to twin deformation during dynamic deformation. On this basis, Gangireddy et al. [59] found that different types of twins played dissimilar roles in dynamic deformation. In the cold-rolled $Al_{0.1}CrFeCoNi$ HEA, the contribution of long-range barriers including dislocation entanglement and deformation twins is not sensitive to the strain rate or temperature. Hence, the strain-rate sensitivity of the cold-rolled $Al_{0.1}CrFeCoNi$ HEA is close to 0. By contrast, the annealing twins obtained by recovering at 893 K can significantly improve the strain-rate sensitivity, reaching a value of strain-rate sensitivity parameter $m = 0.014$ in annealed $Al_{0.1}CrFeCoNi$ HEA at $\sim 10^3\ s^{-1}$.

According to Lu et al., the appearance of nano-twins facilitated the ultimate tensile strength and the elongation of the CrMnFeCoNi HEA to increase by 124 MPa and 3% to 745 MPa and ~63%, respectively, when the strain rate was transformed from quasi-static to dynamic (2,200 s^{-1}) [44]. The research by Dai et al. [84] further indicated that the cooperation of twins and dislocations contributed to the simultaneous enhancement of strength and ductility under dynamic tension in the CrMnFeCoNi HEA. The dislocations will be decomposed into partial dislocations when they move across the twin boundary. The absorption of these partial dislocations into the twin boundary will induce the migration of twin boundary and the formation of dislocation step. This process can effectively release stress concentration. Thus, the twin boundary has the capacity to accommodate considerable plasticity. Consequently, sufficiently thin and dense twin lamellas take positive effect on the dynamic ductility. The ultimate strain of the CrMnFeCoNi HEA under dynamic tensile loading increased by 68% to 57%, in comparison with that under quasi-static tension (34%). As has been recorded *in situ* by high-speed photography (Fig. 20a), a uniform deformation occurred prior to the strain reaching 25% (approximately 0–90 μs). Afterwards, a strain concentration appeared in the middle of the specimens within the strain range of 25%−46% (approximately 90–130 μs). Eventually, the specimen shrank until fracture occurred, revealing excellent deformation uniformity and deformation localization. In addition, the constitutive model showed that the twins were strongly resistive to dislocation motion and provided 27% of work hardening, as displayed in Fig. 20b.

The deformation mechanism of the $Cr_{26}Mn_{20}Fe_{20}Co_{20}Ni_{14}$ HEA was dominated by dislocation slip at 1,000 s^{-1}, thereafter transferred to SFs at 2,000 s^{-1} and twinning at 3,000 s^{-1} [109]. The manifold interactions between dislocations and SFs, SFs and SFs (i.e., the Lomer-Cottrell locks), and SFs and twins contributed to the sustained hardening ability. The yield strength and the ultimate strength at 3,000 s^{-1} were 360 MPa and 1,420 MPa, respectively. Under the effect of SFs and twinning, the $Cr_{26}Mn_{20}Fe_{20}Co_{20}Ni_{14}$ HEA demonstrated uniform plastic deformation without any adiabatic shear bands at 35.8% strain and 3,000 s^{-1}, indicating decent resistance to thermal softening and adiabatic shear localization.

(b) Dynamic Hall-Petch effect

In the $Cr_{22}Mn_{14}Fe_{22}Co_{22}Ni_{20}$ HEA reported by Yang et al. [105], the newly formed deformation twins during dynamic deformation could divide the original annealing twins and the strip substructure in the matrix into ultra-fine closed blocks. This continuous segmentation caused dynamic grain refinement during the dynamic deformation process, leading to large dynamic strain hardening capacity, as shown in Fig. 21. The strain hardening rate remained stable at ~7 GPa to 30% strain when the $Cr_{22}Mn_{14}Fe_{22}Co_{22}Ni_{20}$ HEA deformed at a strain rate of $\sim 9 \times 10^3\ s^{-1}$ at 123 K. During the high-strain-rate (7,000 s^{-1}) deformation of $Cr_{26}Fe_{27}Co_{24}Ni_{23}$ HEA with annealing nanotwins, profuse ultra-fine single-variant deformation nanotwins of 1–2 nm thickness divide strip-like annealing nanotwins of 10–30 nm thickness into nano-blocks. The dynamic deformation-induced hierarchical structures, which are composed of

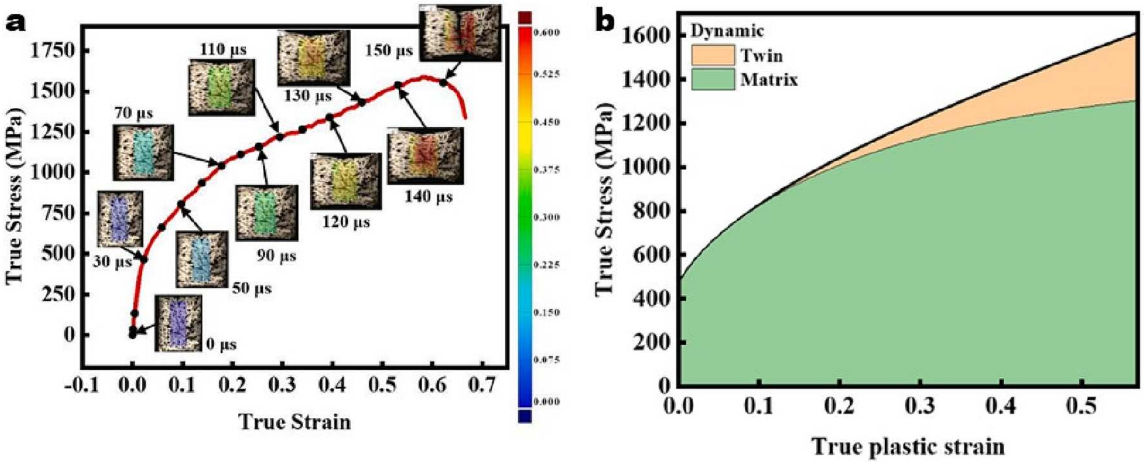

Fig. 20. (a) High-speed photographs correlated with a stress–strain curve of the CrMnFeCoNi HEA under dynamic tension. (b) Area graphs of the proportion of the matrix and twins in the flow stress of the dynamic tensile specimens [84].

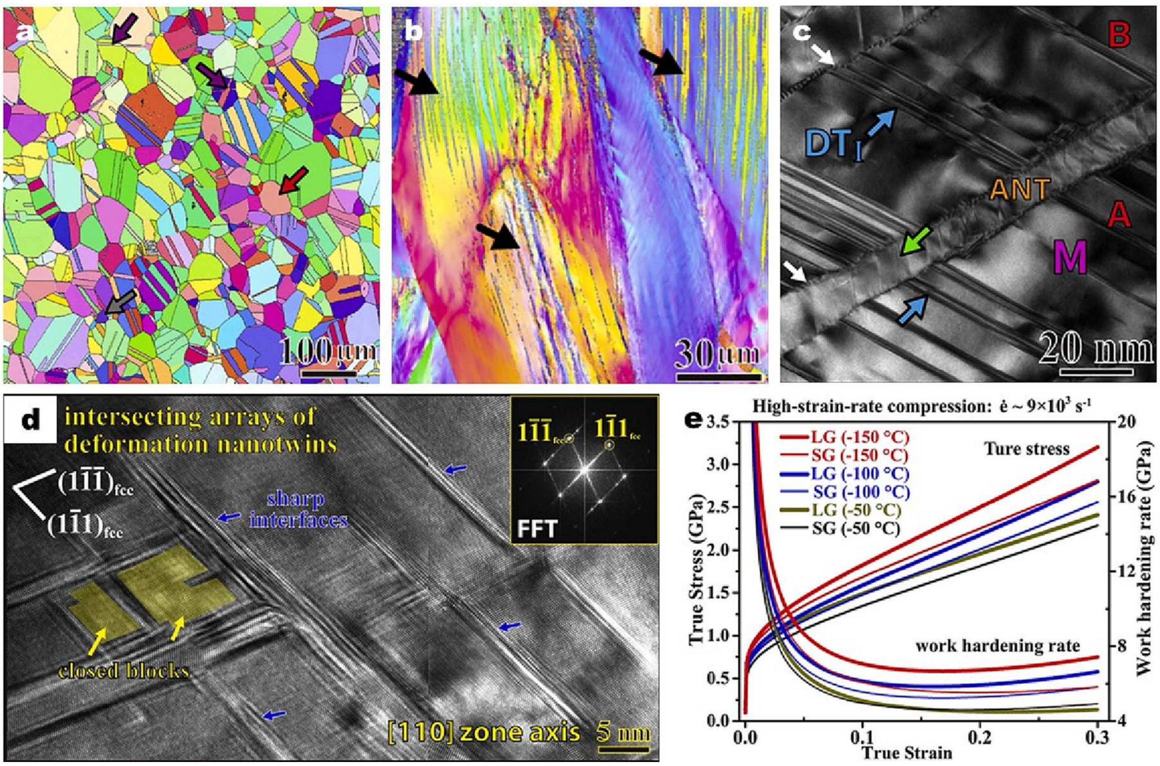

Fig. 21. IPF maps of (a) as-annealed and (b) dynamically-deformed $Cr_{22}Mn_{14}Fe_{22}Co_{22}Ni_{20}$. (c) and (d) TEM images of dynamically-deformed $Fe_{22}Co_{22}Ni_{20}Cr_{22}Mn_{14}$. (e) True stress–strain curves and work-hardening rates at a strain rate of ~9,000 s^{-1} [105].LG and SG represent the large-grain and small-grain samples.

micrometer, nanometer and sub-nanometer twins, provide a higher work-hardening capacity and profoundly improve the dynamic strength to ~1,500 MPa.

Similarly, the $V_{10}Cr_{10}Fe_{45}Co_{35}$ alloy exhibited a high strain-hardening rate and a dynamic compressive strength of ~1.9 GPa due to twinning under dynamic loads, which triggered the dynamic Hall-Petch effect [104]. The MnFeCoNiCu HEA possessed a high strain-hardening rate (~1,600 MPa) under dynamic condition (3,000 s^{-1}) since a large number of deformation twins come into being, resulting in grain fragmentation and weakening of the ⟨1 0 1⟩ compression texture [106]. In another research reported by Yuan et al. [227], plenty of deformation twins formed in the CrCoNi alloy during dynamic deformation owing to its low SFE, as shown in Fig. 22b. The strong interaction between dislocations and multiple twins (see Fig. 22c) could trigger more efficient grain refinement rather than

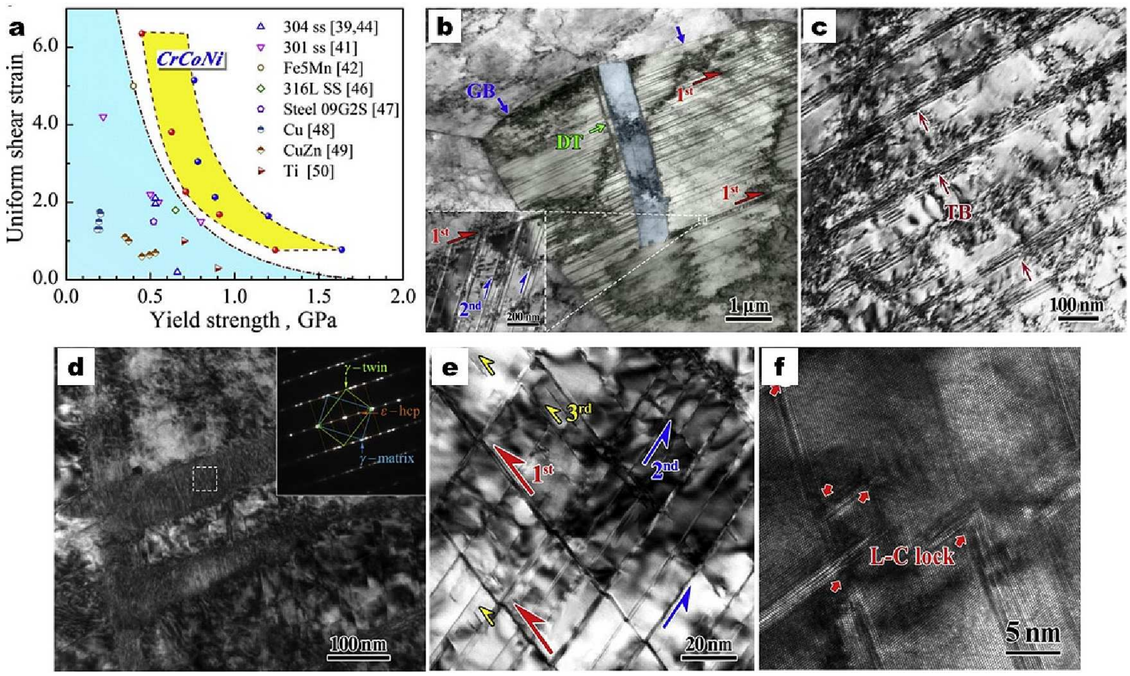

Fig. 22. Uniform dynamic shear strain vs. dynamic shear yield strength for the CrCoNi HEA and other metals as well as alloys. TEM images of the specimen deformed at room temperature showing (b) deformation twins (DTs) and (c) accumulation of high-density dislocations at twin boundaries (TBs). TEM images of the specimen deformed at cryogenic temperature showing (d) high density of stacking faults and phase transformation, (e) multiple DTs and (f) Lomer-Cottrell (L-C) lock [227].

dislocation cells. These newly formed interfaces, such as twin boundaries and grain boundaries, hindered the movement of dislocations. At cryogenic temperatures, more complex structures, including multiple twins, high-density stacking faults, Lomer-Cottrell locks, and phase transformation appeared in the dynamically-deformed CrCoNi alloy, as displayed in Fig. 22d−22f. The multiple twinning networks created obstacles for dislocation motion and provided paths for dislocation slip and cross slip. The Lomer-Cottrell locks and phase boundaries introduced by phase transformation would hinder the movement of dislocations. Under the influence of the above factors, the CrCoNi alloy exhibited better dynamic shear resistance at both room and cryogenic temperatures compared with conventional alloys (Fig. 22a). The uniform dynamic shear strains of the CrCoNi alloy at 298 K and 77 K are >6 and 5 while those of conventional alloys and metals are almost less than 2.

(c) Low deformation-twinning threshold strain

The high instantaneous stress provided by the dynamic loads, the high flow stress of high-density dislocations and the low activation energy of partial dislocations in the complex energy environment of chemical disorder usually promote deformation twinning in HEAs [82].

The critical applied stress for activating twinning partial dislocations could be roughly calculated by considering the SFE, as displayed in Eq. (41). Correspondingly, the theoretical twinning stress for the CrMnFeCoNi [84] and $Al_{0.1}$CrFeCoNi [71] HEAs should be 722 MPa and 636 MPa, respectively. Both of these values were higher than the ultimate flow stress before the quasi-static tensile fracture. However, under the dynamic tensile loading, the true flow stresses exceeded the critical applied stress at the true strains of ~20% and ~30%, respectively. The true strain and the true stress for twinning initiation in the CrMnFeCoNi HEA at 10^{-4} s^{-1} was ~20.5% and ~760 MPa (see blue arrows in Fig. 23a), respectively, whereas that at 4,700 s^{-1} was only ~6.2%~885 MPa (see red arrows in Fig. 23b), according to the investigation conducted by Kim et al. [78]. Moreover, Dai et al. [84] pointed out that the critical strain for twin nucleation was 12% under quasi-static loading for the CrMnFeCoNi HEA. A higher dislocation density induced by dynamic loads will promote the critical strain of the twinning to be 8% in the dynamic tensile specimen. Furthermore, there was a higher twin growth efficiency toward twin nucleation and multiplication during dynamic deformation, whereas the twin evolution rate in the quasi-static tensile specimen is limited. As a result, the twin volume fraction of the final dynamic tensile specimens is 6.1 times higher than that of the quasi-static tensile specimens. Further studies by Lu et al. [44] demonstrated that the stress threshold for twinning in the CrMnFeCoNi HEA was the same as the yield strength under dynamic loads. Under the effect of low threshold for twinning, the deformation mode of the CrMnFeCoNi HEA changed from dislocation slip under quasi-static load to dynamic twinning at high strain rate. The appearance of nano-twins also endowed it with a higher ultimate tensile strength and elongation (745 MPa and ~63% at 2,200 s^{-1}). When the strain rate increased to 9,000 s^{-1}, kinked twins and intersected twins formed in the CrMnFeCoNi HEA [81].

Taheri et al. [82] stated that the change of deformation mechanisms in the CrMnFeCoNi HEA with the strain rate can be attributed to its unique chemical disorder structure. Although twin nucleation requires strong local stress generated by dislocation density, the

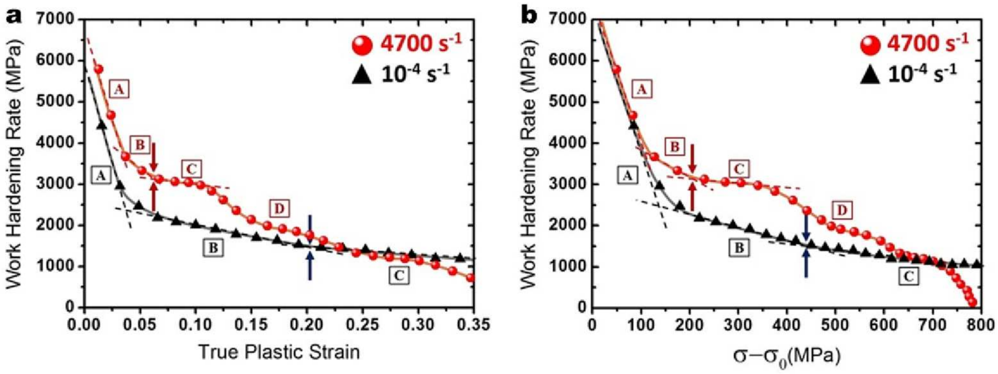

Fig. 23. (a) Work hardening rate ($d\sigma/d\varepsilon$) of the CrMnFeCoNi HEA as a function of true plastic strain and (b) normalized flow stress (σ-σ_0) at a strain rate of 10^{-4} s^{-1} and 4,700 s^{-1} [78].

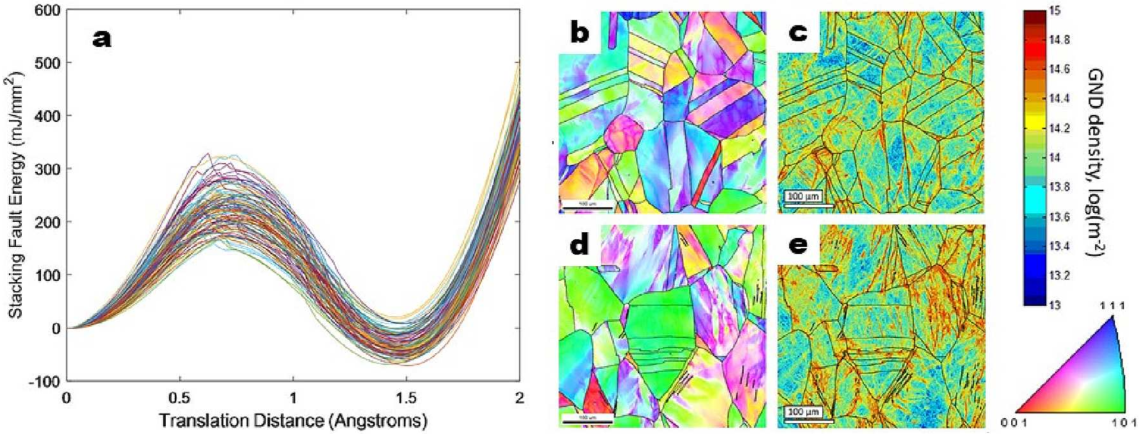

Fig. 24. (a) Relaxed generalized stacking fault energy curves at 0 K for 100 individual areas on a stacking fault plane in the CrMnFeCoNi HEA. IPF and local GND density maps for the (b) and (c)quasi-static, (d) and (e) 5000 s^{-1} conditions [82].

activation energy of partial dislocations in the complex energy environment (Fig. 24a) induced by chemical disorder is lower than that of full dislocations. Therefore, the deformation of the CrMnFeCoNi HEA under dynamic loads is dominated by partial dislocations, which is conducive to the change of plastic deformation mode from dislocation slip under quasi-static condition (Fig. 24b and 24c) to dynamic twinning at high stain rate (Fig. 24d and 24e).

3.3.2. Phase transformation under dynamic loads

Under a certain stress, some metastable structure in materials will transform into a more stable structure, such as the martensitic transformation in an austenitic stainless steels. In general, the stress-induced phase transformation can enhance the strength of a local region, and promote the dislocations to move to adjacent undeformed area, facilitating homogeneous deformation and giving rise to an increment in strain hardening and thereafter ductility. In 2016, Li et al. [25] proposed the TRIP effect in metastable HEAs for the first time. It is reported that the metastable $Fe_{50}Mn_{30}Co_{10}Cr_{10}$ HEA will undergo phase transformation from a soft phase (FCC phase) to a hard phase (close-packed hexagonal phase, HCP) during the loading process. The TRIP effect can reinforce the plasticity and strength of this alloy simultaneously. Lu et al. [228] introduced the TRIP effect into brittle BCC-RHEAs, whose elongation were generally smaller than 15% [101,228,229,230] for ductilization. In metastable dual-phased $TiZrHfTa_{0.4}$-$TiZrHfTa_{0.6}$ HEAs, the phase transformation from the BCC to HCP structure can release the internal stress and then further improves ductility. Thus, the elongation of the $HfZrTiTa_{0.4}$ HEAs could achieve 27%, greatly surpassing the results in previous reports.

The similarity between stress-induced phase transformation behaviors in HEAs under dynamic loads and that under quasi-static load can be comprehended from two aspects.

(a) Phase transformation and TRIP effect in HEAs can be influenced by dynamic loads

On the one hand, the dynamic loads could induce phase transformation. The martensitic phase transformation from FCC structure to BCC structure would occur inside the FCC grains of a metastable $V_{10}Cr_{10}Fe_{45}Co_{35}$ HEA during dynamic compression at room and low temperatures [104]. The slip system of the BCC martensite is fewer than that of the FCC phase. Thus, the alloy has a high strain-hardening rate at high strain rates. According to the density functional calculation results provided by Sohn et al. [103], the

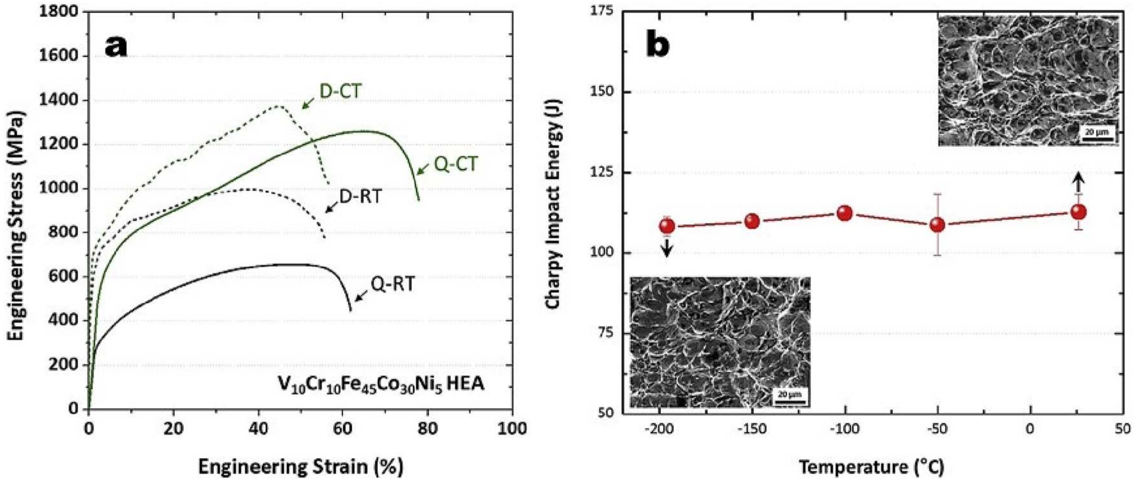

Fig. 25. (a) Quasi-static and dynamic engineering stress–strain curves tested at room and cryogenic temperatures and (b) Charpy-impact energy as a function of test temperature of the $V_{10}Cr_{10}Fe_{45}Co_{35}Ni_5$ HEA [103].

martensite transformation showed temperature dependency. The stability of the BCC martensite and intermediate HCP phase increased with decreasing temperature. Therefore, the metastable $V_{10}Cr_{10}Fe_{45}Co_{30}Ni_5$ HEA would undergo martensitic transformation from the FCC to BCC phase in the early stage of low-temperature dynamic tension. The TRIP effect improves the strength and the elongation at low temperature simultaneously. At 77 K, the tensile yield strength, the ultimate tensile strength and the elongation under a dynamic load (~1,550 s^{-1}) attained 650 MPa, 1,369 MPa, and 56.6% respectively (Fig. 25a). During low-temperature Charpy impact experiment, two-variant networks composed of a number of high-angle boundaries formed in the BCC martensite. These complex network structures refined the grains of the FCC parent phase and the BCC martensite, hindered dislocation motion, and effectively prevented the ductile–brittle transition. Therefore, the metastable $V_{10}Cr_{10}Fe_{45}Co_{30}Ni_5$ HEA maintained an impact toughness of 110 J at 77 K (Fig. 25b).

On the other hand, high strain rate caused a suppression of phase transformation in $Fe_{38-x}Mn_{30}Co_{15}Cr_{15}Ni_2Gd_x$ HEAs[115]. The addition of Gd element reduced the FCC phase stability, leading to the significant strain-induced FCC → HCP phase transformation during low strain-rate (10^{-3}-10^{-1} s^{-1}) deformation. However, with increasing strain rates, the phase transformation was gradually suppressed since the rate-induced shear bands inhibit the growth of the HCP phase. Upon dynamic strain rates (1,000–5,000 s^{-1}), the significant adiabatic temperature rise enhanced the phase stability, so the phase transformation was completely substituted by the deformation twinning. While the phase transformation and consequent HCP phase could postpone the increase of the dislocation density and compress the mean free path of dislocation to enhance strain-hardening rate, the effect of twinning is poor. The constantly reducing trend of strain hardening rate could be in the dynamic compressive true stress–strain curves of $Fe_{38-x}Mn_{30}Co_{15}Cr_{15}Ni_2Gd_x$ HEAs.

(b) Threshold of phase transformation under dynamic loads is related to strain rate

The threshold of phase transformation under dynamic loads is dependent on environment temperature and strain rate on the grounds that the stability of a lattice is dependent on the temperature, and the strain-rate effect normally results in an adiabatic temperature rise. In a metastable $V_{10}Cr_{10}Fe_{45}Co_{35}$ HEA [104], the adiabatic temperature rise during dynamic deformation was ~98 K. This adiabatic temperature rise enhanced the stability of the FCC structure, then inhibited the transformation from the FCC to BCC phase with increasing strain at high strain rate (see Fig. 26a and 26b). The result is, the stress difference under dynamic loads and

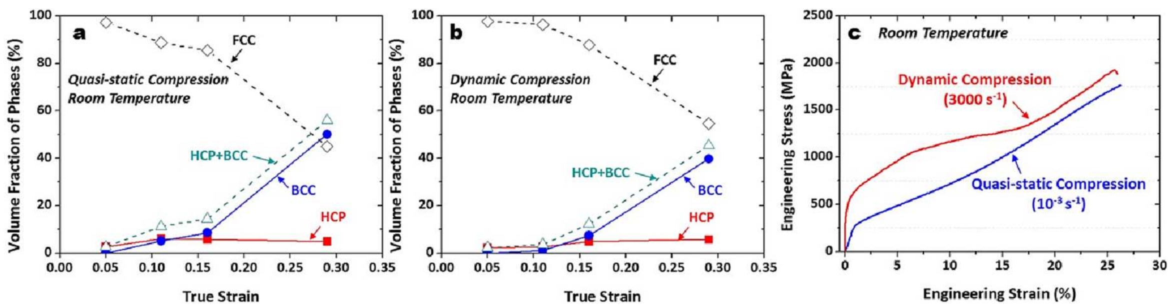

Fig. 26. Volume fractions of FCC, BCC, and HCP phases present in the (a) quasi-statically and (b) dynamically compressed specimens as a function of strain at room temperature in the $V_{10}Cr_{10}Fe_{45}Co_{35}$ HEA. (c) Quasi-static and dynamic engineering stress–strain curves of the $V_{10}Cr_{10}Fe_{45}Co_{35}$ HEA [104].

quasi-static load decreased with increasing strain, as shown in Fig. 26c. When the strain was 5%, the disparity was nearly 500 MPa, however, when the strain was 25%, the disparity was only ~200 MPa.

3.3.3. Adiabatic-shear effect

Adiabatic shear is a typical local instability phenomenon in dynamically-deformed metals, especially refractory metals [231,232,233,234]. During the dynamic deformation process of metals and alloys, the plastic work and the resultant converted heat cannot be timely diffused. Thus, the dynamic deformation process can be approximately seen as an adiabatic process. The formation of ASBs is the typical characteristic of adiabatic shear effect. Severe shear deformation will introduce a large number of dislocations and stimulate grain refinement in ASBs. Theoretically, ASBs preferentially form in the regions suffering from highest shear stress and thus severest deformation, such as along 45° with the loading direction in bulk materials under one-dimensional axial loading. Moreover, the heat converted from plastic deformation can cause melting and recrystallization. As a consequence, amorphous or nanocrystalline phases usually exist within ASBs [235,236,237].

The adiabatic shear effect in HEAs under dynamic loads has the following characteristics:

(a) Pronounced adiabatic temperature rise and adiabatic shear effect

Severe lattice distortion in HEAs will slow down the migration of phonons and electrons, thereby reducing the thermal conductivity. For example, the thermal conductivity of the TiZrNbTa alloy is only 14 $W \cdot m^{-1} \cdot K^{-1}$, which is much lower than its pure metal counterpart [238]. It means that the local temperature rise caused by the high-speed shear deformation can be retained for a long time, then resulting in a more prominent adiabatic shear effect. The study on the $(Al_{0.5}CrFeCoNi)_{0.95}Mo_{0.025}C_{0.025}$ HEA by Zhang et al. [66] proved that the thermal conductivity of HEAs played a decisive role in the formation of ASBs. The presence of Mo atoms would hinder thermal diffusion, reduce thermal conductivity, and advance the generation of ASBs. The width of ASBs in the W-$Al_{0.5}V_{0.2}Cr_{0.9}FeNi_{2.5}$ HEA [113] was ~12 μm, which is much smaller than that of ASB in conventional W-NiFe alloy prepared by liquid phase sintering (~200 μm) [239,240,241] under dynamic compression, indicative of high susceptibility to ASB in HEAs.

(b) More pronounced adiabatic-shear effect in BCC HEAs

On one hand, BCC-HEAs usually contain refractory metallic elements with low intrinsic thermal conductivity [238]. On the other hand, the dynamic deformation mechanism of BCC-HEAs is dominated by dislocation slips. There is no sufficient deformation and hardening mechanisms existing to compete with thermal effects in BCC HEAs. As present in the discovery of Song et al. [96], the strain-rate threshold for the formation of ASBs in BCC-TaNbHfZrTi was about 2,600 s^{-1} under dynamic compression (Fig. 28). This value is much lower than that of the FCC-structured CrMnFeCoNi HEA (4,700 s^{-1}) [78]. The calculated temperature in the ASBs of the W-$Al_{0.5}V_{0.2}Cr_{0.9}FeNi_{2.5}$ HEA was above 1,870 K, leading to the redissolution of precipitates into the matrix and the formation of vortex W and nanorod-like W (see Fig. 27b and 27c), as reported by Xue et al. [113].

(c) Balanced with strain hardening effect

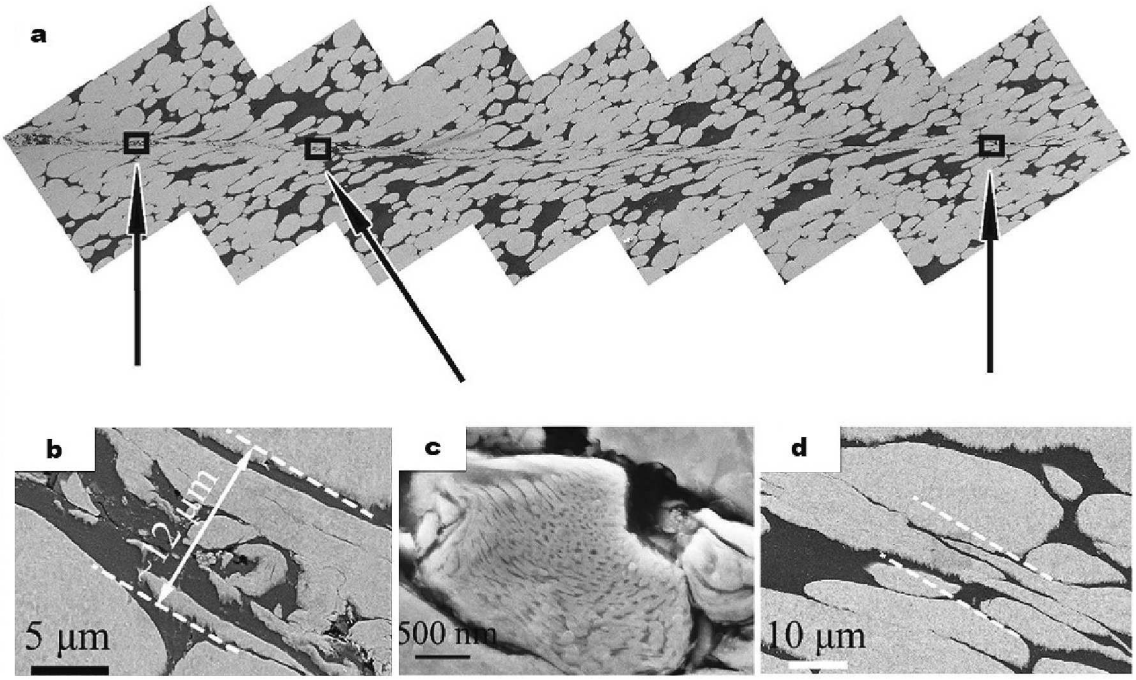

Fig. 27. SEM images of ASB in the W-$Al_{0.5}Cr_{0.9}FeNi_{2.5}V_{0.2}$ HEA: (a) Localized deformation of ASB, (b) typical microstructures of fragment W and vortex W, (c) nanorod-like W, and (d) elongated W [113].

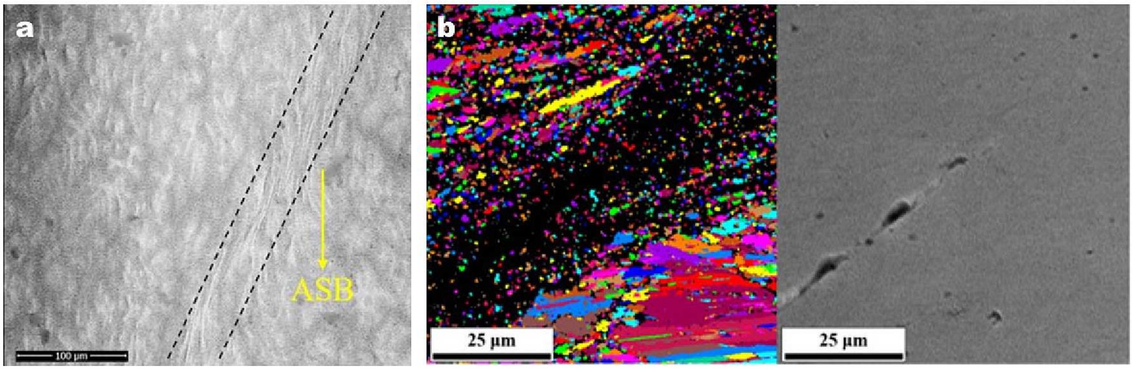

Fig. 28. (a) BSE images of the ASB in TaNbHfZrTi at the strain rate of 2,600 s^{-1}, showing elongated grains in the ASB marked by black dashed line [87]. (b) EBSD (left) and SEM (right) images of ASB in CrMnFeCoNi HEA at the strain rate of 4,700 s^{-1}, showing unique grain color maps indicating highly refined grains in the ASB [78].

He et al. [65] uncovered that small spherical drops and molten trace in the fracture surface resulting from adiabatic temperature rise could be observed in the AlCrFeCoNi HEA after dynamic fracture (Fig. 29a). It illustrated the presence of obvious thermal effect under dynamic compression. Due to the dynamic balance between the strain hardening and thermal softening during the dynamic deformation process, the strain hardening rate during dynamic deformation was higher than that during quasi-static deformation only in the elastic deformation stage (Fig. 29b). Moreover, the plastic deformation stage in the dynamic stress–strain curve of the AlCrFeCoNi alloy was relatively gentle, as presented in Fig. 29c and 29d.

According to Qiao et al., the competition between thermal softening and strain hardening weakens the work-hardening rate of BCC-HEAs such as $TiZrHfNbTaMo_x$ [107] and $AlTi_{0.5}Cr_{1.5}Fe_{1.5}CoNi$ [100] under dynamic loads compared with the situation under quasi-static loading. As stated by Dirras et al. [95], the deformation of the BCC-TiZrHfNbTa HEA was localized in the bands. At low strain rates (10 s^{-1}), the deformation bands were uniformly distributed in the whole alloy. As the strain rate increased, the dispersibility of the deformation bands as well as the density decreased, whereas the thickness increased. At high strain rates, the deformation was confined to ASBs containing a high level of localized strain, whereafter strong thermal softening effect occurred in the early stage of dynamic plastic deformation. Therefore, although the yield strength of the TiZrHfNbTa alloy at 3,400 s^{-1} was 1,450 MPa and the fracture strain was as high as 49%, the flow stress continued to decrease after yielding (Fig. 30a) and it fractured by means of adiabatic shear in the later stage of deformation (Fig. 30b).

As has been revealed by Chen et al. [111], the low thermal conductivity and resultant low adiabatic shear dissipation energy of the TiZrNbV HEA caused apparent adiabatic shearing during dynamic deformation. Consequently, the TiZrNbV HEA exhibited clear elastoplastic mechanical characteristics under quasi-static compression loading, while embrittlement and brittle fracture behavior emerged under dynamic condition. Moreover, the stress would decrease sharply at a certain point, namely stress collapse, due to the formation of ASBs. They conducted a finite element simulation analysis of the TiZrNbV HEA and the experimental steel bars, using the Johnson-Cook constitutive model without considering the adiabatic shear effect. The stress-time curves acquired from the finite element simulation agreed well with the experimental results for the elastic deformation phase, but did not show rapid decline after "stress collapse" as observed in the experiment due to the neglect of adiabatic shear softening. In addition, the experimental X-strain (i.e., the strain in the X direction) was larger than the simulation results, further revealing that the adiabatic shear softening played a significant role in the dynamic deformation of the TiZrNbV HEA.

(d) Affected by additional phase and heterostructure

For the eutectic $Al_{0.7}CrFeCoNi$ HEA with $L1_2$ precipitations [68], although the existence of precipitation would not delay the strain rate/deformation velocity threshold (11.26 m/s) as well as shear-strain threshold (~0.7) for the formation of ASBs and not reduce the width of ASBs (~4 mm), the width of the severely-deformed zone near the ASBs was reduced by 75%. This is because the high-strength precipitates can relieve the localization of deformation during dynamic deformation process. By comparing $Fe_{50}Mn_{30}Co_{10}Cr_{10}$ HEAs prepared by different processes, Yang et al. [91] pointed out that cold-rolled and annealed (CRQ) alloys with finer grains and higher-content HCP phase exhibited stronger strain hardening and strain-rate strengthening effects. Thus, the CRQ $Fe_{50}Mn_{30}Co_{10}Cr_{10}$ HEAs possessed low adiabatic shear susceptibility and stronger local deformation resistance at high strain rate. At 1.37×10^5 s^{-1}, no tendency of adiabatic shearing localization near the hat port was found in CRQ sample (Fig. 31a) while adiabatic shearing localization appeared near the hat port of the hot-rolled and annealed (HRQ) samples (Fig. 15b). Moreover, according to the parameters characterizing adiabatic shear susceptibility, the CRQ variant exhibited narrower ASBs, longer stress collapse time, larger critical strain and larger ASB formation energy, compared with the HRQ alloys. As shown in Fig. 15c and 15d, the stress collapse time and the critical strain for the CRQ alloy are 14.5 μs and 58%, respectively, whereas those of the HRQ alloy are 14.9 μs and 61%, respectively.

An observation carried out by Song et al. [93] indicated that a large quantity of fine lamellar and irregularly-shaped microstructures could effectively inhibit shear localization through twisting and bending during dynamic deformation. Hence, ASBs only formed at 3,200 s^{-1} in the eutectic $AlCrFeCoNi_{2.1}$ HEA with finer microstructure, yet the coarse microstructure displayed shear fracture under a quasi-static load. In the W-$Al_{0.5}V_{0.2}Cr_{0.9}FeNi_{2.5}$ HEA [113], the susceptibility to ASBs is enhanced due to the

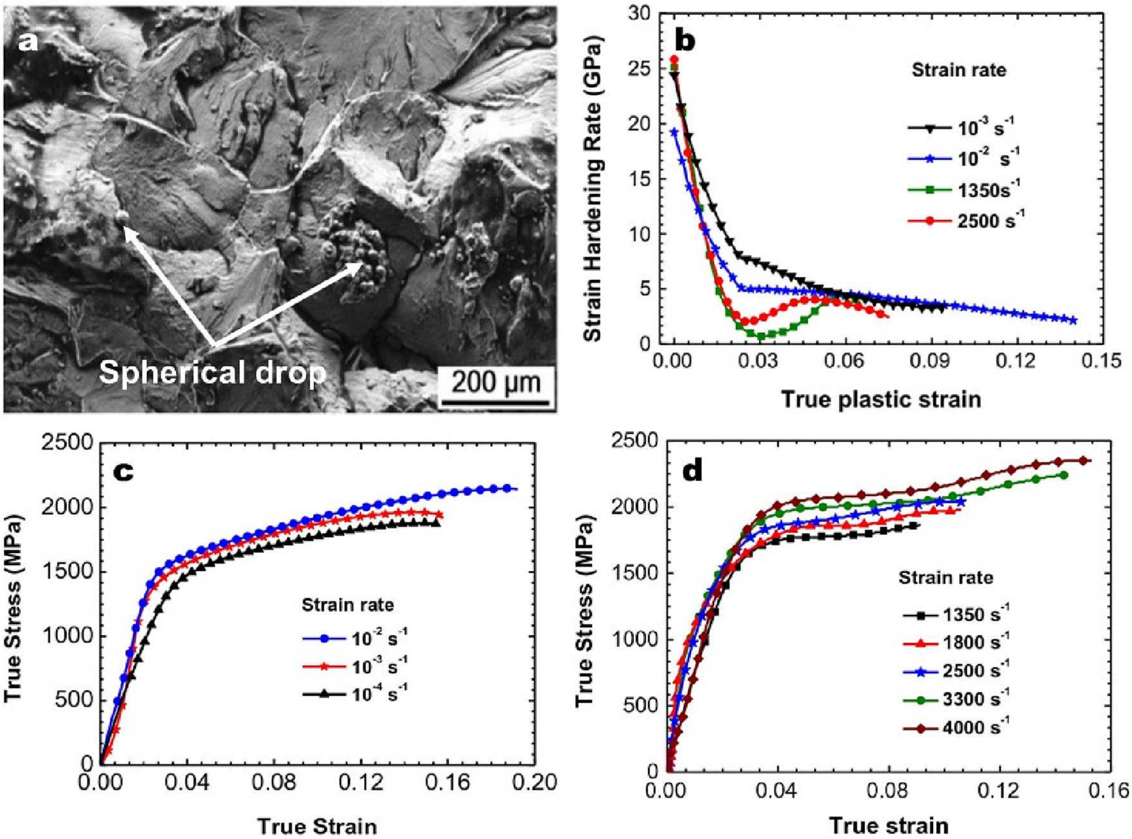

Fig. 29. (a) Fracture surface of the AlCrFeCoNi HEA after compression testing under 2,500 s^{-1}. (b) The variation of strain-hardening rate with the true plastic strain for the AlCrFeCoNi HEA. The true stress–strain curves of the AlCrFeCoNi HEA under (c) quasi-static and (d) dynamic deformation [65].

dissolvement of $L1_2$ precipitations into the matrix at a high temperature inside the ASBs, which led to further softening during shear localization. Therefore, despite that this alloy showed a ductility of >30% in its stress–strain curve, cracks indeed appeared owing to shear localization after dynamic compression tests.

Since the appearance of secondary phase will lead to disparity during the plastic deformation and the thermal conductivity of various regions, dislocations are easy to accumulate and heat is difficult to conduct around the boundaries. For example, when the WFeNiMo HEA [46] with BCC + FCC + μ-phase microstructure was applied upon a high strain-rate loading, multiple slips and high-density dislocation entanglement appeared in the BCC solid solution, and twinning occurred in the FCC solid solution, with dislocations accumulated at the interface between high-strength μ-phase precipitations and FCC solid solution. Due to the heterogeneous

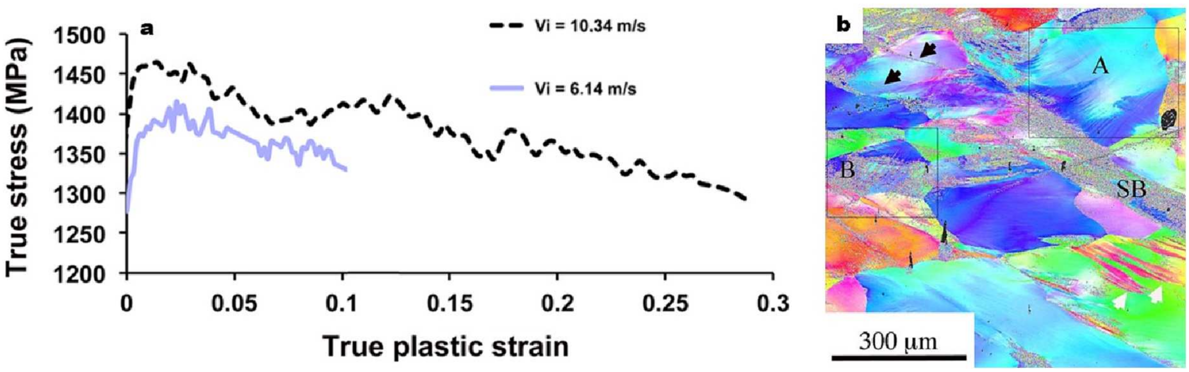

Fig. 30. (a) The true stress versus true plastic strain plots for strain rates in the dynamic regions of the TiZrHfNbTa HEA. (b) IPF map illustrating the localized deformation around a shear band (SB) in the sample impacted up to a true strain of ~0.49 at a velocity of 10.34 m s^{-1}, namely 4700 s^{-1}. SB interacts with the needle-like features in the area marked by A. Very thin SBs within the grains exist in the area marked by B [95].

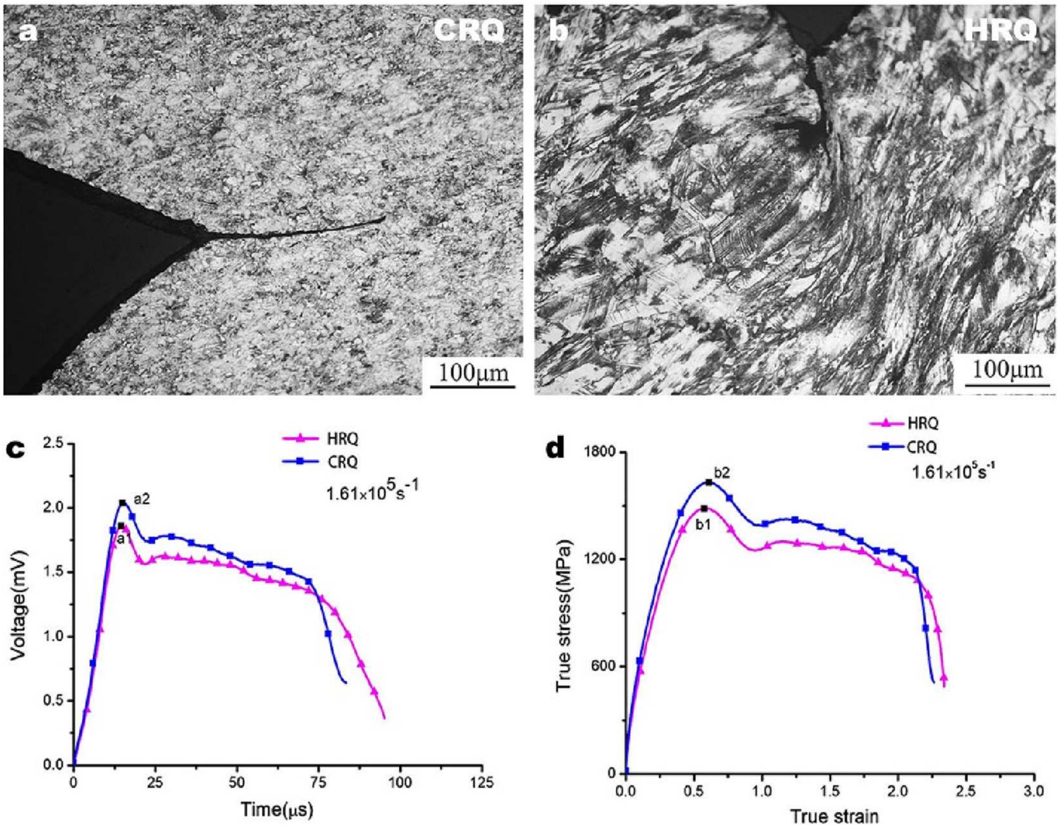

Fig. 31. The characteristics of (a) CRQ and (b) HRQ $Fe_{50}Mn_{30}Co_{10}Cr_{10}$ HEAs under the loading strain rate of 1.37×10^5 s^{-1}. The (c) voltage–time loading curves and (d) true stress–true strain curves of both samples under the loading strain rate of 1.61×10^5 s^{-1} [91].

deformation of different regions, a large strain gradient and dynamic recrystallization were induced by high-density dislocations that accumulated in the region with heterogeneous deformation. Thus, shear bands would be generated at the interfaces due to the instantaneous decrease in stress caused by dynamic recrystallization, as shown in Fig. 32. A similar phenomenon was observed in the case of the $TiZrHfTa_{0.53}$ HEA [47] with BCC + HCP dual-phase structure. Thermoplastic instability under dynamic loads was responsible for adiabatic shear failure. A large number of ASBs initiating along the phase boundaries inhibited the dynamic plastic deformation, giving rise to a fracture strain of only 12.1% at 2,100 s^{-1}.

It has been reported by Liao et al. that inhomogeneous composition elemental distributions, i.e., elemental segregation, in the CrMnFeCoNi HEA could effectively hinder the propagation of ASBs and therefore improve the dynamic toughness [83]. The concentration fluctuation of Mn and Ni, which were enriched in interdendritic boundaries initially, was enhanced during dynamic deformation. The Ni enrichment led to increased local SFE, thereafter local softening. The alternating soft and hard regions resisted the propagation of ASBs, because extra energy was needed for ASBs to pass through hard regions from soft regions. As a result, the ASB became narrower after passing through the intersection between shear-flow elemental segregation regions (see Fig. 33).

It should be noted that the formation and development of ASBs are influenced by additional phase and heterostructure. Adiabatic shear instead of microstructural features will ultimately dominate dynamic failure with increasing strain rates. An example is given by the interfacial decohesion at the B2 and FCC interfaces in eutectic $AlCrFeCoNi_{2.1}$ HEA that led to failure when the alloy was impacted with projectile at a velocity of 803 m/s. At velocities higher than 1,100 m/s, failure occurred in the regions containing ASBs [92].

4. Potential applications of HEAs under dynamic loads

So far, several potential applications based on the dynamic-mechanical behaviors of HEAs have been explored:

5. (a) Bulletproof armor

FCC-HEAs possessing high strain hardening under dynamic condition display promising impact protection ability. Both $Al_{0.1}$CrFeCoNi [67] and $AlCrFeCoNi_{2.1}$ [92] HEAs failed by ductile-hole growth, which is a common failure mode for ductile materials under ballistic impact, showing great potential for impact protection applications. For the $Al_{0.1}$CrFeCoNi HEA with an FCC structure that was impacted by spherical E52100 steel projectiles, microbanding and microtwinning dominated the deformation at a projectile velocity of

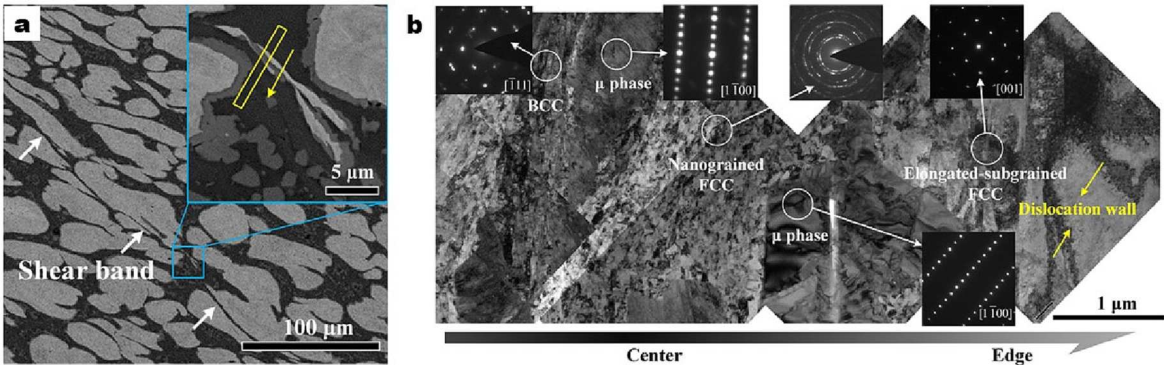

Fig. 32. (a) SEM images of regions near the fracture surface of WFeNiMo remnant showing shear bands formation in the main body. The insets mark the regions for TEM observation. (b) Bright-field TEM image of the shear band in yellow rectangles in the inset of Fig. 32a from the center to its edge [46].

594 m/s [67]. The generation of ASBs, recrystallized fine grains and crack initiation and growth were triggered when the projectile velocity was increased. A high hardness value of highly deformed areas and narrow zones around ASBs indicates remarkable work hardening during penetration. When the FCC + B2 eutectic $AlCrFeCoNi_{2.1}$ HEA was impacted by the spherical tungsten-carbide projectiles, it was partially and fully penetrated at 803 m/s and 1,159 m/s, respectively [92]. When the projectile velocity reached 1,388 m/s, full penetration appeared. Yang et al. [122] investigated the microstructure evolution of the $Cr_{26}Fe_{27}Co_{24}Ni_{23}$ HEA impacted by semi-armor-piercing projectiles with a velocity of ~840 m/s. Results showed that there was just dislocation accumulation at the boundaries between lamellar annealing nanotwins and recrystallized grains in the non-deformation region (Fig. 34d). In the intermediate deformation region and the heavy deformation region close to the bullet hole, block-structures composed of boundaries of annealing/deformation nanotwins formed (Fig. 34a and 34b).

(b) High-speed damage

Although microstructure features hardly affect the dynamic-mechanical behaviors of HEAs at high loading velocities, ASBs or shear bands along boundaries seem to be beneficial to the damage characteristics of alloys. For example, the FeNiMoW HEA displayed outstanding self-sharpening performance due to the ultra-strong μ-phase-stimulated dynamic recrystallization softening mediated shear banding (Fig. 35a) [46]. The volume of penetration channel of the FeNiMoW HEA increases by 18% compared with the tungsten heavy alloy under high kinetic energy per volume (25 kJ/cm^3), as shown in Fig. 35b. Under the effect of adiabatic shear, recrystallizations and twins, the CrFeCoNi HEA showed outstanding penetration performance [97]. Compared with those of the steel long rod projectiles, the penetration depth and the volume of crater of the CrFeCoNi HEA long rod projectiles increased by 43% and 78%, respectively. The $TiZrHfTa_{0.53}$ [47] and $TiZrHfTa_{0.7}W_{0.3}$ [115] HEAs with a BCC + HCP dual-phased microstructure and the TiZrNbV HEA [111] with single BCC structure all exhibited energy-release characteristics due to the rapid shearing fragmentation and the oxidation of active metals (Fig. 36).

6. Prospects

Despite of the above-mentioned achievements, the studies focused on the dynamic-mechanical behaviors of HEAs are still few and lacking. In this final section, several future trends and prospects of HEAs are proposed based on the existing literature as follows:

(a) The establishment of a dynamic-mechanical model for HEAs is important and necessary. So far, the research regarding the dynamic-mechanical models of HEAs have mainly been based on numerical simulation combining experimental results and classical models. It is expected that the unique composition and structure may not only bring about some new parameters, but also engender new physical models that can better predict the dynamic-mechanical behaviors of existing and/or yet-to-be-discovered novel HEA systems. In our opinion, due to the mixture of multiple equal or nearly equal elements and consequently the high configurational entropy, HEA will exhibit a single solid solution matrix with the highly chemical complexity and serious lattice distortion. Moreover, dense and various ordered microstructures with different scales generally coexist. Thus, various deformation mechanisms can be easily activated and work together under dynamic load. It may be a potent and key point for the establishment of a dynamic-mechanical model for HEAs.

(b) The *in situ* observation of microstructure during the dynamic deformation of HEAs need more effort. To date, the observation of microstructure evolution of HEAs during dynamic loads has been *ex situ*. Although the analysis on the HEAs with different strains can obtain some useful information on the microstructure evolution during dynamic deformation, some pseudo phenomenon may be found due to the interference from the equipment for controlling deformation degree and the disappearance of thermal effect. In order to exactly establish an in-depth comprehension on the complex microstructure evolution of HEAs and further the deformation mechanism, especially the multiple deformation mechanisms during dynamic deformation, the *in situ* observation of microstructures is necessary.

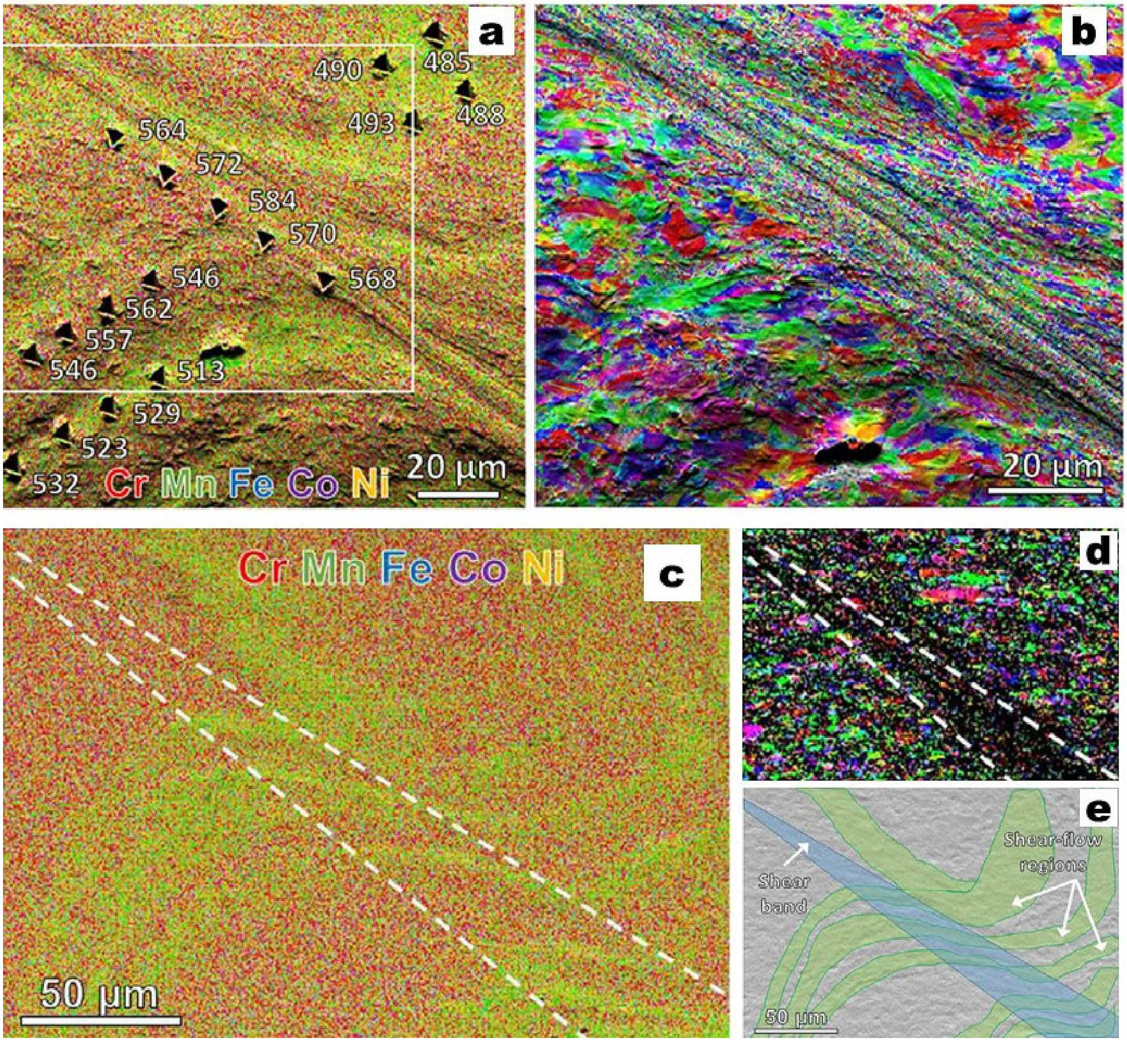

Fig. 33. (a) Nanoindentation points with their Vickers hardness values in Hv and (b) fore-scattered detector image overlapped with its corresponding EBSD inverse pole figure (IPF)-Z image of the area marked with the white rectangle in (a) of CrMnFeCoNi HEA deformed at a strain rate of ~15,000 s^{-1} with a strain of ~0.62. (c) Elemental distribution maps, (d) an EBSD IPFZ map and (e) a schematic in the sample, showing an ASB stopped in the area with elemental segregation [83].

(c) The effect of multi-field coupling is worth systematic intensive study. Up to now, most of the researches on the dynamic-mechanical behaviors of HEAs have been carried out at room temperature. The dynamic-mechanical behaviors of HEAs at extreme conditions, such as high temperature, low temperature and strong corrosion, are supposed to be different. The effect of multi-field coupling should be more concerned and surveyed. As far as we are concerned, the mechanical behavior under high strain rate is similar with that at cryogenic environment. For example, both the strength and ductility raise as the strain rate increases or environment temperature decreases. Thus, the dynamic-mechanical behaviors of HEAs at cryogenic environment is worth expecting.

(d) More researches concerning the applications of HEAs under dynamic loads are desirable. Flexibility in composition and structure design of HEAs can bring in the outstanding dynamic properties as well as other additional performance. Excellent comprehensive performance is very important for modern devices, which are often multifunctional. Valuable application prospects will promote more valuable researches.

7. Conclusion

A great deal of progress has been made on the dynamic-mechanical behaviors of HEAs during the past 8 years. The members in this material family have been expanded to 61 alloy systems, and more novel members are still awaiting to be discovered in the future. These materials have been characterized in a wide range of evaluations including the mechanical tests at different strain rates by

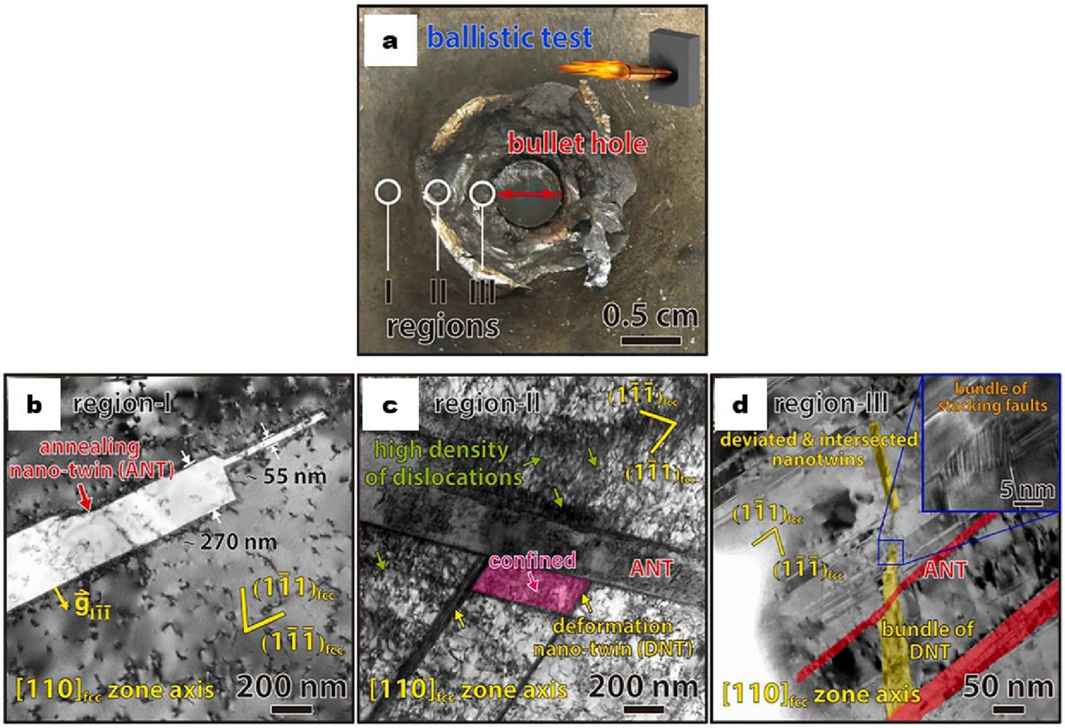

Fig. 34. (a) The ballistic Mn-free $Fe_{27}Co_{24}Ni_{23}Cr_{26}$ HEA plate and the microstructural examination regions, i.e. regions I, II and III, nearby the bullet hole. TEM images of regions (b) I, (c) II and (d) III [122].

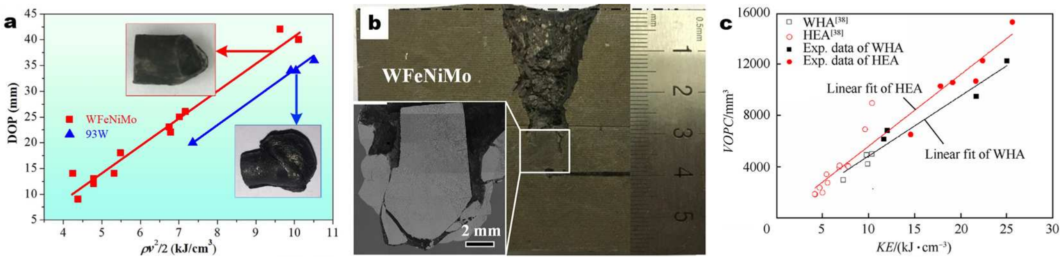

Fig. 35. (a) Penetration depth of a FeNiMoW rod and 93 W rod versus kinetic energy per volume, with photographs of the retrieved remnants, longitudinal sections of medium carbon steel targets impacted by (b) a FeNiMoW penetrator, with SEM micrographs of the remnant in the corresponding insets, respectively [46]. (c) Experiment results of kinetic energy per volume ($1/2\rho v^2$) - volume of penetration channel [97].

different methods as well as the microstructure observation at different scales. While some special dynamic deformation mechanisms of HEAs were revealed and analyzed based on the evolution of microstructures, some classic dynamic-mechanical models were revised accordingly. More importantly, many of the alloys showed unique and probably useful dynamic-mechanical properties, spurring continued research and exploration of possible applications.

In short, the dynamic-mechanical behaviors, especially the dynamic deformation mechanisms, of HEAs include the following characteristics:

(a) The dynamic deformation of HEAs is dominated by dislocation slips. Under the effects of dislocation thermal activation mechanism and phonon drag mechanism, HEAs show significant positive strain-rate effect and strain-rate sensitivity under dynamic loads. In addition, the rapidly proliferating dislocations caused by high strain load will produce a strong interaction, which can further strengthen the alloys. At the meantime, the entangled dislocations will affect the fracture mechanism of HEAs.

(b) The special microstructures in HEAs have an important impact on the dislocation motion upon dynamic loads and thus the dynamic-mechanical properties of the materials. Under dynamic loads, the strong lattice distortion caused by topological order and chemical disorder of HEAs can simultaneously improve strength and ductility. The short-range ordered microstructure greatly improves the yield strength of alloys by hindering dislocation movement at the atomic scale, showing high strain-rate

Fig. 36. High-speed video frames of the deflagration process of the $TiZrHfTa_{0.53}$ projectile at the speed of 857 m/s [47].

sensitivity and significant positive strain-rate effect. These reported HEAs still follow the Hall-Petch relationship under dynamic loads. Grain refinement effectively strengthens the alloys, while contributes a good ductility. For HEAs with multi-phases, the additional phase affects the dynamic-mechanical properties of alloys by affecting dislocation movement.

(c) Twinning plays an important role during the dynamic deformation of HEAs with low stacking fault energy, such as FCC-HEAs. During high strain-rate deformation, a large instantaneous stress provided by dynamic loads results in the high-density dislocations and the increasing flow stress. Then the critical stress for dislocations further slips and the resolved shear stress for twining increase, showing as an apparent low threshold strain of HEAs during dynamic deformation. As a result, the dynamic deformation of HEAs with low stacking fault energy could be coordinated by deformation twins. On one hand, deformation twinning generates a large number of twin boundaries. On the other hand, deformation twinning produces a "dynamic Hall-Petch effect" to further refine the microstructure. The formation of new interfaces will hinder the movement of dislocations. Therefore, HEAs with low stacking fault energy display high strain hardening under dynamic loads.

(d) The dynamic deformation of metastable HEAs is affected by strain induced transformation. The phase transformation under dynamic loads can effectively improve the strain hardening of the alloys, whereas the strain hardening will be restrained by the thermal effect caused by dynamic deformation. In addition, the phase transformation under dynamic loads has a certain grain-refining effect. Refining grains and grain boundaries can inhibit the ductile–brittle transition of the alloys as to ensure good impact toughness.

(e) The dynamic deformation of HEAs generally leads to adiabatic shear and other thermal effects. Due to the serious lattice distortion in HEAs, there exists obvious thermal effect during the dynamic deformation. The thermal-softening effect will weaken the strain hardening of HEAs. The adiabatic shear effect is more obvious in BCC-HEAs, as they are composed of elements with low thermal conductivity and the deformation mechanism is relatively single. Although additional phase can inhibit deformation localization to a certain extent, the difference of plastic deformation and thermal conductivity of each phase and the obstruction of interfaces to dislocation movement will promote the generation of adiabatic shear band.

(f) To reveal more deeply dynamic-mechanical behaviors of HEAs, the dynamic-mechanical model for HEAs and the platform for *in situ* observing the microstructure evolution during the dynamic deformation of HEAs should be established. The effect of multi-field coupling and the applications concerning with dynamic-mechanical behaviors of HEAs are also worth systematic intensive study.

Declaration of Competing Interest

The authors declare that they have no known competing financial interests or personal relationships that could have appeared to influence the work reported in this paper.

Data availability

No data was used for the research described in the article.

Acknowledgments

This work was supported by the National Natural Science Foundation of China (Grant Nos. 52171166, 11972372, 52271110 and U20A20231), the State Key Laboratory for Advanced Metals and Materials in the University of Science and Technology Beijing (No. 2020Z-08), the Funds for Creative Research Groups of China (No. 51921001). P. K. Liaw appreciates support from (1) the National Science Foundation (Grant Nos. DMR - 1611180, 1809640, and 2226508) and (2) the Army Research Office (W911NF-13-1-0438 and W911NF-19-2-0049).

References

[1] Zambrano OA. A general perspective of Fe-Mn-Al-C steels. J Mater Sci 2018;53:14003–62.
[2] Luo HW, Shen GH. Progress and perspective of ultra-high strength steels having high toughness. Acta Metall Sin 2020;56:494–512.
[3] Kilic N, Ekici B. Ballistic resistance of high hardness armor steels against 7.62 mm armor piercing ammunition. Mater Des 2013;44:35–48.

[4] Saleh M, Kariem MM, Luzin V, Toppler K, Li HJ, Ruan D. High strain rate deformation of ARMOX 500T and effects on texture development using neutron diffraction techniques and SHPB testing. Mater Sci Eng, A 2018;709:30–9.
[5] Behner T, Heine A, Wickert M. Dwell and penetration of tungsten heavy alloy long-rod penetrators impacting unconfined finite-thickness silicon carbide ceramic targets. Int J Impact Eng 2016;95:54–60.
[6] Cury R, Issartel F, Joubert JM, Couque H. Evolution of cobalt-free tungsten heavy alloys for kinetic energy penetrators. Powder Metall 2013;56:347–50.
[7] Luo RM, Huang DW, Yang MC, Tang EL, Wang M, He LP. Penetrating performance and "self-sharpening" behavior of fine-grained tungsten heavy alloy rod penetrators. Mater Sci Eng, A 2016;675:262–70.
[8] Fang XL, Liu JX, Wang X, Li SK, Guo WQ. Investigation on the penetration performance and "self-sharpening" behavior of the 80W–14Cu-6Zn penetrators. Int J Refract Met Hard Mater 2016;54:237–43.
[9] Zhu FL, Chen Y, Zhu GL. Numerical simulation study on penetration performance of depleted Uranium (DU) alloy fragments. Def Technol 2021;17:50–5.
[10] Bleise A, Danesi PR, Burkart W. Properties, use and health effects of depleted uranium (DU): a general overview. J Environ Radioact 2003;64:93–112.
[11] Wang B, Dong Y, Huang G. An investigation on the adiabatic shear bands in depleted U-0.75 wt % Ti alloy under dynamic loading. Metals 2018:8.
[12] Meyers MA. Dynamic behavior of materials. Ner York: John Wiley & Sons; 1994.
[13] Liang R, Khan AS. A critical review of experimental results and constitutive models for BCC and FCC metals over a wide range of strain rates and temperatures. Int J Plast 1999;15:963–80.
[14] Cantor B, Chang ITH, Knight P, Vincent AJB. Microstructural development in equiatomic multicomponent alloys. Mater Sci Eng, A 2004;375:213–28.
[15] Yeh JW, Chen SK, Lin SJ, Gan JY, Chin TS, Shun TT, et al. Nanostructured high-entropy alloys with multiple principal elements: Novel alloy design concepts and outcomes. Adv Eng Mater 2004;6:299–303.
[16] Zhang W, Liaw PK, Zhang Y. Science and technology in high-entropy alloys. Sci China Mater 2018;61:2–22.
[17] Chen H, Kauffmann A, Laube S, Choi IC, Schwaiger R, Huang Y, et al. Contribution of lattice distortion to solid solution strengthening in a series of refractory high entropy alloys. Metall Mater Trans A 2017;49:772–81.
[18] Yeh JW. Alloy design strategies and future trends in high-entropy alloys. JOM 2013;65:1759–71.
[19] Song H, Tian F, Hu Q-M, Vitos L, Wang Y, Shen J, et al. Local lattice distortion in high-entropy alloys. Phys Rev Mater 2017:1.
[20] Tong Y, Zhao S, Bei H, Egami T, Zhang Y, Zhang F. Severe local lattice distortion in Zr- and/or Hf-containing refractory multi-principal element alloys. Acta Mater 2020;183:172–81.
[21] Lei Z, Liu X, Wu Y, Wang H, Jiang S, Wang S, et al. Enhanced strength and ductility in a high-entropy alloy via ordered oxygen complexes. Nature 2018;563:546–50.
[22] Ding Q, Zhang Y, Chen X, Fu X, Chen D, Chen S, et al. Tuning element distribution, structure and properties by composition in high-entropy alloys. Nature 2019;574:223–7.
[23] Wu Y, Zhang F, Yuan X, Huang H, Wen X, Wang Y, et al. Short-range ordering and its effects on mechanical properties of high-entropy alloys. J Mater Sci Technol 2021;62:214–20.
[24] Dasari S, Jagetia A, Sharma A, Nartu MSKKY, Soni V, Gwalani B, et al. Tuning the degree of chemical ordering in the solid solution of a complex concentrated alloy and its impact on mechanical properties. Acta Mater 2021:212.
[25] Li Z, Pradeep KG, Deng Y, Raabe D, Tasan CC. Metastable high-entropy dual-phase alloys overcome the strength-ductility trade-off. Nature 2016;534:227–30.
[26] Lu Y, Dong Y, Guo S, Jiang L, Kang H, Wang T, et al. A promising new class of high-temperature alloys: eutectic high-entropy alloys. Sci Rep 2014;4:6200.
[27] Shi P, Li R, Li Y, Wen Y, Zhong Y, Ren W, et al. Hierarchical crack buffering triples ductility in eutectic herringbone high-entropy alloys. Science 2021;373:912–98.
[28] Pan Q, Zhang L, Feng R, Lu Q, An K, Chuang AC, et al. Gradient cell-structured high-entropy alloy with exceptional strength and ductility. Science 2021;374:984–99.
[29] Gludovatz B, Hohenwarter A, Catoor D, Chang EH, George EP, Ritchie RO. A fracture-resistant high-entropy alloy for cryogenic applications. Science 2014;345:1153–8.
[30] Yang T, Zhao YL, Tong Y, Jiao ZB, Wei J, Cai JX, et al. Multicomponent intermetallic nanoparticles and superb mechanical behaviors of complex alloys. Science 2018;362:933–97.
[31] Kumar NAPK, Li C, Leonard KJ, Bei H, Zinkle SJ. Microstructural stability and mechanical behavior of FeNiMnCr high entropy alloy under ion irradiation. Acta Mater 2016;113:230–44.
[32] El-Atwani O, Li N, Li M, Devaraj A, Baldwin JKS, Schneider MM, et al. Outstanding radiation resistance of tungsten-based high-entropy alloys. Sci Adv 2019;5:eaav2002.
[33] Zhang Y, Stocks GM, Jin K, Lu C, Bei H, Sales BC, et al. Influence of chemical disorder on energy dissipation and defect evolution in concentrated solid solution alloys. Nat Commun 2015;6:8736.
[34] Jin K, Lu C, Wang LM, Qu J, Weber WJ, Zhang Y, et al. Effects of compositional complexity on the ion-irradiation induced swelling and hardening in Ni-containing equiatomic alloys. Scripta Mater 2016;119:65–70.
[35] Chen YY, Duval T, Hung UD, Yeh JW, Shih HC. Microstructure and electrochemical properties of high entropy alloys - a comparison with type-304 stainless steel. Corros Sci 2005;47:2257–79.
[36] Luo H, Li ZM, Mingers AM, Raabe D. Corrosion behavior of an equiatomic CoCrFeMnNi high-entropy alloy compared with 304 stainless steel in sulfuric acid solution. Corros Sci 2018;134:131–219.
[37] Fu Y, Li J, Luo H, Du CW, Li XG. Recent advances on environmental corrosion behavior and mechanism of high-entropy alloys. J Mater Sci Technol 2021;80:217–33.
[38] Li L, Lu J, Liu X, Dong T, Zhao X, Yang F, et al. Al CoCrFeNi high entropy alloys with superior hot corrosion resistance to Na_2SO_4 + 25% NaCl at 900 °C. Corros Sci 2021;187.
[39] Jawaharram GS, Barr CM, Monterrosa AM, Hattar K, Averback RS, Dillon SJ. Irradiation induced creep in nanocrystalline high entropy alloys. Acta Mater 2020;182:68–76.
[40] Tsao TK, Yeh AC, Kuo CM, Kakehi K, Murakami H, Yeh JW, et al. The high temperature tensile and creep behaviors of high entropy superalloy. Sci Rep 2017;7:12658.
[41] Sun S, Gao P, Sun GX, Cai ZY, Hu JJ, Han S, et al. Nanostructuring as a route to achieve ultra-strong high- and medium-entropy alloys with high creep resistance. J Alloys Compd 2020;830.
[42] Kumar N, Ying Q, Nie X, Mishra RS, Tang Z, Liaw PK, et al. High strain-rate compressive deformation behavior of the $Al_{0.1}$CrFeCoNi high entropy alloy. Mater Des 2015;86:598–602.
[43] Zhang TW, Ma SG, Zhao D, Wu YC, Zhang Y, Wang ZH, et al. Simultaneous enhancement of strength and ductility in a NiCoCrFe high-entropy alloy upon dynamic tension: micromechanism and constitutive modeling. Int J Plast 2020;124:226–46.
[44] He J, Wang Q, Zhang H, Dai L, Mukai T, Wu Y, et al. Dynamic deformation behavior of a face-centered cubic FeCoNiCrMn high-entropy alloy. Sci Bull 2018;63:362–438.
[45] Shabani M, Indeck J, Hazeli K, Jablonski PD, Pataky GJ. Effect of strain rate on the tensile behavior of CoCrFeNi and CoCrFeMnNi high-entropy alloys. J Mater Eng Perform 2019;28:4348–56.
[46] Liu XF, Tian ZL, Zhang XF, Chen H-H, Liu T-W, Chen Y, et al. "Self-sharpening" tungsten high-entropy alloy. Acta Mater 2020;186:257–66.
[47] Zhang Z, Zhang H, Tang Y, La Zu, Ye Y, Li S, et al. Microstructure, mechanical properties and energetic characteristics of a novel high-entropy alloy $HfZrTiTa_{0.53}$. Mater Des 2017;133:435–43.
[48] Miracle DB, Senkov ON. A critical review of high entropy alloys and related concepts. Acta Mater 2017;122:448–511.
[49] George EP, Curtin WA, Tasan CC. High entropy alloys: a focused review of mechanical properties and deformation mechanisms. Acta Mater 2020;188:435–74.
[50] Sathiyamoorthi P, Kim HS. High-entropy alloys with heterogeneous microstructure: processing and mechanical properties. Prog Mater Sci 2022; 123.

[51] Li W, Xie D, Li D, Zhang Y, Gao Y, Liaw PK. Mechanical behavior of high-entropy alloys. Prog Mater Sci 2021;118.
[52] Li ZZ, Zhao ST, Ritchie RO, Meyers MA. Mechanical properties of high-entropy alloys with emphasis on face-centered cubic alloys. Prog Mater Sci 2019;102: 296–345.
[53] George EP, Raabe D, Ritchie RO. High-entropy alloys Nat Rev Mater 2019;4:515–34.
[54] Huang A, Fensin SJ, Meyers MA. Strain-rate effects and dynamic behavior of high entropy alloys. J Mater Res Technol 2023;22:307–47.
[55] Jiao ZM, Ma SG, Chu MY, Yang HJ, Wang ZH, Zhang Y, et al. Superior mechanical properties of $AlCoCrFeNiTi_x$ high-entropy alloys upon dynamic loading. J Mater Eng Perform 2015;25:451–546.
[56] Li Z, Zhao S, Diao H, Liaw PK, Meyers MA. High-velocity deformation of $Al_{0.3}CoCrFeNi$ high-entropy alloy: remarkable resistance to shear failure. Sci Rep 2017;7:42742.
[57] Gangireddy S, Gwalani B, Banerjee R, Mishra RS. High strain rate response of $Al_{0.7}CoCrFeNi$ high entropy alloy: dynamic strength over 2 GPa from thermomechanical processing and hierarchical microstructure. J Dynam Behav Mat 2018;5:1–7.
[58] Gangireddy S, Gwalani B, Liu K, Banerjee R, Mishra RS. Microstructures with extraordinary dynamic work hardening and strain rate sensitivity in $Al_{0.3}CoCrFeNi$ high entropy alloy. Mater Sci Eng, A 2018;734:42–50.
[59] Gangireddy S, Kaimiao L, Gwalani B, Mishra R. Microstructural dependence of strain rate sensitivity in thermomechanically processed $Al_{0.1}CoCrFeNi$ high entropy alloy. Mater Sci Eng, A 2018;727:148–59.
[60] Wang L, Qiao JW, Ma SG, Jiao ZM, Zhang TW, Chen G, et al. Mechanical response and deformation behavior of $Al_{0.6}CoCrFeNi$ high-entropy alloys upon dynamic loading. Mater Sci Eng, A 2018;727:208–13.
[61] Gwalani B, Gangireddy S, Zheng Y, Soni V, Mishra RS, Banerjee R. Influence of ordered $L1_2$ precipitation on strain-rate dependent mechanical behavior in a eutectic high entropy alloy. Sci Rep 2019;9:6371.
[62] Wang X, Zhao Y, Zhou J, Xue Y, Yuan F, Ma L, et al. Effect of solidification rate on the microstructure and strain-rate-sensitive mechanical behavior of AlCoCrFeNi high-entropy alloy prepared by bridgman solidification. Mater Trans 2019;60:929–34.
[63] Jiang K, Ren T, Shan G, Ye T, Chen L, Wang C, et al. Dynamic mechanical responses of the $Al_{0.1}CoCrFeNi$ high entropy alloy at cryogenic temperature. Mater Sci Eng A 2020;797.
[64] Gwalani B, Torgerson T, Dasari S, Jagetia A, Nartu MSKKY, Gangireddy S, et al. Influence of fine-scale B2 precipitation on dynamic compression and wear properties in hypo-eutectic $Al_{0.5}CoCrFeNi$ high-entropy alloy. J Alloys Compd 2021;853:157126.
[65] Wang CT, He Y, Guo Z, Huang X, Chen Y, Zhang H, et al. Strain rate effects on the mechanical properties of an AlCoCrFeNi high-entropy alloy. Met Mater Int 2021;27:2310–3238.
[66] Wang B, Wang C, Liu B, Zhang X. Dynamic mechanical properties and microstructure of an $(Al_{0.5}CoCrFeNi)_{0.95}Mo_{0.025}C_{0.025}$ high entropy alloy. Entropy 2019; 21.
[67] Muskeri S, Choudhuri D, Jannotti PA, Schuster BE, Lloyd JT, Mishra RS, et al. Ballistic impact response of $Al_{0.1}CoCrFeNi$ high-entropy alloy. Adv Eng Mater 2020;22.
[68] Gwalani B, Wang T, Jagetia A, Gangireddy S, Muskeri S, Mukherjee S, et al. Dynamic shear deformation of a precipitation hardened $Al_{0.7}CoCrFeNi$ eutectic high-entropy alloy using hat-shaped specimen geometry. Entropy 2020;22.
[69] Jiang ZJ, He JY, Wang HY, Zhang HS, Lu ZP, Dai LH. Shock compression response of high entropy alloys. Mater Res Lett 2016;4:226–32.
[70] Li D, Zhang Y. The ultrahigh charpy impact toughness of forged $Al_xCoCrFeNi$ high entropy alloys at room and cryogenic temperatures. Intermetallics 2016;70: 24–8.
[71] Jiang K, Li J, Meng Y, Hou B, Suo T. Dynamic tensile behavior of Al0.1CoCrFeNi high entropy alloy: Experiments, microstructure and modeling over a wide range of strain rates and temperatures. Mater Sci Eng A 2022;860.
[72] Arab A, Guo Y, Dilshad Ibrahim Sktani Z, Chen P. Effect of strain rate and temperature on deformation and recrystallization behaviour of BCC structure AlCoCrFeNi high entropy alloy. Intermetallics 2022;147.
[73] Zhang L. Thermo-mechanical characterization and dynamic failure of a CoCrFeNi high-entropy alloy. Mater Sci Eng A 2022;844.
[74] Hou X, Zhang X, Liu C, Chen H, Xiong W, Chen J, et al. Effects of annealing temperatures on mechanical behavior and penetration characteristics of FeNiCoCr high-entropy alloys. Metals 2022;12.
[75] Zhang NB, Xu J, Feng ZD, Sun YF, Huang JY, Zhao XJ, et al. Shock compression and spallation damage of high-entropy alloy Al0.1CoCrFeNi. J Mater Sci Technol 2022;128:1–9.
[76] Cheng JC, Qin HL, Li C, Zhao F, Pan RC, Wang QY, et al. Deformation and damage of equiatomic CoCrFeNi high-entropy alloy under plate impact loading. Mater Sci Eng A 2023;862.
[77] Wang B, Fu A, Huang X, Liu B, Liu Y, Li Z, et al. Mechanical properties and microstructure of the CoCrFeMnNi high entropy alloy under high strain rate compression. J Mater Eng Perform 2016;25:2985–92.
[78] Park JM, Moon J, Bae JW, Jang MJ, Park J, Lee S, et al. Strain rate effects of dynamic compressive deformation on mechanical properties and microstructure of CoCrFeMnNi high-entropy alloy. Mater Sci Eng, A 2018;719:155–63.
[79] Cao CM, Tong W, Bukhari SH, Xu J, Hao YX, Gu P, et al. Dynamic tensile deformation and microstructural evolution of $Al_xCrMnFeCoNi$ high-entropy alloys. Mater Sci Eng, A 2019;759:648–54.
[80] Soares GC, Patnamsetty M, Peura P, Hokka M. Effects of adiabatic heating and strain rate on the dynamic response of a CoCrFeMnNi high-entropy alloy. J Dynam Behav Mat 2019;5:320–30.
[81] Tsai S-P, Tsai Y-T, Chen Y-W, Chen P-J, Chiu P-H, Chen C-Y, et al. High-entropy CoCrFeMnNi alloy subjected to high-strain-rate compressive deformation. Mater Charact 2019;147:193–218.
[82] Foley DL, Huang SH, Anber E, Shanahan L, Shen Y, Lang AC, et al. Simultaneous twinning and microband formation under dynamic compression in a high entropy alloy with a complex energetic landscape. Acta Mater 2020;200:1–11.
[83] Hasan MN, Gu J, Jiang S, Wang HJ, Cabral M, Ni S, et al. Effects of elemental segregation on microstructural evolution and local mechanical properties in a dynamically deformed CrMnFeCoNi high entropy alloy. Scripta Mater 2021;190:80–5.
[84] Qiao Y, Chen Y, Cao F-H, Wang H-Y, Dai L-H. Dynamic behavior of CrMnFeCoNi high-entropy alloy in impact tension. Int J Impact Eng 2021;158:104008.
[85] Li Z, Zhao S, Alotaibi SM, Liu Y, Wang B, Meyers MA. Adiabatic shear localization in the CrMnFeCoNi high-entropy alloy. Acta Mater 2018;151:424–31.
[86] Yang Z, Yang M, Ma Y, Zhou L, Cheng W, Yuan F, et al. Strain rate dependent shear localization and deformation mechanisms in the CrMnFeCoNi high-entropy alloy with various microstructures. Mater Sci Eng A 2020;793.
[87] Thürmer D, Gunkelmann N. Shock-induced spallation in a nanocrystalline high-entropy alloy: an atomistic study. J Appl Phys 2022;131.
[88] Li W, Wang B, Huang X, Liu B, Brechtl J, Liaw PK. Mechanical behavior and shear band of a powder-metallurgy-fabricated CoCrFeMnNi high-entropy alloy during high strain-rate deformation. J Mater Res Technol 2022;21:1461–78.
[89] Yang Y, Yang S, Wang H. Effects of the phase content on dynamic damage evolution in $Fe_{50}Mn_{30}Co_{10}Cr_{10}$ high entropy alloy. J Alloys Compd 2021;851.
[90] Yang Y, Yang S, Wang H. Effects of microstructure on the evolution of dynamic damage of $Fe_{50}Mn_{30}Co_{10}Cr_{10}$ high entropy alloy. Mater Sci Eng, A 2021;802.
[91] Yang S, Yang Y, Yang Z, Lu C, Liu W. Adiabatic shear susceptibility of $Fe_{50}Mn_{30}Co_{10}Cr_{10}$ high-entropy alloy. Metall Mater Trans A 2020;51:1771–80.
[92] Choudhuri D, Jannotti PA, Muskeri S, Shukla S, Gangireddy S, Mukherjee S, et al. Ballistic response of a FCC-B2 eutectic $AlCoCrFeNi_{2.1}$ high entropy alloy. J Dynam Behav Mat 2019;5:495–503.
[93] Hu M, Song K, Song W. Dynamic mechanical properties and microstructure evolution of $AlCoCrFeNi_{2.1}$ eutectic high-entropy alloy at different temperatures. J Alloys Compd 2022;892:162097.
[94] Zhao SP, Feng ZD, Li LX, Zhao XJ, Lu L, Chen S, et al. Dynamic mechanical properties, deformation and damage mechanisms of eutectic high-entropy alloy AlCoCrFeNi21 under plate impact. J Mater Sci Technol 2023;134:178–88.
[95] Dirras G, Couque H, Lilensten L, Heczel A, Tingaud D, Couzinié JP, et al. Mechanical behavior and microstructure of $Ti_{20}Hf_{20}Zr_{20}Ta_{20}Nb_{20}$ high-entropy alloy loaded under quasi-static and dynamic compression conditions. Mater Charact 2016;111:106–13.

[96] Hu Ml, Song Wd, Duan Db, Wu Y. Dynamic behavior and microstructure characterization of TaNbHfZrTi high-entropy alloy at a wide range of strain rates and temperatures. Int J Mech Sci 2020;182:105738.
[97] Chen H-h, Zhang X-f, Dai L-h, Liu C, Xiong W, Tan M-t. Experimental study on WFeNiMo high-entropy alloy projectile penetrating semi-infinite steel target. Def Technol 2022;18:1470-82.
[98] Li C, Xue Y, Hua M, Cao T, Ma L, Wang L. Microstructure and mechanical properties of $Al_xSi_{0.2}CrFeCoNiCu_{1-x}$ high-entropy alloys. Mater Des 2016;90:601–69.
[99] Ma SG, Jiao ZM, Qiao JW, Yang HJ, Zhang Y, Wang ZH. Strain rate effects on the dynamic mechanical properties of the $AlCrCuFeNi_2$ high-entropy alloy. Mater Sci Eng, A 2016;649:35–8.
[100] Zhang TW, Jiao ZM, Wang ZH, Qiao JW. Dynamic deformation behaviors and constitutive relations of an $AlCoCr_{1.5}Fe_{1.5}NiTi_{0.5}$ high-entropy alloy. Scripta Mater 2017;136:15–9.
[101] Chen Y, Li Y, Cheng X, Wu C, Cheng B, Xu Z. The microstructure and mechanical properties of refractory high-entropy alloys with high plasticity. Materials 2018;11:208.
[102] Gwalani B, Gangireddy S, Shukla S, Yannetta CJ, Valentin SG, Mishra RS, et al. Compositionally graded high entropy alloy with a strong front and ductile back. Mater Today Commun 2019:20.
[103] Jo YH, Kim DG, Jo MC, Doh KY, Sohn SS, Lee D, et al. Effects of deformation-induced BCC martensitic transformation and twinning on impact toughness and dynamic tensile response in metastable VCrFeCoNi high-entropy alloy. J Alloys Compd 2019;785:1056–67.
[104] Song H, Kim DG, Kim DW, Jo MC, Jo YH, Kim W, et al. Effects of strain rate on room- and cryogenic-temperature compressive properties in metastable $V_{10}Cr_{10}Fe_{45}Co_{35}$ high-entropy alloy. Sci Rep 2019;9:6163.
[105] Chung TF, Chen PJ, Tai CL, Chiu P-H, Lin Y-S, Hsiao C-N, et al. Investigation of nanotwins in the bimodal-structured $Fe_{22}Co_{22}Ni_{20}Cr_{22}Mn_{14}$ alloy subjected to high-strain-rate deformation at cryogenic temperatures. Mater Charact 2020;170:110667.
[106] Sonkusare R, Jain R, Biswas K, Parameswaran V, Gurao NP. High strain rate compression behaviour of single phase CoCuFeMnNi high entropy alloy. J Alloys Compd 2020;823:153763.
[107] Zhang S, Wang Z, Yang HJ, Qiao JW, Wang ZH, Wu YC. Ultra-high strain-rate strengthening in ductile refractory high entropy alloys upon dynamic loading. Intermetallics 2020;121:106699.
[108] Haridas RS, Agrawal P, Thapliyal S, Yadav S, Mishra RS, McWilliams BA, et al. Strain rate sensitive microstructural evolution in a TRIP assisted high entropy alloy: experiments, microstructure and modeling. Mech Mater 2021;156.
[109] Jiang W, Gao X, Guo Y, Chen X, Zhao Y. Dynamic impact behavior and deformation mechanisms of $Cr_{26}Mn_{20}Fe_{20}Co_{20}Ni_{14}$ high-entropy alloy. Mater Sci Eng, A 2021:824.
[110] Li N, Chen W, He J, Gu J, Wang Z, Li Y, et al. Dynamic deformation behavior and microstructure evolution of $CoCrNiMo_x$ medium entropy alloys. Mater Sci Eng, A 2021:827.
[111] Ren K, Liu H, Chen R, Tang Y, Guo B, Li S, et al. Compression properties and impact energy release characteristics of TiZrNbV high-entropy alloy. Mater Sci Eng, A 2021;827:142074.
[112] Zhong X, Zhang Q, Xie J, Wu M, Jiang F, Yan Y, et al. Mechanical properties and microstructure of the $Al_{0.3}CoCrFeNiTi_{0.3}$ high entropy alloy under dynamic compression. Mater Sci Eng, A 2021;812:141147.
[113] Zhou S, Jian R, Liang Y-J, Zhu Y, Wang B, Wang L, et al. High susceptibility to adiabatic shear banding and high dynamic strength in tungsten heavy alloys with a high-entropy alloy matrix. J Alloys Compd 2021;859.
[114] Wang YZ, Jiao ZM, Bian GB, Yang HJ, He HW, Wang ZH, et al. Dynamic tension and constitutive model in $Fe_{40}Mn_{20}Cr_{20}Ni_{20}$ high-entropy alloys with a heterogeneous structure. Mater Sci Eng, A 2022:839.
[115] Tang W, Zhang K, Chen T, Wang Q, Wei B. Microstructural evolution and energetic characteristics of $TiZrHfTa_{0.7}W_{0.3}$ high-entropy alloy under high strain rates and its application in high-velocity penetration. J Mater Sci Technol 2023;132:144–53.
[116] Liu X, Wu Y, Wang Y, Chen J, Bai R, Gao L, et al. Enhanced dynamic deformability and strengthening effect via twinning and microbanding in high density NiCoFeCrMoW high-entropy alloys. J Mater Sci Technol 2022;127:164–76.
[117] Chung T-F, Lu S-Y, Lin Y-S, Li Y-L, Chiu P-H, Hsiao C-N, et al. Hierarchical nanotwins in Fe27Co24Ni23Cr26 high-entropy alloy subjected to high strain-rate Hopkinson bar deformation. Mater Charact 2022;185.
[118] Xu J, Liang L, Tong W, Wang HJ, Tian J, Peng LM. Role of strain rate in phase stability and deformation mechanism of non-equiatomic Fe38-xMn30Co15Cr15Ni2Gdx high-entropy alloy. Mater Charact 2022;194.
[119] Huang Y, Xie Z, Li W, Chen H, Liu B, Wang B. Dynamic mechanical properties of the selective laser melting NiCrFeCoMo0.2 high entropy alloy and the microstructure of molten pool. J Alloys Compd 2022:927.
[120] Chen J, Chen C, Guo K, Chang M, Wang R, Han Y, et al. Dynamic mechanical properties and ignition behavior of TiZrHfX0.5 high-entropy alloys associated with temperature, trace element and strain rate. J Alloys Compd 2023:933.
[121] Hawkins MC, Thomas S, Hixson RS, Gigax J, Li N, Liu C, et al. Dynamic properties of FeCrMnNi, a high entropy alloy. Mater Sci Eng, A 2022:840.
[122] Chung T-F, Chiu P-H, Tai C-L, Li Y-L, Wang L-M, Chen C-Y, et al. Investigation on the ballistic induced nanotwinning in the Mn-free $Fe_{27}Co_{24}Ni_{23}Cr_{26}$ high entropy alloy plate. Mater Chem Phys 2021;270.
[123] Johnson GR, Cook WH. Fracture characteristics of three metals subjected to various strains, strain rates, temperatures and pressures. Eng Fract Mech 1985;21:31–48.
[124] Tan JQ, Zhan M, Liu S, Huang T, Guo J, Yang H. A modified Johnson-Cook model for tensile flow behaviors of 7050–T7451 aluminum alloy at high strain rates. Mater Sci Eng, A 2015;631:214–29.
[125] Dodd B, Bai YL. Adiabatic shear localization: frontiers and advances. London: Elsevier Science Ltd.; 2012.
[126] Cowper GR, Symonds PS. Strain-hardening and strain-rate effects in the impact loading of cantilever beams. Division of Applied Mathematics Brown University; 1957.
[127] Zerilli FJ, Armstrong RW. Dislocation-mechanics-based constitutive relations for material dynamics calculations. J Appl Phys 1987;61:1816–25.
[128] Voyiadjis GZ, Abed FH. Microstructural based models for bcc and fcc metals with temperature and strain rate dependency. Mech Mater 2005;37:355–78.
[129] Huang S, Khan AS. Modeling the mechanical behaviour of 1100–0 aluminum at different strain rates by the bodner-partom model. Int J Plast 1992;8:501–17.
[130] Khan AS, Liu H. Variable strain rate sensitivity in an aluminum alloy: Response and constitutive modeling. Int J Plast 2012;36:1–14.
[131] Khan AS, Liu H. Strain rate and temperature dependent fracture criteria for isotropic and anisotropic metals. Int J Plast 2012;37:1–15.
[132] Li P, Li SX, Wang ZG, Zhang ZF. Unified factor controlling the dislocation evolution of fatigued face-centered cubic crystals. Acta Mater 2017;129:98–111.
[133] Zerilli FJ, Armstrong RW. The effect of dislocation drag on the stress-strain behavior of F.C.C. metals. Acta Metall Mater 1992;40:1803–2188.
[134] Taylor GI. Plastic strain in metals. J Inst Metals 1938;62:307–24.
[135] Estrin Y. Dislocation-density–related constitutive modeling. San Diego: Academic Press; 1996.
[136] Liang ZY, Wang X, Huang W, Huang MX. Strain rate sensitivity and evolution of dislocations and twins in a twinning-induced plasticity steel. Acta Mater 2015;88:170–219.
[137] Fullman RL. Measurement of approximately cylindrical particles in opaque samples. Trans Metall Soc AIME 1953;197:447–52.
[138] Olson GB, Cohen M. Kinetics of strain-induced martensitic nucleation. Metall Mater Trans A 1975;6:791.
[139] Kocks UF, Mecking H. Physics and phenomenology of strain hardening: the FCC case. Prog Mater Sci 2003;48:171–273.
[140] Beyerlein IJ, Tomé CN. A dislocation-based constitutive law for pure Zr including temperature effects. Int J Plast 2008;24:867–95.
[141] Zecevic M, Knezevic M, Beyerlein IJ, Tomé CN. An elasto-plastic self-consistent model with hardening based on dislocation density, twinning and de-twinning: application to strain path changes in HCP metals. Mater Sci Eng, A 2015;638:262–74.
[142] Bouaziz O, Estrin Y, Bréchet Y, Embury JD. Critical grain size for dislocation storage and consequences for strain hardening of nanocrystalline materials. Scripta Mater 2010;63:477–549.
[143] Byun TS. On the stress dependence of partial dislocation separation and deformation microstructure in austenitic stainless steels. Acta Mater 2003;51:3063–71.

[144] Curtze S, Kuokkala VT. Dependence of tensile deformation behavior of TWIP steels on stacking fault energy, temperature and strain rate. Acta Mater 2010;58:5129–41.
[145] Meyers MA, Subhash G, Kad BK, Prasad L. Evolution of microstructure and shear-band formation in α-hcp titanium. Mech Mater 1994;17:175–93.
[146] Rohde RW, Butcher BM, Holland JR, Karnes CH. Metallurgical effects at high strain rates. Boston: Springer; 1973.
[147] Grady DE. Properties of an adiabatic shear-band process zone. J Mech Phys Solids 1992;40:1197–215.
[148] Zhang W, Chen X, Zhuo B, Li P, He L. Effect of strain rate and temperature on dynamic mechanical behavior and microstructure evolution of ultra-high strength aluminum alloy. Mater Sci Eng, A 2018;730:336–44.
[149] Tang X, Li D, Prakash V, Lewandowski JJ. Effects of microstructure on high strain rate deformation and flow behaviour of Al–Mg–Si alloy (AA 6061) under uniaxial compression and combined compression and shear loading. Mater Sci Technol 2013;27:13–20.
[150] Fan X, Suo T, Sun Q, Wang T. Dynamic mechanical behavior of 6061 al alloy at elevated temperatures and different strain rates. Acta Mech Solida Sin 2013;26:111–20.
[151] Moćko W, Rodríguez-Martínez JA, Kowalewski ZL, Rusinek A. Compressive viscoplastic response of 6082–T6 and 7075–T6 aluminium alloys under wide range of strain rate at room temperature: experiments and modelling. Strain 2012;48:498–509.
[152] Wang J, Yuan X, Jin P, Ma H, Shi B, Zheng H, et al. Study on modified Johnson-Cook constitutive material model to predict the dynamic behavior Mg-1Al-4Y alloy. Mater Res Lett 2020:7.
[153] Kale C, Turnage S, Avery DZ, El Kadiri H, Jordon JB, Solanki KN. Towards dynamic tension-compression asymmetry and relative deformation mechanisms in magnesium. Materialia 2020:9.
[154] Shen J, Yin W, Kondoh K, Jones TL, Kecskes LJ, Yarmolenko SN, et al. Mechanical behavior of a lanthanum-doped magnesium alloy at different strain rates. Mater Sci Eng, A 2015;626:108–21.
[155] Chen Y, Tekumalla S, Guo YB, Shabadi R, Shim VPW, Gupta M. The dynamic compressive response of a high-strength magnesium alloy and its nanocomposite. Mater Sci Eng, A 2017;702:65–72.
[156] Xuefeng X, Tayyeb A, Lin W, Huanwu C, Zhe Z, Zixuan N, et al. Research on dynamic compression properties and deformation mechanism of Ti6321 titanium alloy. J Mater Res Technol 2020;9:11509–16.
[157] Markovsky PE, Janiszewski J, Bondarchuk VI, Stasyuk OO, Savvakin DG, Skoryk MA, et al. Effect of strain rate on microstructure evolution and mechanical behavior of titanium-based materials. Metals 2020:10.
[158] Mohammadhosseini A, Masood SH, Fraser D, Jahedi M. Dynamic compressive behaviour of Ti-6Al-4V alloy processed by electron beam melting under high strain rate loading. Adv Manuf 2015;3:232–43.
[159] Biswas N, Ding JL, Balla VK, Field DP, Bandyopadhyay A. Deformation and fracture behavior of laser processed dense and porous Ti6Al4V alloy under static and dynamic loading. Mater Sci Eng, A 2012;549:213–21.
[160] Yanjun H, Jinxu L, Jianchong L, Shukui L, Guohui W. Investigation on dynamic properties and failure mechanisms of Ti–47Al–2Cr–2Nb alloy under uniaxial dynamic compression at a temperature range of 288 K–773 K. J Alloys Compd 2015;649:122–217.
[161] Bobbili R, Madhu V. Physically-based constitutive model for flow behavior of a Ti-22Al-25Nb alloy at high strain rates. J Alloys Compd 2018;762:842–88.
[162] Song B, Chen W, Antoun BR, Frew DJ. Determination of early flow stress for ductile specimens at high strain rates by using a SHPB. Exp Mech 2007;47:671–769.
[163] Hu X, Xie L, Gao F, Xiang J. On the development of material constitutive model for 45CrNiMoVA ultra-high-strength steel. Metals 2019:9.
[164] Fu H, Wang X, Xie L, Hu X, Umer U, Rehman AU, et al. Dynamic behaviors and microstructure evolution of iron-nickel based ultra-high strength steel by SHPB testing. Metals 2019:10.
[165] Lu T, Li Y, Zhao H, Wang C, Han S. Dynamic constitutive behavior investigation of a novel low alloy ultra-high strength steel. Mater Res Lett 2021:8.
[166] Xiong Z-p, Ren X-p, Bao W-p, Shu J, Li S-x, Qu H-t. Effect of high temperature and high strain rate on the dynamic mechanical properties of Fe-30Mn-3Si-4Al TWIP steel. Int J Miner, Metall Mater 2013;20:835–41.
[167] Khan AS, Liang R. Behaviors of three BCC metal over a wide range of strain rates and temperatures: experiments and modeling. Int J Plast 1999;15:1089–109.
[168] Ren J, Xu Y, Zhao X, Zhao P. Dynamic mechanical behaviors and failure thresholds of ultra-high strength low-alloy steel under strain rate 0.001/s to 106/s. Mater Sci Eng, A 2018;719:178–91.
[169] Chen G, Hao Y, Chen X, Hao H. Compressive behaviour of tungsten fibre reinforced Zr-based metallic glass at different strain rates and temperatures. Int J Impact Eng 2017;106:110–9.
[170] Kim Y, Shin SY, Kim JS, Huh H, Kim KJ, Lee S. Dynamic deformation behavior of Zr-based amorphous alloy matrix composites reinforced with STS304 or tantalum fibers. Metall Mater Trans A 2012;43:3023–33.
[171] Wu RF, Jiao ZM, Wang YS, Wang Z, Wang ZH, Ma SG, et al. Excellent plasticity of a new Ti-based metallic glass matrix composite upon dynamic loading. Mater Sci Eng, A 2016;677:376–83.
[172] Chen TH, Tsai CK. The microstructural evolution and mechanical properties of Zr-based metallic glass under different strain rate compressions. Materials 2015;8:1831–40.
[173] Liu J, Shim VPW. Characterization and modelling of in-situ La-based bulk metallic glass composites under static and dynamic loading. Int J Impact Eng 2015;80:94–106.
[174] Xue Y, Zhong X, Wang L, Fan Q, Zhu L, Fan B, et al. Effect of W volume fraction on dynamic mechanical behaviors of W fiber/Zr-based bulk metallic glass composites. Mater Sci Eng, A 2015;639:417–24.
[175] Wang BP, Yu BQ, Fan QB, Liang JY, Wang L, Xue YF, et al. Anisotropic dynamic mechanical response of tungsten fiber/Zr-based bulk metallic glass composites. Mater Des 2016;93:485–93.
[176] Li W, Geng T, Ge S, Zhu Z, Zhang L, Li Z, et al. Effect of strain rate on compressive behavior of a Zr-based metallic glass under a wide range of strain rates. Materials 2020:13.
[177] Hufnagel TC, Jiao T, Li Y, Xing LQ, Ramesh KT. Deformation and failure of $Zr_{57}Ti_5Cu_{20}Ni_8Al_{10}$ bulk metallic glass under quasi-static and dynamic compression. J Mater Res 2011;17:1441–2145.
[178] Liu X, Yang C, Yang X, Luo L, He X, Kang S. Dynamic mechanical behavior and adiabatic shear bands of ultrafine grained pure zirconium. J Wuhan Univ Technol, Mater Sci Ed 2020;35:200–27.
[179] Wang T, Li B, Li Y, Li M, Nie Z. Evolution mechanism of dislocation boundary and characteristic micro-structure of commercial pure titanium during the projectile impact. Mater Sci Eng, A 2018;712:325–31.
[180] Kapoor R, Nemat-Nasser S. Comparison between high and low strain-rate deformation of tantalum. Metall Mater Trans A 2000;31:815–23.
[181] He JY, Zhu C, Zhou DQ, Liu WH, Nieh TG, Lu ZP. Steady state flow of the FeCoNiCrMn high entropy alloy at elevated temperatures. Intermetallics 2014;55:9–14.
[182] Bu Y, Wu Y, Lei Z, Yuan X, Wu H, Feng X, et al. Local chemical fluctuation mediated ductility in body-centered-cubic high-entropy alloys. Mater Today 2021;46:28–34.
[183] Yin B, Curtin WA. Origin of high strength in the CoCrFeNiPd high-entropy alloy. Mater Res Lett 2020;8:209–15.
[184] Ma E, Wu X. Tailoring heterogeneities in high-entropy alloys to promote strength-ductility synergy. Nat Commun 2019;10:5623.
[185] Liu SF, Wu Y, Wang HT, Lin WT, Shang YY, Liu JB, et al. Transformation-reinforced high-entropy alloys with superior mechanical properties via tailoring stacking fault energy. J Alloys Compd 2019;792:444–55.
[186] Lu J, Hultman L, Holmström E, Antonsson KH, Grehk M, Li W, et al. Stacking fault energies in austenitic stainless steels. Acta Mater 2016;111:39–46.
[187] Allain S, Chateau JP, Bouaziz O, Migot S, Guelton N. Correlations between the calculated stacking fault energy and the plasticity mechanisms in Fe–Mn–C alloys. Mater Sci Eng, A 2004;387–389:158–62.
[188] Sato K, Ichinose M, Hirotsu Y, Inoue Y. Effects of deformation induced phase transformation and twinning on the mechanical properties of austenitic Fe-Mn-Al alloys. ISIJ Int 1989;29:868–77.

[189] Regazzoni G, Kocks UF, Follansbee PS. Dislocation kinetics at high strain rates. Acta Metall 1987;35:2865–75.
[190] Yao S, Pei X, Liu Z, Yu J, Yu Y, Wu Q. Numerical investigation of the temperature dependence of dynamic yield stress of typical BCC metals under shock loading with a dislocation-based constitutive model. Mech Mater 2020;140.
[191] Suzuki YKHOKKT. Plastic homology of bcc metals. Philos Mag A 1999;79:1629–42.
[192] Imura T, Noda K, Matsui H, Saka H, Kimura H. Dislocations in solids. Tokyo: University Tokyo Press; 1985.
[193] Zotov N, Grabowski B. Molecular dynamics simulations of screw dislocation mobility in bcc Nb. Modell Simul Mater Sci Eng 2021;29.
[194] Ateba Betanda Y, Helbert A-L, Brisset F, Mathon M-H, Waeckerlé T, Baudin T. Measurement of stored energy in Fe–48%Ni alloys strongly cold-rolled using three approaches: Neutron diffraction, Dillamore and KAM approaches. Mater Sci Eng, A 2014;614:193–218.
[195] Williamson GK, Hall WH. X-ray line broadening from filed aluminium and wolfram. Acta Metall 1953;1:22–31.
[196] Williamson GK, Smallman III RE. Dislocation densities in some annealed and cold-worked metals from measurements on the X-ray debye-scherrer spectrum. Philos Mag 1956;1:34–46.
[197] Dirras G, Gubicza J, Heczel A, Lilensten L, Couzinié JP, Perrière L, et al. Microstructural investigation of plastically deformed $Ti_{20}Zr_{20}Hf_{20}Nb_{20}Ta_{20}$ high entropy alloy by X-ray diffraction and transmission electron microscopy. Mater Charact 2015;108:1–7.
[198] Rx W, Tang Y, Li S, Ai Y, Li Y, Xiao B, et al. Effect of lattice distortion on the diffusion behavior of high-entropy alloys. J Alloys Compd 2020;825:154099.
[199] Kumar N, Komarasamy M, Nelaturu P, Tang Z, Liaw PK, Mishra RS. Friction stir processing of a high entropy alloy $Al_{0.1}CoCrFeNi$. JOM 2015;67:1007–13.
[200] Wu Z, Bei H, Pharr GM, George EP. Temperature dependence of the mechanical properties of equiatomic solid solution alloys with face-centered cubic crystal structures. Acta Mater 2014;81:428–41.
[201] Zhang Y, Zuo TT, Tang Z, Gao MC, Dahmen KA, Liaw PK, et al. Microstructures and properties of high-entropy alloys. Prog Mater Sci 2014;61:1–93.
[202] Lee C, Chou Y, Kim G, Gao MC, An K, Brechtl J, et al. Lattice-distortion-enhanced yield strength in a refractory high-entropy alloy. Adv Mater 2020;32:e2004029.
[203] Feng R, Feng B, Gao MC, Zhang C, Neuefeind JC, Poplawsky JD, et al. Superior high-temperature strength in a supersaturated refractory high-entropy alloy. Adv Mater 2021;33:e2102401.
[204] Lee C, Song G, Gao MC, Feng R, Chen P, Brechtl J, et al. Lattice distortion in a strong and ductile refractory high-entropy alloy. Acta Mater 2018;160:158–72.
[205] Ding J, Yu Q, Asta M, Ritchie RO. Tunable stacking fault energies by tailoring local chemical order in CrCoNi medium-entropy alloys. Proc Natl Acad Sci U S A 2018;115:8919–24.
[206] Tamm A, Aabloo A, Klintenberg M, Stocks M, Caro A. Atomic-scale properties of Ni-based FCC ternary, and quaternary alloys. Acta Mater 2015;99:307–12.
[207] Zhang R, Zhao S, Ding J, Chong Y, Jia T, Ophus C, et al. Short-range order and its impact on the CrCoNi medium-entropy alloy. Nature 2020;581:283–327.
[208] Zhang R, Zhao S, Ophus C, Deng Y, Vachhani SJ, Ozdol B, et al. Direct imaging of short-range order and its impact on deformation in Ti-6Al. Sci Adv 2019;5:eaax2799.
[209] Chen H, Wang YD, Nie Z, Li R, Cong D, Liu W, et al. Unprecedented non-hysteretic superelasticity of [001]-oriented NiCoFeGa single crystals. Nat Mater 2020;19:712–78.
[210] Sudmanns M, El-Awady JA. The effect of local chemical ordering on dislocation activity in multi-principle element alloys: a three-dimensional discrete dislocation dynamics study. Acta Mater 2021;220:117307.
[211] Lei Z, Wu Y, He J, Liu X, Wang H, Jiang S, et al. Snoek-type damping performance in strong and ductile high-entropy alloys. Sci Adv 2020;6:eaba7802.
[212] Hirata A, Kang LJ, Fujita T, Klumov B, Matsue K, Kotani M, et al. Geometric frustration of icosahedron in metallic glasses. Science 2013;341:376–9.
[213] Sheng HW, Luo WK, Alamgir FM, Bai JM, Ma E. Atomic packing and short-to-medium-range order in metallic glasses. Nature 2006;439:419–25.
[214] Smith WF, Hashemi J. Foundations of materials science and engineering. USA: McGraw-Hill Inc; 2009.
[215] Hall EO. The deformation and ageing of mild steel: III discussion of results. Proc Phys Soc Sec B 1951;64:747.
[216] Petch N. The cleavage strength of polycrystals. J Iron Steel InstInst 1953;174:25–8.
[217] Hansen N. Hall-Petch relation and boundary strengthening. Scripta Mater 2004;51:801–86.
[218] Liu WH, Wu Y, He JY, Nieh TG, Lu ZP. Grain growth and the Hall-Petch relationship in a high-entropy FeCrNiCoMn alloy. Scripta Mater 2013;68:526–59.
[219] Kang B, Lee J, Ryu HJ, Hong SH. Microstructure, mechanical property and Hall-Petch relationship of a light-weight refractory Al0.1CrNbVMo high entropy alloy fabricated by powder metallurgical process. J Alloys Compd 2018;767:1012–21.
[220] Chen S, Tseng K-K, Tong Y, Li W, Tsai C-W, Yeh J-W, et al. Grain growth and Hall-Petch relationship in a refractory HfNbTaZrTi high-entropy alloy. J Alloys Compd 2019;795:19–26.
[221] Liang YJ, Wang L, Wen Y, Cheng B, Wu Q, Cao T, et al. High-content ductile coherent nanoprecipitates achieve ultrastrong high-entropy alloys. Nat Commun 2018;9:4063.
[222] Koike J, Kobayashi T, Mukai T, Watanabe H, Suzuki M, Maruyama K, et al. The activity of non-basal slip systems and dynamic recovery at room temperature in fine-grained AZ31B magnesium alloys. Acta Mater 2003;51:2055–65.
[223] Meyers MA, Vöhringer O, Lubarda VA. The onset of twinning in metals: a constitutive description. Acta Mater 2001;49:4025–39.
[224] Ming K, Bi X, Wang J. Strength and ductility of CrFeCoNiMo alloy with hierarchical microstructures. Int J Plast 2019;113:255–68.
[225] Laplanche G, Kostka A, Reinhart C, Hunfeld J, Eggeler G, George EP. Reasons for the superior mechanical properties of medium-entropy CrCoNi compared to high-entropy CrMnFeCoNi. Acta Mater 2017;128:292–303.
[226] Zhang Z, Mao MM, Wang J, Gludovatz B, Zhang Z, Mao SX, et al. Nanoscale origins of the damage tolerance of the high-entropy alloy CrMnFeCoNi. Nat Commun 2015;6:10143.
[227] Ma Y, Yuan F, Yang M, Jiang P, Ma E, Wu X. Dynamic shear deformation of a CrCoNi medium-entropy alloy with heterogeneous grain structures. Acta Mater 2018;148:407–18.
[228] Huang H, Wu Y, He J, Wang H, Liu X, An K, et al. Phase-transformation ductilization of brittle high-entropy alloys via metastability engineering. Adv Mater 2017;29:1701678.
[229] Wu YD, Cai YH, Wang T, Si JJ, Zhu J, Wang YD, et al. A refractory $Hf_{25}Nb_{25}Ti_{25}Zr_{25}$ high-entropy alloy with excellent structural stability and tensile properties. Mater Lett 2014;130:277–80.
[230] Senkov ON, Semiatin SL. Microstructure and properties of a refractory high-entropy alloy after cold working. J Alloys Compd 2015;649:1110–23.
[231] Schuster BE, Ligda JP, Pan ZL, Wei Q. Nanocrystalline refractory metals for extreme condition applications. JOM 2011;63:27–31.
[232] Wei Q, Kecskes LJ, Ramesh KT. Effect of low-temperature rolling on the propensity to adiabatic shear banding of commercial purity tungsten. Mater Sci Eng, A 2013;578:394–401.
[233] Wei Q, Schuster BE, Mathaudhu SN, Hartwig KT, Kecskes LJ, Dowding RJ, et al. Dynamic behaviors of body-centered cubic metals with ultrafine grained and nanocrystalline microstructures. Mater Sci Eng, A 2008;493:58–64.
[234] Zou DL, Luan BF, Liu Q, Chai LJ, Chen JW. Formation and evolution of adiabatic shear bands in zirconium alloy impacted by split Hopkinson pressure bar. J Nucl Mater 2013;437:380–438.
[235] Zhan H, Zeng W, Wang G, Kent D, Dargusch M. Microstructural characteristics of adiabatic shear localization in a metastable beta titanium alloy deformed at high strain rate and elevated temperatures. Mater Charact 2015;102:103–13.
[236] Li N, Wang YD, Lin Peng R, Sun X, Liaw PK, Wu GL, et al. Localized amorphism after high-strain-rate deformation in TWIP steel. Acta Mater 2011;59:6369–77.
[237] Baik S-I, Gupta RK, Kumar KS, Seidman DN. Temperature increases and thermoplastic microstructural evolution in adiabatic shear bands in a high-strength and high-toughness 10 wt.% Ni steel. Acta Mater 2021;205:116568.
[238] Wang RX. Microstructure evolution and energetic structural properties of NbZrTiTa high-entropy alloy. Changsha, China: National University of Defense Technology; 2018.
[239] Hu K, Li X, Guan M, Qu S, Yang X, Zhang J. Dynamic deformation behavior of 93W–5.6Ni-1.4Fe heavy alloy prepared by spark plasma sintering. Int J Refract Met Hard Mater 2016;58:117–24.

[240] Couque H, Nicolas G, Altmayer C. Relation between shear banding and penetration characteristics of conventional tungsten alloys. Int J Impact Eng 2007;34:412–23.
[241] Hu K, Li X, Liu B, Guan M, Qu S, Han S. Dynamic mechanical behavior of 93W–4.9Ni–2.1Fe/95W–2.8Ni–1.2Fe–1Al2O3 heavy alloy composite. Mater Sci Eng, A 2018;729:349-56.
[242] Yamada H, Ogasawara N, Shimizu Y, Horikawa K, Kobayashi H, Chen X. Effect of high strain rate on indentation in pure aluminum. J Eng Mater Technol 2013;135.
[243] Moon J, Hong SI, Bae JW, Jang MJ, Yim D, Kim HS. On the strain rate-dependent deformation mechanism of CoCrFeMnNi high-entropy alloy at liquid nitrogen temperature. Mater Res Lett 2017;5:472–547.
[244] Sun C, Ma J, Yang Y, Hartwig KT, Maloy SA, Wang H, et al. Temperature and grain size dependent plastic instability and strain rate sensitivity of ultrafine grained austenitic Fe–14Cr–16Ni alloy. Mater Sci Eng, A 2014;597:415–21.
[245] Wu Z, Gao Y, Bei H. Thermal activation mechanisms and Labusch-type strengthening analysis for a family of high-entropy and equiatomic solid-solution alloys. Acta Mater 2016;120:108–19.
[246] Xu Z, Huang F. Thermomechanical behavior and constitutive modeling of tungsten-based composite over wide temperature and strain rate ranges. Int J Plast 2013;40:163–84.
[247] Wang H, Wu P, Kurukuri S, Worswick MJ, Peng Y, Tang D, et al. Strain rate sensitivities of deformation mechanisms in magnesium alloys. Int J Plast 2018;107:207–22.
[248] Wei Q, Cheng S, Ramesh KT, Ma E. Effect of nanocrystalline and ultrafine grain sizes on the strain rate sensitivity and activation volume: fcc versus bcc metals. Mater Sci Eng, A 2004;381:71–9.
[249] Rohatgi A, Vecchio KS, Gray GT. The influence of stacking fault energy on the mechanical behavior of Cu and Cu-Al alloys: Deformation twinning, work hardening, and dynamic recovery. Metall Mater Trans A 2001;32:135–45.
[250] Yang HK, Zhang ZJ, Tian YZ, Zhang ZF. Negative to positive transition of strain rate sensitivity in Fe-22Mn-0.6C-x(Al) twinning-induced plasticity steels. Mater Sci Eng, A 2017;690:146–57.
[251] Lichtenfeld JA, Van Tyne CJ, Mataya MC. Effect of strain rate on stress-strain behavior of alloy 309 and 304L austenitic stainless steel. Metall Mater Trans A 2006;37:147–61.

Dr. Yu Tang is associate professor in College of Aerospace Science and Engineering, National University of Defense Technology, China. He got his Ph.D. from Zhejiang University in 2016. His research interests are high-entropy alloys and their applications. He proposed and verified the application potential of high-entropy alloys as energetic structural materials. In recent 3 years, Dr. Tang have been published more than 20 papers in the field of high-entropy alloys.

Dr. Ruixin Wang is research assistant in College of Aerospace Science and Engineering, National University of Defense Technology, China. She received her Ph.D. in Materials Science and Engineering from National University of Defense Technology in 2023. Her research interests revolve around mechanical behaviors of high entropy alloys under extreme environments.

Dr. Junwei Qiao is professor of the Laboratory of High Entropy Alloys at Taiyuan University of Technology in China. He got his Ph.D. from the State Key Laboratory of Advanced Metals and Materials at University of Science and Technology Beijing in 2011. His research interests include microstructures and mechanical properties of high-entropy alloys, the shear avalanche in amorphous solids, and mechanical behaviors of in-situ metallic glass matrix composites, etc. Up to now, he has published more than 200 papers in the field of materials science, and has edited two books (in Chinese): High-entropy Alloys, and Face-centered Cubic High-entropy Alloys.

Dr. Shunxin Bai is professor in College of Aerospace Science and Engineering, National University of Defense Technology, China. He received his Ph.D. degree from National University of Defense Technology. His research interests include metal-based high-temperature thermal structures, energetic structural materials and electronic information materials. He has published more than 200 papers and authorized 20 patents in the field of materials science.

Dr. Yong Zhang is professor in the state key laboratory for advanced metals and materials, the University of Science and Technology Beijing, China. He received his Ph.D degree in materials science from the University of Science and Technology Beijing in 1998. He is devoting himself to studying sawtooth behavior, high-throughput technology and collective effect in materials science. His research interests are amorphous alloys and high entropy materials. He has published more than 200 academic papers which were cited more than 20,000 times and 6 books in the field of materials science.

Dr. Peter K. Liaw is John Fisher Professor, Ivan Racheff Chair of Excellence, and National Alumni Association Distinguished Service Professor in Department of Materials Science and Engineering, The University of Tennessee, USA. He received his Ph.D in Materials Science and Engineering from Northwestern University, USA. His main research interests include mechanical behavior of high-entropy alloys, superalloys, bulk-metallic glasses and metal-matrix composites, neutron and synchrotron studies of mechanical behavior, corrosion-fatigue crack-growth behavior of nuclear materials, etc. Up to now, he has published more than 1100 papers and 60 books in the field of materials science.